LIGO interferometer operating at design sensitivity with application to gravitational radiometry

by

Stefan W. Ballmer

Submitted to the Department of Physics
in partial fulfillment of the requirements for the degree of

Doctor of Philosophy

at the

MASSACHUSETTS INSTITUTE OF TECHNOLOGY

June 2006

Author . . . .
Department of Physics
May 3rd, 2006

Certified by. . . . .
Erotokritos Katsavounidis
Professor
Thesis Supervisor

Certified by. . . . .
Peter Fritschel
Principal Research Scientist
Thesis Co-Supervisor

Accepted by . . . .
Thomas J. Greytak
Associate Department Head for Education

LIGO interferometer operating at design sensitivity with application to gravitational radiometry

by

Stefan W. Ballmer

Abstract

During the last decade the three interferometers of the Laser Interferometer Gravitational Wave Observatory (LIGO) were built and commissioned. In fall 2005 design sensitivity was achieved, corresponding to a strain sensitivity of 2.5×10^{-23} Hz$^{-1/2}$ at 150 Hz. All three interferometers are now in an extended science run.

One of the most critical steps to reach this goal was increasing the power in the interferometer to more than 200 Watt at the beam splitter. This required the commissioning of both a thermal compensation system and shot noise limited sensing electronics capable of detecting all the light. Additionally, a series of unexpected noise sources had to be mitigated. This work is described in the first part of this thesis.

In a second part I introduce a radiometer analysis that is capable of spatially resolving anisotropies in a stochastic gravitational wave background. The analysis is optimized for identifying point sources of stochastic gravitational radiation.

Finally, data from the fourth LIGO science run is used to set both isotropic and directional upper limits on the stochastic background of gravitational waves. The bound set on the normalized gravitational wave energy density is $h^2 \Omega_{\mathrm{gw}}(f) < 6.25 \times 10^{-5}$ and the limit set on a broadband and flat strain power spectrum coming from a point source varies between 8.5×10^{-49}Hz^{-1} and 6.1×10^{-48}Hz^{-1}, depending on the source position. Additionally a limit on gravitational radiation coming from the direction of Sco-X1, the brightest X-ray source short of the sun, is set for each frequency bin.

Thesis Supervisor: Erotokritos Katsavounidis
Title: Professor

Thesis Co-Supervisor: Peter Fritschel
Title: Principal Research Scientist

Acknowledgments

I had the privilege to join the LIGO project in the final phase of interferometer commissioning, and was given the chance to work on what is arguably the biggest table-top experiment a physics graduate student can dream of working on. As a consequence I had the pleasure to work with many great people from the project, probably learning something from each and every one of them.

As much as I would like to do it, thanking all of them personally would fill too many pages of an already too long thesis. But even so I want to take this opportunity to mention at least a few of them by name.

To Rana, thanks for showing me how to solder a cable and how to wire up an op-amp.

To Paul, thanks for teaching the beauty of RF electronics to the 21st century youth.

To Peter, thanks for teaching me the difference between AS_I and AS_Q.

Dir, Daniel, danke für all dä Whisky won i Dir wäggsoffe ha.

To Dave, Gregg and Rich, for keeping me from drinking my Guinness alone, thanks.

To Rai, thank you for getting me into this adventure.

To Erik, thanks for letting me run with my own ideas and always supporting me.

To Nergis, thank you for getting me away from the dark side of physics.

To Marie, for taking bureaucracy off my shoulders, thank you.

To the whole Hanford crew, thank you all for the hospitality and support I enjoyed. And sorry for all those sleepless night I have caused for some of you...

I would also like to thank Edith for the many beautiful moments we shared whenever we were not working on opposite sides of the Atlantic ocean. Finally, I want to express my deep gratitude to my parents, Ruth and Werner Ballmer, for all the love and care I enjoyed in the last thirty one years of my life. Without them this thesis would never have been written.

- Stefan, May 3, 2006

Contents

List of Figures

List of Tables

Preface

Ever since the existence of gravitational waves was first predicted by Albert Einstein in 1918 [1], the experimental challenge to directly measure their effect was daunting. It was clear that the laboratory generation of gravitational waves strong enough for the experimental verification of Einstein's prediction is virtually impossible - by far the largest wave amplitudes are due to rare collisions of stellar-sized compact objects. It took more than 40 years before J. Weber made the first serious attempt to directly measure their effect using a resonant bar detector [25].

Then, in 1975, the discovery of the binary pulsar PSR 1913+16 by Hulse and Taylor [2, 3] provided a laboratory with which the emission of gravitational waves could be tested. Over the years their data indeed showed a decrease in the orbital period of the binary, consistent with the energy loss predicted by the emission of gravitational waves, proving, albeit indirectly, the existence of gravitational waves.

The potential payoff of directly measuring gravitational waves would be enormous. Gravitational waves are created during the first fraction of a second after the big bang, or originate at the core of stellar collisions or explosions. Exactly because they interact so little with matter, they penetrate the surrounding matter that is responsible for emission of electromagnetic radiation, so far the only carrier of information about such events. Directly observing gravitational waves therefore would literally open a new window to the universe.

Today, 88 years after Einstein's prediction, nobody has yet succeeded in directly detecting gravitational waves. However, during the last decade a handful of kilometer scale, laser interferometer gravitational wave antennae were constructed, commissioned and have begun operation. This worldwide network of observatories includes

the German-British GEO600 [1] [40], the Japanese TAMA [2][41], the Italian-French VIRGO [3] [46] and a set of three interferometers in the United States called Laser Interferometer Gravitational Wave Observatory (LIGO) [4] [42, 45].

Personally I had the privilege to join the LIGO laboratory for the last five years of the initial interferometer commissioning phase. I spent almost 2 years at the LIGO Hanford Observatory in Washington State, where I spearheaded the day-to-day commissioning of the 4km interferometer. This was diverse and exceptionally rewarding work. Of course the main goal was to improve the interferometer strain sensitivity, but due to the intertwined complexity of the LIGO interferometers I had to become familiar with almost every subsystem. This also meant working together with many people from across the whole the project, all of them experts on their own subsystem. I would like to use this opportunity to thank all of them; I learned a lot from them.

After an introduction to gravitational waves in chapter 1, I summarize the key hardware improvements that were made while I was working at the LIGO Hanford Observatory in chapter 2. They were the last steps required to reach the design sensitivity laid out more than a decade ago [39].

In chapter 3 I introduce an analysis that uses the data from the two LIGO sites to set a directional upper limit on stochastic gravitational background radiation. Finally, in chapter 4, I report on the results of this analysis from the LIGO S4 Science Run.

This work, and the LIGO Laboratory, is supported by the United States National Science Foundation [5] under Cooperative Agreement PHY-0107417.

Chapter 1

Gravitational Radiation

By 1905 Albert Einstein's Special Theory of Relativity established Lorentz invariance as the fundamental symmetry of space and time. It became clear that Isaac Newton's law of gravitation needed to be extended since it included instantaneous action at a distance, which violates of causality in the framework of Lorentz invariance. All attempts to modify Newton's theory to comply with Lorentz invariance necessarily include a finite propagation speed of gravitational phenomena. In that sense already the Special Theory of Relativity suggests the existence of gravitational waves. Furthermore it is also no surprise that such waves should propagate at the speed of light, for this is the only Lorentz invariant velocity.

The exact properties of such gravitational waves however were only predicted by Einstein's General Theory of Relativity, and were worked out in his 1918 article "Über Gravitationswellen" [1]. The following section is a quick review to this prediction. I chose to do it formally because this highlights how few assumptions actually go into its derivation.

1.1   Gravitational Radiation in General Relativity

The big philosophical leap that lead Einstein to the General Theory of Relativity was insight that one has to abandon the view of space-time as an unalterable stage on which the universe evolves. Instead space-time itself becomes a dynamic field that is

influenced by the matter floating in it. Euclidean geometry is no longer appropriate.

Following the ideas of Bernhard Riemann such a curved space-time can be described by a metric $g_{\mu\nu}$, which is a function of the coordinates $\xi^\mu = (t, x^1, x^2, x^3)$: the infinitesimal distance or eigen time $d\tau$ between 2 events (points) separated by $d\xi^\mu$ is given by

$$d\tau^2 = d\xi^\mu g_{\mu\nu} d\xi^\nu \tag{1.1}$$

The metric $g_{\mu\nu}$ is a dynamic field. In the limit of special relativity the metric $g_{\mu\nu}$ becomes the Minkowski metric $\eta_{\mu\nu} = \mathrm{diag}(-1, 1, 1, 1)$.

1.1.1 The linearized Einstein Equation

The Einstein equation is a 2nd order differential equation for the metric tensor $g_{\mu\nu}$. It determines the evolution of $g_{\mu\nu}$ under the influence of matter, which in turn is described by the stress tensor $T_{\mu\nu}$:

$$G_{\mu\nu}(g_{\mu\nu}) = 8\pi G T_{\mu\nu} \tag{1.2}$$

Here G is Newton's constant and the 2nd order differential operator $G_{\mu\nu}$ is called Einstein tensor. The derivation of an explicit expression for $G_{\mu\nu}$ was one of the central results of Einstein.

Since we are interested in describing gravitational waves far away from any source we can use the weak field limit, defined by

$$g_{\mu\nu} = \eta_{\mu\nu} + h_{\mu\nu}, \quad |h_{\mu\nu}| \ll 1 \tag{1.3}$$

where $\eta_{\mu\nu}$ is again the Minkowski metric. Then the Einstein tensor $G_{\mu\nu}$ becomes linear and is given by

$$2G_{\mu\nu} = -h_{\mu\nu,\lambda}{}^\lambda + h_\mu{}^\lambda{}_{,\lambda\nu} + h_\nu{}^\lambda{}_{,\lambda\mu} - \eta_{\mu\nu} h^{\lambda\sigma}{}_{,\lambda\sigma} + \eta_{\mu\nu} h_{,\lambda}{}^\lambda - h_{,\mu\nu} \tag{1.4}$$

In the last term h is the trace of $h_{\mu\nu}$, i.e. $h = h^\mu_\mu$.

18

While this looks complicated at first glance it is surprisingly simple to see why this has to be the correct expression:

- *Newton:* Since the theory has to be an extension of Newton's work, we know that there has to be a Laplace operator acting on the quantity that describes the gravitational field ($h_{\mu\nu}$). The Lorentz-invariant extension is the D'Alembert operator $\Box = \partial_t^2 - \triangle$. This is the 1st term in equation 1.4.

- *Energy-Momentum conservation:* It implies $0 = 8\pi G T_{\mu\nu}{}^{,\nu} = G_{\mu\nu}{}^{,\nu}$. This requires the 2nd term in equation 1.4. Since $T_{\mu\nu}$ and therefore $G_{\mu\nu}$ are symmetric in μ and ν, we also need the 3rd term. But this 3rd term also has to be canceled. Applying the same argument again thus gives rise to the 4th term.

- *Covariance:* The Einstein equation has to be invariant under any coordinate transformations, in particular infinitesimal ones of the form $\tilde{x}^\mu = x^\mu + \xi^\mu$. For those $h_{\mu\nu}$ transforms as $\tilde{h}_{\mu\nu} = h_{\mu\nu} - \xi_{\mu,\nu} - \xi_{\nu,\mu}$. Requiring that the Einstein tensor is invariant under these transformations leads to term 5 (to cancel term 4) and term 6 (to cancel terms 2 and 3). Terms 5 and 6 together also fulfill the Energy-Momentum conservation criterion.

1.1.2 The transverse-traceless gauge

To see the physical effect of a gravitational wave it is useful to fix the gauge. The most practical choice is to introduce the trace-inversed strain $\tilde{h}_{\mu\nu}$

$$\tilde{h}_{\mu\nu} = h_{\mu\nu} - \frac{1}{2}\eta_{\mu\nu}h \tag{1.5}$$

and impose the *harmonic gauge condition* (transversality)

$$\tilde{h}_{\mu\nu}^{,\nu} = 0 \tag{1.6}$$

19

This reduces the Einstein equation to a simple wave equation:

$$G_{\mu\nu} = -\frac{1}{2}\Box\tilde{h}_{\mu\nu} = 8\pi G T_{\mu\nu} \tag{1.7}$$

Furthermore if we now focus on a region of space outside the source we have $T = 0$, which allows us to impose the even stricter transverse-traceless gauge, defined by the following 2 conditions:

$$h_{\mu\nu}{}^{,\nu} = 0 \ \ (transverse)$$
$$h_{\mu}{}^{\mu} = 0 \ \ (traceless) \tag{1.8}$$

This also assures that the trace-inversed strain $\tilde{h}_{\mu\nu}$ is identical to the physical strain $h_{\mu\nu}$.

1.1.3 Plane wave solution and effect on free masses

To visualize the effect of a gravitational wave on free (inertial) masses in space we can look at a plane wave solution of equation 1.7 with wave vector k_λ:

$$h_{\mu\nu}(x^\lambda) = \bar{h}_{\mu\nu} \cos\left(k_\lambda x^\lambda\right) \tag{1.9}$$

We have $k_\lambda k^\lambda = 0$ since solutions of 1.7 travel at light speed and $\bar{h}_{\mu\nu} k^\nu = 0$, $\bar{h}_\mu^\mu = 0$ due to the transverse traceless condition 1.8. Choosing the wave vector k_i along the z-axis we can parametrize the amplitude $\bar{h}_{\mu\nu}$ as

$$\bar{h}_{\mu\nu} = \begin{pmatrix} 0 & 0 & 0 & 0 \\ 0 & h_+ & h_\times & 0 \\ 0 & h_\times & -h_+ & 0 \\ 0 & 0 & 0 & 0 \end{pmatrix} \tag{1.10}$$

i.e. we have two independent polarizations, h_+ and $h_\times$. Let's further assume 2 test masses separated by the distance L along the X-axis before the wave hit. The test

mass separation while the wave is passing is then given by

$$L + dL = \sqrt{L g_{xx} L} \approx \left(1 + \frac{h_+}{2}\right) L \tag{1.11}$$

while we get a minus sign for a separation along the y-axis. In other words a gravitational wave with h_+ polarization stretches distances along the x-axis and shortens distances along the y-axis during the first half period and does the opposite during the second half period. The $h_\times$ polarization does the same thing, but in a coordinate system rotated by 45 degree.

The best way of measuring a gravitational wave strain therefore is to compare the arm length difference between two perpendicular arms. Choosing the two arms along x and y-axis the arm length difference is given by

$$L_x - L_y = h_+ L \tag{1.12}$$

Comparing the length of two perpendicular arms conveniently is exactly what a Michelson interferometer does.

1.2 Gravitational Wave Sources

1.2.1 Quadrupole radiation and signal strength

Just as electric charge conservation implies that there is no electromagnetic monopole radiation, the energy-momentum conservation $T^{\mu\nu}_{;\nu} = 0$ implies that there is no monopole or dipole gravitational radiation. Working in the near Newtonian approximation $T^{\mu\nu}_{;\nu} = 0$ implies in particular the identity

$$\int dx^3 T^{jk} = \frac{1}{2} \frac{d^2}{dt^2} \int dx^3 T^{00} x^i x^j. \tag{1.13}$$

21

Since equation 1.7 is a regular wave equation its far field solution at distance d is the retarded field given by

$$\tilde{h}_{ij} = \frac{4G}{d} \int dx^3 T_{\text{ret}}^{ij} \tag{1.14}$$

Applying identity 1.13 and projecting to the transverse traceless gauge we get

$$
\begin{aligned}
h_{ij}^{TT} &= \frac{2G}{dc^4} \frac{d^2}{dt^2} I_{ij,\text{ret}}^{TT} \\
&= 1.7 \times 10^{-47} \left(\frac{\frac{d^2}{dt^2} I_{ij,\text{ret}}^{TT}}{1 \text{ Watt}} \right) \left(\frac{1 \text{ km}}{d} \right) \\
&= 9.6 \times 10^{-20} \left(\frac{\frac{d^2}{dt^2} I_{ij,\text{ret}}^{TT}}{M_\odot c^2} \right) \left(\frac{1 \text{ Mpc}}{d} \right)
\end{aligned}
\tag{1.15}
$$

where $I_{ij,\text{ret}}^{TT}$ is the retarded transverse traceless part of the quadrupole momentum $I_{ij} = \int dx^3 \rho(x) x^i x^j$. From equation 1.15 it is also immediately clear that there is no chance of observing gravitational waves from a terrestrial source. The strain h_{ij}^{TT} is also related to the radiated energy density through

$$\rho_{gw} = \frac{c^2}{32\pi G} \left\langle h_{ij,0}^{TT} h_{ij,0}^{TT} \right\rangle = \frac{c^2}{16\pi G} \left\langle |h_{+,0}|^2 + |h_{\times,0}|^2 \right\rangle \tag{1.16}$$

The result has to be averaged over several wavelength to be physically meaningful, which is indicated by the angle brackets $\langle ... \rangle$. Finally the power radiated by the whole source can be obtained by integrating over all directions

$$
\begin{aligned}
P &= \frac{G}{5c^5} \left\langle \dddot{I}_{ij}^{\text{traceless}} \dddot{I}_{ij}^{\text{traceless}} \right\rangle \\
&\approx \frac{G}{c^5} P_{\text{internal}}^2 \\
&\approx \frac{P_{\text{internal}}^2}{3.6 \times 10^{59} \text{erg/sec}}
\end{aligned}
\tag{1.17}
$$

so the radiated power is proportional to the square of the power P_{internal} flowing internally from one side of the source to the other.

The existence of gravitational waves has been confirmed indirectly by Hulse and Taylor [2, 3, 4], resulting in the 1993 Nobel Prize in Physics. They observed a shift

in the perihelion passing time of the binary pulsar system PSR 1913+16 that was perfectly explained by the loss of energy and angular momentum due to the emission of gravitational waves.

1.2.2 Expected astrophysical sources

Inspiral of a compact binary

Any two stars orbiting each other will loose energy by radiating gravitational waves at a rate given by

$$\frac{dE}{dt} = -\frac{32}{5}\frac{c^5}{G}\frac{\mu^2 M^3}{a^5}f(\epsilon) \tag{1.18}$$

where $M = M_1 + M_2$ is the total mass, $\mu = M_1 M_2/M$ the reduced mass, a the semi-major axis and

$$f(\epsilon) = [1 + \frac{73}{24}\epsilon^2 + \frac{37}{96}\epsilon^4 + O(\epsilon^6)][1 - \epsilon^2]^{-7/2} \tag{1.19}$$

is a correction for non-zero eccentricity ϵ (see [7], page 988). Thus both period and semi-major axis a will shrink resulting in a chirp with $\dot{f} \propto f^{11/3}$, with the gravitational wave frequency f equal to twice the orbital frequency. The 2 stars merge when the sum of their radii becomes comparable to their separation, $R_1 + R_2 \approx 2a$. Thus the chirp signal ends roughly at

$$\begin{aligned}
f_{\max} &= \sqrt{\frac{8GM}{\pi^2(R_1 + R_2)^3}} \\
&= 15 \text{ Hz} \left(\frac{1000\text{km}}{R_1 + R_2}\right)^{\frac{3}{2}} \left(\frac{M}{2M_\odot}\right)^{\frac{1}{2}}.
\end{aligned} \tag{1.20}$$

Even if only one of the stars is a white dwarf ($R_1 \approx 10^6 m$, $M_1 = M_\odot$) this frequency is already outside the band accessible to LIGO (starting roughly above 40Hz, see chapter 2). Thus LIGO can only see binary inspirals where both stars are either a neutron star (NS, $R_i \approx 10^4 m$, $M_i = 1.4M_\odot$) or a black hole (BH, $R_i \approx R_{\text{ISCO}} = 6GM_i c^{-2}$).

In both cases $f_{\max}$ can be as high as about 6 kHz.

During the inspiral phase the NS/NS wave forms are believed to be sufficiently well modeled by post-Newtonian approximation that they can be used for matched filtering [21, 89]. For BH/BH wave forms the confidence is not as big [22]. Nevertheless matched filtering is usually applied.

All of these post-Newtonian wave forms become inaccurate during the final phase (merger). So far no accurate wave forms for the merger phase is known. This is especially unfortunate since the radiated power reaches a maximum during this merger phase. The product of such a merger is most likely a black hole. Just after being born this black hole will still be excited and undergo damped oscillations that will also radiate gravitational waves [18].

NS/NS inspiral rate estimate

The NS/NS merger rate in our Galaxy was estimated to be about 83 Myr^{-1} using a population model that was based on all known NS/NS systems [23, 24]. The uncertainty on this estimate is rather large - the 95 % interval spans values from 4 Myr^{-1} to 220 Myr^{-1}. This translates into a detection rate ($SNR > 8$) for LIGO at design sensitivity of 1 per 30 years, with the most optimistic value consistent with the 95 % interval being 1 per 8 years.

Periodic sources

Another potential source of gravitational waves are fast spinning non-axis-symmetric pulsars. Fast spinning pulsars are often referred to as Millisecond Pulsars because their period is only a couple milliseconds long. These sources will produce a monochromatic signal at twice the pulsar frequency. The strength of such a signal is about

$$h \approx 6 \times 10^{-26} \left(\frac{f_{gw}}{500 \text{ Hz}} \right)^2 \left(\frac{10 \text{ kpc}}{d} \right) \left(\frac{\epsilon}{10^{-6}} \right) \qquad (1.21)$$

where ϵ is the ellipticity of the pulsar. Since the pulsar frequencies are extremely stable the best way to look for such signals is to demodulate the data stream at

the expected frequency, taking into account all effects from polarization and orbital motion of both pulsar and earth.

The most interesting pulsars naturally are the fast spinning ones. Those tend to be driven by mass accretion, which in turn can affect the frequency stability. For those objects on can also relate the expected gravitational radiation to the observed X-ray luminosity, see section 3.2.1.

Other sources

Gravitational waves for which we do not have a template can come from a variety of sources. These include the superposition of an ensemble of the sources described above as well as any other inaccurately modeled sources such as supernovae or even primordial gravitational waves.

Phenomenologically one usually divides those sources into bursts and stochastic background, depending on whether they have a finite duration. The boundary between long bursts and a stochastic background however is not well defined. More details on a stochastic background are given in chapter 3.

1.3 Gravitational Wave Detectors

A gravitational wave detector must be able to convert a space-time strain into a recordable signal. The whole challenge lies in the weakness of the signal. This section recalls the history of suggested detectors and motivates the optical configuration of the LIGO interferometers.

1.3.1 Bar detectors

In 1960 Joseph Weber suggested using the resonance of an aluminum bar as an antenna for gravitational waves [25]. The idea is that a passing short gravitational wave pulse would induce a strain in the bar and excite its resonance. For reasons detailed elsewhere[26, 27], the community was never able to verify Weber's subsequent

claims of detection[28] although various theories[19, 20] were developed to explain the enormous apparent flux of gravitational wave energy.

Since Weber's pioneering work resonant bar detectors have come a long way. Today's bar detectors are cryogenically cooled, have much improved seismic isolations and make use of SQUIDs to readout the signal [29].

The sensitivity on resonance of such a bar with length l_0, mass m, resonance frequency f_0 and mechanical quality factor Q is limited by thermal excitation of the bar resonance

$$
\begin{aligned}
h_{\text{therm}} &\approx \frac{4}{l_0}\sqrt{\frac{k_B T}{8\pi^3 f_0^3 m Q}} \\
&\approx 3\times 10^{-23}\text{Hz}^{-\frac{1}{2}}\left(\frac{T}{1\text{mK}}\right)^{\frac{1}{2}}\left(\frac{10^6}{Q}\right)^{\frac{1}{2}}\left(\frac{10^3\text{kg}}{m}\right)^{\frac{1}{2}}\left(\frac{10^3\text{Hz}}{f_0}\right)^{\frac{3}{2}}\left(\frac{1\text{m}}{l_0}\right).
\end{aligned}
\tag{1.22}
$$

This follows from the strain-to-amplitude ($h \to \Delta l$) transfer function

$$
\Delta l = \frac{f^2 \frac{1}{2} l_0 h}{f^2 - f_0^2 - i\frac{f f_0}{Q}}
\tag{1.23}
$$

and the Fluctuation-Dissipation theorem, implying

$$
\Delta l_{\text{therm}}^2 df = \frac{\frac{k_B T f_0}{2\pi^3 Q m}}{\frac{f^2 f_0^2}{Q^2} + (f^2 - f_0^2)^2} df
\tag{1.24}
$$

(see for instance [8]).

In recent years there also have been proposals [30] for more sophisticated geometries (spheres, dodecahedrons, etc.) designed to improve the bandwidth and directional sensitivity of the resonant mass detectors [31].

1.3.2 Interferometers

Given the effect of a passing gravitational wave (eq. 1.12) a Michelson interferometer is the canonical instrument to measure such an effect. This was first pointed out by Pirani in 1956 [33] and by 1971 a prototype interferometer was built in Malibu [34].

Shortly after that a study done at MIT by R. Weiss identified almost all noise sources relevant for a LIGO-scale interferometer [37, 38].

Since then many different optical configurations have been suggested (see [55] for a summary). The LIGO antennae are power-recycled Fabry-Perot Michelson interferometers. All of today's kilometer-scale interferometers are a variant of this optical configuration [40, 41, 42, 45, 46].

1.3.3   Remark on interferometer for GW detection

Quoting the analogy to the Cosmic Microwave Background ("the wavelength gets stretched with redshift"), I was often asked whether such a wavelength stretching would not null out any interferometric readout. Hence this short paragraph:

At its heart an interferometric measurement is not a distance measurement but rather a relative timing (or time-of-flight) measurement - it compares the phase of the light reflected from both arms at the fixed location of the photo diode. Furthermore, since $h_{tt} = 0$ for all gravitational waves (see 1.10), the evolution of time is not affected by the wave. In other words, a set of clocks that was synchronized before the wave arrived remains synchronized during the event and afterward. Therefore we should analyze the interferometer as follows: A phase front $\Phi = const$ starts at the beam splitter, gets split up and travels with light speed (hence the name...) down each arm, gets reflected at each end and arrives back at the beam splitter after

$$\Delta t_{x,y} = 2\frac{(1 \pm \frac{h_+}{2})L}{c} \tag{1.25}$$

i.e. the relative time delay between the 2 arms is $\Delta t = 2\frac{h_+ L}{c}$, which then translates into a phase difference of $\Delta\Phi = 2\pi\nu\Delta t$. The laser frequency ν is unaffected by the gravitational wave ($h_{tt} = 0$).

The analysis above is for the limit of long gravitational wave length (gravitational wave period > light storage time in the arms). The generalization to a time and

position dependent $h_+(t, \vec{x})$ is straightforward and gives

$$\Delta t = \int_0^{\frac{2L}{c}} \left(\frac{h_+(t, \vec{x}(t))}{2} + \frac{h_+(t, \vec{y}(t))}{2} \right) dt \tag{1.26}$$

where $\vec{x}(t)$ / $\vec{y}(t)$ is the position of the phase front in the x-arm / y-arm.

Notice that I never had to talk about the laser wavelength. Nevertheless, it is still legitimate to academically ask what happens to the laser wavelength when a gravitational wave passes. The wavelength is the distance between two points that have a phase difference of 2π. In the static case $h_+ = const$ and for a newly emitted photon, since the light speed is exactly what it's name suggests, this distance is always given by $\lambda = c/\nu$, independent of h_+. If however $h_+(t)$ depends on t one can show that the laser wavelength λ becomes

$$\lambda = \frac{c}{\nu} \left(1 + \frac{1}{4\nu} \frac{\partial h_+}{\partial t} \right) \tag{1.27}$$

in 1st order approximation, i.e. it is indeed stretched if h_+ increases. This however does *not* result in a correction to equation 1.26 and hence to the strain signal provided by a interferometer.

Chapter 2

The LIGO interferometer

Figure 2-1: **Aerial photograph of the LIGO Hanford Observatory**

An excellent summary of the control system and the relevant noise sources was given by Rana Adhikari in his thesis [51]. It captures the state of the LIGO interferometers during the S2 science run. Also, the instrument status during the S1 science run is summarized in [49].

This chapter is intended to be an update covering the changes in the control system and newly identified noise sources. It is intended to capture the state of the LIGO interferometers at the beginning of the 1-year long S5 science run, even though not all aspects of the LIGO instrument will be covered. At this point all three interferometers show roughly one order of magnitude improvement in sensitivity everywhere above 40Hz compared to S2.

Thus I will begin this chapter with a description of the optical layout and the RF readout scheme. I then will move on to the fundamental noise source limiting initial LIGO, namely shot noise, and explain a series of technical noise sources that had to be eliminated during commissioning. After that a big section is filled by the detailed description of the thermal compensation system that had to be installed to deal with thermal aberration in the large optics. Finally I will summarize all the known noise sources that contribute to the interferometer displacement sensitivity.

2.1   Optical layout

The three initial LIGO interferometers [43, 44] are all power-recycled Michelson interferometers [36] with Fabry-Perot arm cavities [32] (see figure 2-2). Two of them, one with 4 km and one with 2 km arm length (labeled H1 and H2), are installed at the LIGO Hanford Observatory in Washington State. The third one (L1) also has an arm length of 4 km and is installed at the LIGO Livingston Observatory in Louisiana.

On all interferometers all optics, including input mode cleaner and mode matching telescope mirrors, are freely suspended as pendula, hanging from a platform that is passively seismically isolated. All these optics and seismic isolation stacks are enclosed in a vacuum system. Also, the Livingston interferometer was recently upgraded with a Hydraulic External Pre-Isolation (HEPI) system, i.e. an active seismic isolation systems that is installed outside the vacuum envelope. All freely suspended optics have little magnets glued on. The required actuation forces are applied to those magnets using small coils.

The light source for a LIGO interferometer is a 10 Watt Nd:YAG laser from
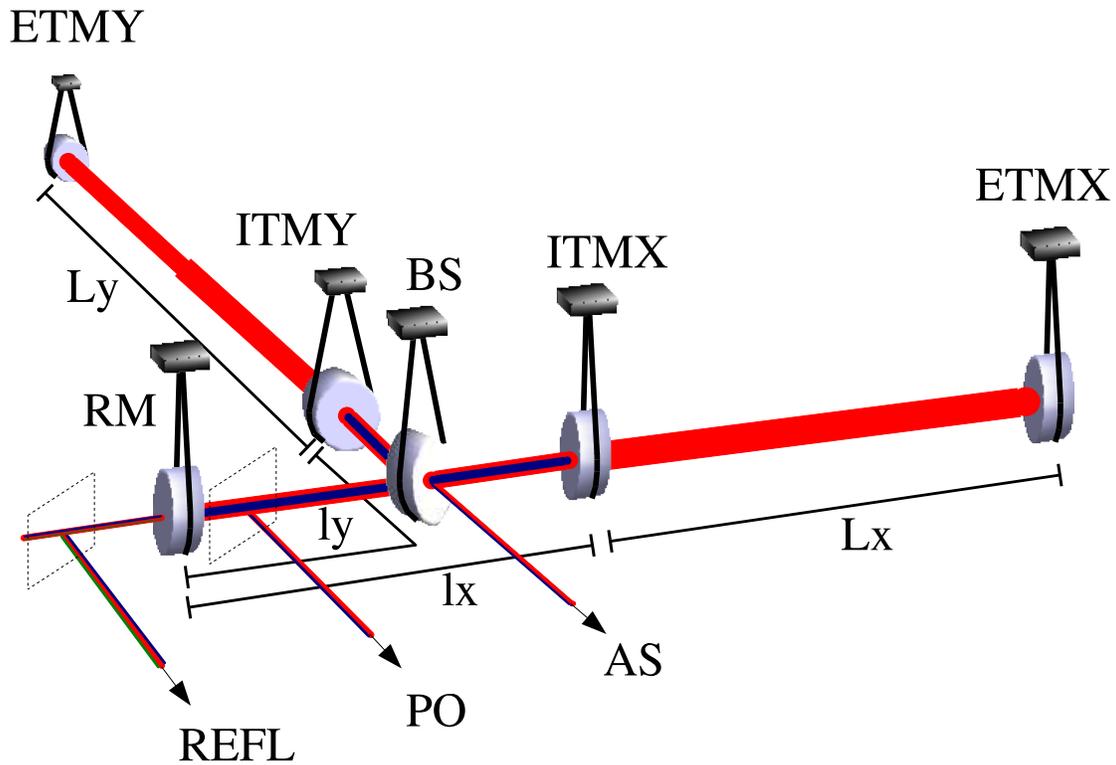
Figure 2-2: **Optical layout of the LIGO interferometers.** The Laser light enters from the left. The gravitational wave signal is sensed at the anti-symmetric or dark port (AS). Shown are the Recycling Mirror (RM), the Beam Splitter (BS), the two Input Test Masses (ITMX/ITMY) and the two End Test Masses (ETMX/ETMY). Carrier light is shown in red, the resonant sideband in blue and the non-resonant sideband in green (only reflected at RM). Indicated are also the reflective or symmetric port (REFL) and the pick-off port (PO), as well as the distances L_x, L_y, l_x and l_y.

Lightwave, operating at a wavelength of 1064 nm. It is both frequency and intensity stabilized. The output laser light is passed through the pre-mode cleaner, a 21 cm long triangular cavity designed to both filter the spatial mode and the intensity noise above about 1 MHz.

Most error signals for controlling the interferometer are derived using a Pondermotive locking scheme [35] (see section 2.2, or [48]). Thus the input laser beam is frequency-modulated at three different frequencies, producing three sets of sidebands at 24.48 MHz (resonant sideband), 61.20 MHz (non-resonant sideband) and 33.29 MHz (mode cleaner sideband). All but the mode cleaner sideband then pass the mode cleaner (MC), which is a triangular cavity with 24.492 meters round trip length. The mode cleaner sideband is used to lock the mode cleaner in reflection. The resonant sideband passes 2 free spectral ranges (FSRs) away from the carrier, the non-resonant sideband 5 FSRs away from the carrier.

The beam then hits the recycling mirror (RM), which is already part of the main interferometer, see figure 2-2. The non-resonant sideband is just reflected, it is not resonant in any of the cavities of the main interferometer - hence its name. Both carrier and resonant sideband build up in the recycling cavity that is formed by the RM and the 2 Input Test Masses (ITMX and ITMY). The recycling gain is $G_{cr} = 50$ for the carrier and $G_{sb} = 26.5$ for the sideband. Finally only the carrier is resonant in the arm cavities formed by the ITMs and the end test masses (ETMX and ETMY). The arm cavity finesse is $\mathcal{F} = 219$.

The beam splitter (BS) is placed such that (almost) no carrier is exiting at the antisymmetric port (AS or dark port). Due to the Schnupp asymmetry $l_x - l_y = 0.356m$ the sideband leaks out the dark port. Nominally the recycling cavity should be almost critically coupled for the sideband such that almost all sideband should end up on the dark port. The differential arm (DARM) error signal $L_x - L_y$ is derived from beating sideband and carrier at the dark port.

The common arm error signal $(L_x + L_y)/2$ (CARM) is derived from beating the carrier at the reflective port (REFL or symmetric port) against either resonant or non-resonant sideband. CARM is fed back to the laser frequency with 20 kHz control

loop bandwidth.

Finally error signals for both $l_+ = (l_x - l_y)/2$ (PRC; power recycling cavity length) and $l_- = l_x - l_y$ (MICH; Michelson degree of freedom) are derived from the carrier - resonant sideband beat at the pick-off (PO) port (see 2.2).

In this work I will assume that all the cavities are already on resonance (locked). The process of lock-acquisition would fill a chapter on its own. See [53, 54] instead.

All quoted values are for the Hanford 4km interferometer (H1).

2.2 Sensing matrix

All of the error signals used to control the LIGO interferometer are derived using a heterodyne scheme. Almost all length control signals are derived using the resonant sideband at 24.5 MHz, with the exception being the REFL port on some interferometers (currently L1) - it uses the non-resonant sideband at 61.2 MHz.

The sensing matrix element used to read out a differential arm (DARM or L_-) displacement, and hence to read out a Gravitational wave signal, is given by [47]

$$
\begin{aligned}
[L_- \rightsquigarrow AS\_Q] &= -\aleph\, g_{cr} t_{sb} r'_c \frac{1}{1 + if/f_c} k\, \delta L_- \\
&= 4.4 \frac{\text{Watt}_{\text{pk}}}{\text{nm}} \frac{P}{1\ \text{Watt}} \frac{1}{1 + if/f_c}\, \delta L_-.
\end{aligned}
\tag{2.1}
$$

where $\aleph = 4 j_0(\Gamma) j_1(\Gamma) P \cos \omega_m t$ is the gain prefactor, $j_i(\Gamma)$ are Bessel functions of the first kind, Γ is the modulation depth, P is the power into the interferometer, ω_m is the resonant sideband modulation frequency, g_{cr} is the carrier amplitude recycling gain, t_{sb} is the sideband transmission to the dark port, $r'_c = \pi/(2\mathcal{F})$ is the derivative of the arm cavity reflectivity with respect to round trip phase, f_c is the arm cavity pole, k is the light wave vector and $L_- = dx - dy$ is the differential displacement. Numerical values for those parameters are tabulated in appendix A. There is an additional factor $\frac{e\eta}{h\nu}\overline{d(t)\cos\omega_m t}$ to convert the signal into a demodulated photo current. Here $d(t)$ is the demodulation function (ideally a square wave), e the electron charge, h Planck's constant, ν the laser frequency and η the photo diode quantum efficiency.

Here I will just list the other relevant sensing matrix elements, more details can be found in [51] and [47]. Besides the element 2.1 used for DARM loop the elements used for the 3 other length control loops (CARM or L_+, PRC or l_+, MICH or l_-) are

$$[L_+ \rightsquigarrow REFL\_I] = 2\aleph \, g_{cr}^2 r_{sb} r'_c \frac{1}{1 + if/f_{cc}} k \, \delta L_+ \tag{2.2}$$

$$[l_+ \rightsquigarrow POB\_I] = 2\aleph \frac{g_{cr} g_{sb}}{t_{RM}} r_M r_c \left[g_{cr} \frac{1}{1 + i\frac{f}{f_{cc}}} - g_{sb} \right] k \, \delta l_+ \tag{2.3}$$

$$[l_- \rightsquigarrow POB\_Q] = -\aleph \frac{g_{cr} g_{sb}^2}{t_{RM}} t_M k \, \delta l_- \tag{2.4}$$

There are however significant off-diagonal couplings, namely

$$[L_+ \rightsquigarrow POB\_I] = -2\aleph \frac{g_{cr}^2 g_{sb}}{t_{RM}} r_M r'_c \frac{1}{1 + if/f_{cc}} k \, \delta L_+ \tag{2.5}$$

$$[l_+ \rightsquigarrow REFL\_I] = 2\aleph \left[g_{sb}^2 r_{cr} r_M + g_{cr}^2 r_{sb} r_c \frac{1}{1 + if/f_{cc}} \right] k \, \delta l_+ \tag{2.6}$$

$$[l_- \rightsquigarrow AS\_Q] = \aleph \, g_{cr} t_{sb} r_c \frac{1}{1 + if/f_c} k \, \delta l_- \tag{2.7}$$

Especially significant is the element $[L_+ \rightsquigarrow POB\_I]$ (2.5), it could actually dominate the POB_I. In practice the high bandwidth ($20kHz$ unity gain frequency) CARM loop zeros the $REFL\_I$ signal by acting on the laser frequency. Since $REFL\_I$ is also sensitive to l_+ through 2.6 this high bandwidth loop effectively changes the $l_+ \rightsquigarrow POB\_I$ element making it frequency independent:

$$[l_+ \rightsquigarrow POB\_I] = -2\aleph \frac{g_{sb}^2 r_M}{t_{RM} r_{sb}} [g_{cr} r_{sb} r_c + g_{sb} r_{cr} r_M] k \, \delta l_+ \tag{2.8}$$

Finally l_- also shows up in $REFL\_Q$.

$$[l_- \rightsquigarrow REFL\_Q] = -\aleph \, g_{sb} t_{sb} r_{cr} k \, \delta l_- \tag{2.9}$$

In practice however $REFL\_Q$ shows a large low frequency pollution that is thought to be due to the non-mode-matched component of the carrier field. In fact this large signal limits the amount of power we can detect at the REFL port since it gets close to saturation in the photo detector. This has actually forced us to change the L_+ readout on the Livingston interferometer to the non-resonant sideband. Since the non-resonant doesn't enter the recycling cavity it is not sensitive to motion of optics past the recycling mirror. In particular there cannot be any Q signal. In Livingston we now use a diode tuned for the non-resonant sideband at 61.2 MHz. The sensing matrix element is also given by equation 2.2, except that r_{sb} and $j_1(\Gamma)$ refer to non-resonant sideband values.

2.3 Shot Noise

The fundamental limit to detect the power at the dark port is the shot noise limit. Since the light at the dark port is dominated by the sidebands, effects from non-stationarity and demodulation have to be taken into account [64]:

$$
\begin{aligned}
S_P^{1-sided} &= \sqrt{2h\nu(2j_1^2 t_{SB}^2 P)\left[\frac{P_c}{P_{SB}} + \frac{\overline{d(t)^2 \cos^2 \omega_m t}}{\overline{d(t)^2}\ \overline{\cos^2 \omega_m t}}\right]} \left(\eta^{-\frac{1}{2}}\frac{\sqrt{\overline{d(t)^2}}}{\overline{d(t)\cos \omega_m t}}\right) \\
&= 2.8 \times 10^{-10}\frac{\mathrm{Watt_{pk}}}{\sqrt{\mathrm{Hz}}}\sqrt{\frac{P}{1\ \mathrm{Watt}}}
\end{aligned}
\tag{2.10}
$$

Here P is the power into the interferometer, $d(t)$ is the wave form used for demodulation (typically a square wave since the local oscillator is squared up in the demodulation boards) and η is the photo diode quantum efficiency - see table A.3 as well as section 2.2, paragraph 2 for the definition of the remaining symbols.

The factor in the last bracket is required to convert the shot noise into $\mathrm{Watt_{pk}}$ to be comparable with equation 2.1. The carrier to (both) sideband power ratio at the dark port was measured to be $P_c/P_{SB} \approx 0.09$ using an Optical Spectrum Analyzer. It is also related to the contrast defect $c_d = P_{\mathrm{carrier}}^{(\mathrm{beam\ splitter})}/P_{\mathrm{carrier}}^{(\mathrm{AS\ port})}$, which can be

expressed as

$$c_d = \frac{2j_1^2 t_{SB}^2}{j_0^2 g_{cr}^2} \frac{P_c}{P_{SB}} \approx 1 \times 10^{-4}. \tag{2.11}$$

Here I used the experimentally measured sideband transmissivity $t_s b \approx 0.77$.

Using equations 2.1, 2.10 and $\eta P = 4$ Watt the shot noise limited displacement sensitivity is

$$S_{DARM}^{1-sided} = \sqrt{\frac{h\nu}{2\eta P}} \frac{(1 + if/f_c)}{j_0 g_{cr} r_c' k} \left(\frac{\sqrt{\frac{P_c}{P_{SB}} \overline{d(t)^2} \, \overline{\cos^2 \omega_m t} + \overline{d(t)^2 \cos^2 \omega_m t}}}{\overline{d(t) \cos \omega_m t}} \right)$$
$$= 3.2 \times 10^{-20} \frac{\text{m}}{\sqrt{\text{Hz}}} (1 + if/f_c). \tag{2.12}$$

This is good agreement with the experimentally measured shot noise (see figure 2.9). In particular this means that the overlap of sideband and carrier at the AS port is quite good - that overlap was assumed to be ideal in eq. 2.12.

2.4   The AS_I signal

A recurring problem during the commissioning of LIGO was a large signal in the uncontrolled orthogonal quadrant of a demodulated photo diode signal. Such a signal limits the amount of detectable power because a saturation of the RF electronics and the mixer has to be avoided. The problem exists both on $REFL\_Q$ - where the solution was switching to the non-resonant sideband, see 2.2 - and on the AS port.

To get a signal in the I quadrature of the dark port an *effective* sideband imbalance at the dark port $\delta g_{SB} t_M$ and arm cavity reflectivity imbalance δr_c is required [51]. t_M is the transmissivity for the sideband to the dark port.

$$S_{\text{AS\_I}} = \frac{1}{4} \aleph \, g_{cr} t_M \, \delta r_c \, \delta g_{sb} \tag{2.13}$$

I say *effective* because contributions can come from higher order modes - I am using the arm cavities to define the modal basis since the almost flat-flat recycling cavity supports all modes. In particular almost any angular misalignments will produce an

AS_I signal by beating first order transverse modes. In fact even with all angular control loops closed we found a *linear* dependence of AS_I on angular mirror misalignment, indicating that at least a part of the DC AS_I signal is due to small offsets in the angular control loops.

The reflectivity imbalance δr_c for the fundamental mode comes from an imbalance in the round trip loss in the arms. For $l = 2$ a δr_c arises from arm cavity mode mismatch, both in beam width and beam curvature. The latter can be affected by changing the thermal lens in the ITMs (see 2.8).

Another hint that a significant contribution to the AS_I signal is due to higher order spatial mode comes from a test with an output mode cleaner (OMC) in the AS detection path. The OMC effectively strips off higher order spatial modes and thus their contribution to the readout signal. It reduced the DC offset in AS_I by a factor 9 and the RMS fluctuations in AS_I by a factor 3.

To quantify the size of the AS_I signal is hard because it depends on so many factors (alignment offsets and thermal lensing in ITM's). However a typical size of the DC signal in AS_I before any tuning of the interferometer is

$$S_{\text{AS\_I}} \approx 5 \times 10^{-3} \text{Watt}_{\text{pk}} \frac{P}{1 \text{ Watt}}. \tag{2.14}$$

This value can be tuned to zero by changing the differential thermal lensing in the ITMs (see 2.8) and/or some alignment offsets, affecting the $l = 2$ and/or $l = 1$ contributions to AS_I respectively. Based on this and equation 2.13 we can estimate the effective "$\delta r_c \times \delta g_{sb}$" to be roughly 0.02 in the untuned case. Note that the measured contrast defect $c_d \approx 1 \times 10^{-4}$ (section 2.3) limits the arm reflectivity imbalance to $\delta r_c = 2\sqrt{c_d} \approx 0.02$. However this measurement was done in a thermally tuned state.

I also want to point out that there is a natural mechanism that creates a sideband imbalance for higher order modes: the higher order mode pick up an additional phase shift from the arm. The arm cavity reflectivity of a sideband mode with mode number

l is given by

$$r_c = \left(-\frac{T_{ITM}\sqrt{R_{ETM}}e^{i\phi}}{1 - \sqrt{R_{ITM}R_{ETM}}e^{i\phi}} + \sqrt{R_{ITM}} \right)$$

$$\phi = 2\pi\frac{\pm f_{SB} - (l \times f_{TM})}{\text{FSR}} \tag{2.15}$$

$$f_{TM} = \frac{\text{FSR}}{\pi}\text{acos}\left((1 - L/\text{RoC}_{ITM})^{\frac{1}{2}}(1 - L/\text{RoC}_{ETM})^{\frac{1}{2}} \right).$$

$\pm f_{SB}$ is the (upper/lower) sideband frequency and f_{TM}, FSR, L, RoC are the arm cavity transverse mode spacing, free spectral range, length and optics curvature. That translates into a sideband recycling gain given by

$$g_{sb} = \frac{\sqrt{T_{RM}}}{1 - r_M r_c \sqrt{R_{RM}}} \tag{2.16}$$

In particular the values for the first 3 transverse sideband modes ($l = 0$: fundamental, $l = 1$: alignment mismatch and $l = 2$: mode mismatch) are given in table 2.1. In particular for the $l = 2$ bullseye mode the ratio between upper and lower sideband power becomes almost 2:1.

Higher order mode SB recycling gain				
	upper SB			
l	f_{off}	$\angle(r_c)$	$\|g_{sb}\|^2$	$\angle(g_{sb})$
0	-17.7 kHz	-0.074 deg	29.9	-2.4 deg
1	-6.1 kHz	-1.45 deg	17.8	-39.0 deg
2	+5.5 kHz	+1.65 deg	15.8	+42.6 deg
	lower SB			
l	f_{off}	$\angle(r_c)$	$\|g_{sb}\|^2$	$\angle(g_{sb})$
0	+17.7 kHz	+0.074 deg	29.9	+2.4 deg
1	-8.3 kHz	-0.98 deg	22.8	-28.9 deg
2	+3.3 kHz	+2.87 deg	8.1	+57.2 deg

Table 2.1: **Sideband recycling gain for different spatial modes.** f_{off} is the frequency offset from the arm resonance. The phase shift induced by the arm causes a sideband power imbalance of almost 2:1 for the $l = 2$ mode.

In practice the only way to avoid mixer saturations due to the large AS_I signal was to implement feed-back that cancels out the AS_I induced RF photo current on

the diode. The installed system has a range of $10V_{pk}$ through a coupling resistor of 1 kOhm, i.e. it can correct up to $10mA_{pk}$ photo current per diode. Allowing for a factor of 2 headroom to ride out seismic transients this means that we now need about 1 dark port photo diode per Watt into the interferometer. We are now running with 4 diodes. Without the AS_I servo we would need about 10 times as many diodes since 1 mA$_{pk}$ of photo current and an average transimpedance of about 1 kOhm results in 1 V$_{pk}$, which is about the slew rate limit of the MAX4107 op-amp at the photo detector output. Details about the AS_I servo are given in [51], appendix H.

2.5   Oscillator phase noise

As we increased the power into the interferometer to improve the high frequency sensitivity we started noticing a noise bump above about 1 kHz that was present in both the Livingston and the Hanford 4km interferometer, but with a somewhat different shape. The noise was as high as 4×10^{-18} m/$\sqrt{\text{Hz}}$ at 1 kHz, which is 10 times above the design sensitivity.

Eventually we were able to track this to phase noise of the 24.48 MHz RF oscillator that we used to modulate the input beam and as a local oscillator for the signal demodulation. At 1 kHz the our oscillator had about 6×10^{-7} rad/$\sqrt{\text{Hz}}$ and the transfer function to displacement turned out to be a surprisingly high 7×10^{-12} m/ rad (see figure 2-3).

2.5.1   Basic coupling

The coupling of oscillator phase noise to displacement noise is closely related to the large AS_I signal at the dark port. The basic coupling mechanism is simple - a jitter in the demodulation of the constant offset in AS_I produces noise in AS_Q. Fortunately there is a cancellation mechanism: since we are using the same oscillator to both modulate the light and demodulate the photo diode signal, any jitter on the oscillator should cancel out.

There are 2 ways to circumvent this cancellation. First, any noise introduced after

the split between the electro-optic modulator (EOM) path and the local oscillator (LO) path will couple directly into AS_Q with the strength

$$S_{\text{AS-Q}} = S_{\text{AS-I},DC}\delta\phi_N(f), \tag{2.17}$$

where $\delta\phi_N(f)$ is the differential phase noise between optical and LO path. This large sensitivity to the differential phase noise prompted us to redesign the RF distribution system. We now amplify the signal before we split it and make sure we never dip below -1dBm LO level to avoid thermal noise. As oscillator we use a Wenzel Crystal oscillator with 10dBm output and and a phase noise specification of -140dBc/Hz at 100Hz,-155dBc/Hz at 1kHz and -162dBc/Hz at 10kHz. The thermal (Johnson) noise thus would degrade the LO signal at -168dBm/Hz (Johnson noise) - (-162dBc/Hz) + 5dB (amplifier noise figure) = -1dBm. The noise figure I quote is for the Mini-Circuits ERA-5 RF amplifier that we use in the demodulation boards.

The second way to avoid the cancellation is to introduce a relative phase shift between the 2 paths. A simple path length difference is not large enough - the difference between the 2 paths is about 5 meters resulting in a relative phase shift of only 1×10^{-4}radians at 1kHz. The optical cavities in the light path however can produce a significant phase shift.

Figure 2-3 shows the measured transfer function from oscillator phase noise to displacement. As expected it rises as f^2 below about 2 kHz (see figure caption 2-3). But there is clearly a pole somewhere between 2.5 kHz and 3kHz (3dB point after correction for the cavity pole). Plus there are 2 resonances at 3.3 kHz and 5.5kHz corresponding to the spatial $l = 2$ sideband modes resonating in the arms.

The obvious element that can introduce a phase shift in the optical path is the mode cleaner (MC). The sidebands are passed through the mode cleaner 2 free spectral ranges higher and lower. It has a pole frequency of 4.5 kHz (full width of 9 kHz). This is a bit too high for what is observed in the transfer function. Moreover an attempt to filter the LO with a 9 kHz wide crystal filter showed hardly any effect on the transfer function. Neither did detuning the mode cleaner and changing the
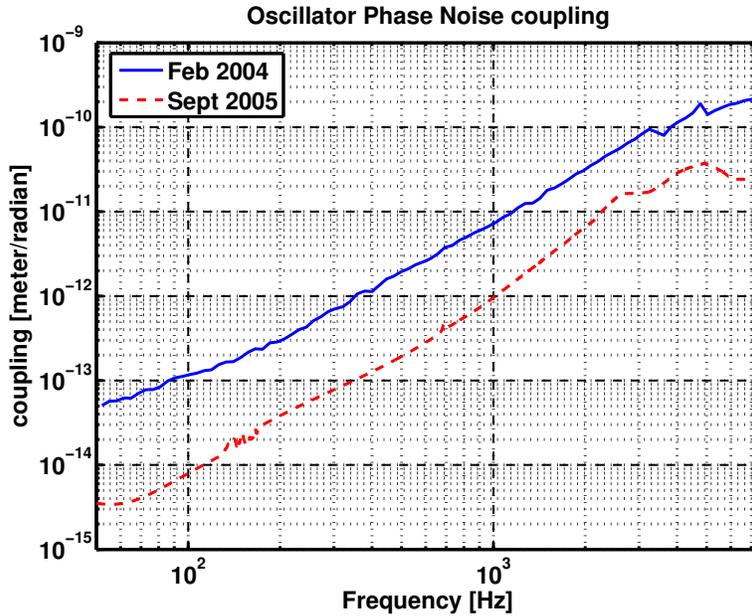
Figure 2-3: **Measured transfer function oscillator phase noise → displacement.** The solid Feb 2004 trace was taken before any thermal tuning and with the old ITMX. The dashed Sept 2005 trace was taken after the ITMX was replaced and in a thermally tuned state. Below about 2kHz the traces rise as f^2 - one power of f is due to a zero at the cavity pole of 85Hz (barely visible), the other comes from the phase noise cancellation effect. In the Feb 2004 trace 2 resonances are visible at 3.3 kHz and 5.5kHz. They are due to (spatial) $l = 2$ sideband modes becoming resonant in the arms (see table 2.1). This was confirmed by slightly changing the main modulation frequency - the resonances move in opposite directions.

modulation frequency at the same time to force a sideband imbalance.

The only other cavity in the path is the recycling cavity, but taken alone its cavity pole is at 71 kHz. This, however, is not accurate when the arms are aligned and the double cavity resonance must be considered.

2.5.2 The double cavity as seen by the sideband

When the arms are aligned and the interferometer is locked, the laser light sees an effective three-mirror cavity formed by RM, common ITM and common ETM, which is referred to as double cavity. For the carrier this double cavity has a pole frequency f_{DC} (half the FWHM line width) of

$$f_{DC} \approx f_c \frac{1 - \sqrt{R_{RM}} \, |r_c|}{2} \approx 1 \text{ Hz} \tag{2.18}$$

where $f_c = 85$ Hz is the arm cavity pole frequency, $R_{RM} = 0.973$ is the recycling mirror power reflectivity and r_c is the arm cavity amplitude reflectivity [52]. The pole frequency is so low because the double cavity round trip phase shift $\partial \phi_{DC}/\partial f$ for the carrier is dominated by the arm reflectivity change (equation 2.19, line 1, $\partial \phi_{ARM}/\partial f$ and $\partial \phi_{RM}/\partial f$ are arm cavity and recycling cavity round trip phase shifts).

The (resonant) sideband on the other hand is close to anti-resonant in the arms. However it turns that $\partial \phi_{DC}/\partial f$ is *still* dominated by the arm reflectivity change, even though this term is reduced by $r_c'^2$ compared to the carrier (equation 2.19, line 2).

$$\frac{\partial \phi_{DC}}{\partial f} \approx \begin{cases} r_c' \frac{\partial \phi_{ARM}}{\partial f} + \frac{\partial \phi_{RC}}{\partial f} & \text{carrier} \\ \frac{1}{r_c'} \frac{\partial \phi_{ARM}}{\partial f} + \frac{\partial \phi_{RC}}{\partial f} & \text{sideband} \end{cases} \tag{2.19}$$

This effect of the arms is even bigger when the sidebands are close to resonant in the arms, which is the case for higher order spatial modes ($l = 1, 2$) (see table 2.1 and equation 2.15).

The resulting side band power recycling gain as a function of audio offset frequency for the sideband modes with $l = 0, 1, 2$ are shown in figure 2-4. The traces are

calculated with

$$f_{TM} = \frac{\text{FSR}}{\pi}\text{acos}\left((1 - L/\text{RoC}_{ITM})^{\frac{1}{2}}(1 - L/\text{RoC}_{ETM})^{\frac{1}{2}}\right)$$

$$\phi = 2\pi\frac{f \pm f_{SB} - (l \times f_{TM})}{\text{FSR}}$$

$$r_c = \left(-\frac{T_{ITM}\sqrt{R_{ETM}}e^{i\phi}}{1 - \sqrt{R_{ITM}R_{ETM}}e^{i\phi}} + \sqrt{R_{ITM}}\right) \qquad (2.20)$$

$$\phi_{RC} = 2\pi\frac{f \pm f_{SB}}{\text{FSR}_{RC}} + \pi$$

$$g_{sb} = \frac{\sqrt{T_{RM}}}{1 - \sqrt{R_{RM}}r_M r_c e^{i\phi_{RC}}}.$$

Clearly both the upper and lower sideband for the $l = 1, 2$ modes are sitting right
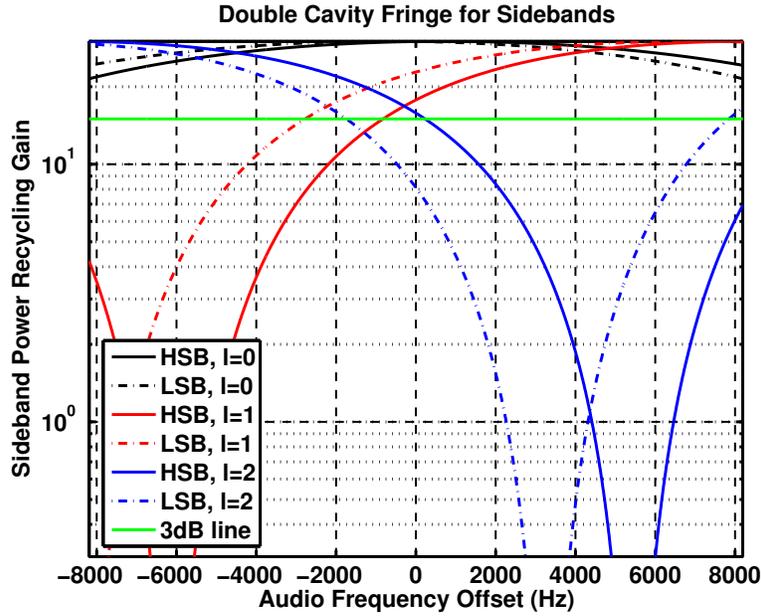
Figure 2-4: **Fringe of the double cavity as seen by higher order sideband modes ($l = 0, 1, 2$).** The fundamental mode sees a pole frequency of 12kHz and the upper and lower sideband are reasonably well balanced. For $l = 1$ and especially the $l = 2$ mode the sideband is sitting near the -3dB point and the lower sideband becomes completely anti-resonant at 3.3kHz offset.

on the side of the fringe. The most dramatic phase shift is seen by the $l = 2$ mode of the lower sideband.

Converting this fringe pattern into a transfer function can be a mess. All 3 modes

$l = 0, 1, 2$ will contribute depending on how much carrier power of each mode is at the dark port. Here I will just focus on $l = 2$ since it will lead to the lowest pole frequency. For $l > 0$ the carrier can actually have non-zero components in both quadratures since the length servo cannot zero them. In the $l = 2$ case these 2 components come from an arm phase front curvature mismatch and from an arm beam radius mismatch.

To work out the $l = 2$ contribution to the dark port noise of an oscillator phase modulation with modulation depth Γ at an audio frequency f, I start with an expression for the input beam with phase modulated sidebands:

$$\Psi = \tilde{C}_0 + S_0 \left(e^{+i(2\pi f_{SB} t + \Gamma \cos 2\pi f t)} + e^{-i(2\pi f_{SB} t + \Gamma \cos 2\pi f t)} \right) \tag{2.21}$$

Since the modulation Γ is assumed to be small I can use the approximation

$$e^{i\Gamma \cos 2\pi f t} = 1 + i\frac{\Gamma}{2} e^{+i2\pi f t} + i\frac{\Gamma}{2} e^{-i2\pi f t} \tag{2.22}$$

When this field is propagated through the mode cleaner and interferometer to the dark port each sideband term picks up the mode cleaner pole at 4.59 kHz plus a factor $i \; t_M \; g_{sb}^{\pm f_{SB} \pm f_{\text{audio}}}$. Here I use the notation $g_{sb}^{\pm f_{SB} \pm f_{\text{audio}}}$ to indicate the sideband recycling gain of the upper or lower ($\pm f_{SB}$) sideband with a positive or negative audio frequency offset ($\pm f_{\text{audio}}$). These are the quantities plotted in figure 2-4. Note that the $g_{sb}^{\pm f_{SB} \pm f_{\text{audio}}}$ are different for each spatial mode l, but I assume that all modes see the same mode cleaner pole, i.e. I assume that the mode mismatching happens after the mode cleaner.

I then assume that at the dark port the carrier is dominated by junk light that I

leave as a free (complex) parameter C_0. Thus the field at the dark port has the form

$$
\Psi = C_0 + i \ t_M t_{MC} S_0 \Bigg[+ g_{sb}^{+f_{SB}} \ e^{i2\pi(+f_{SB})t}
$$
$$
+ i\frac{\Gamma}{2} g_{sb}^{+f_{SB}+f} \ e^{i2\pi(+f_{SB}+f)t} + i\frac{\Gamma}{2} g_{sb}^{+f_{SB}-f} \ e^{i2\pi(+f_{SB}-f)t}
$$
$$
+ g_{sb}^{-f_{SB}} \ e^{i2\pi(-f_{SB})t}
$$
$$
+ i\frac{\Gamma^*}{2} g_{sb}^{-f_{SB}+f} \ e^{i2\pi(-f_{SB}+f)t} + i\frac{\Gamma^*}{2} g_{sb}^{-f_{SB}-f} \ e^{i2\pi(-f_{SB}-f)t} \Bigg].
$$

$$(2.23)$$

The mode cleaner transmission t_{MC} accounts for the mode cleaner pole.

The photo current at the dark port is proportional to $|\Psi|^2$, and it is demodulated with the local oscillator $\propto \cos(2\pi ft + \Gamma \cos 2\pi ft)$. This is where the cancellation effect mentioned above comes in. Carrying out this calculation, I find that the phase noise transfer function is proportional to

$$
\propto t_{MC} \big[\text{Carrier}\big]^*
$$
$$
\Big[(+g_{sb}^{-f_{SB}-f} + g_{sb}^{-f_{SB}+f} - g_{sb}^{+f_{SB}-f} - g_{sb}^{+f_{SB}+f} - 2 * g_{sb}^{-f_{SB}} + 2 * g_{sb}^{+f_{SB}}) \quad (2.24)
$$
$$
+ i(+g_{sb}^{-f_{SB}-f} - g_{sb}^{-f_{SB}+f} - g_{sb}^{+f_{SB}-f} + g_{sb}^{+f_{SB}+f}) \Big].
$$

Figure 2-5 shows this transfer function. The (scaled) data from Feb 2004 is overlaid on this plot, but one should keep in mind that the model transfer function is only one from several possible coupling paths ($l = 0, 1, 2, ...$ with 2 carrier quadratures each).

With all that said I should also mention that the oscillator phase noise is always good for surprises: at one point we changed the mode cleaner length of the Livingston interferometer by 1 mm because we wanted to use an in-house oscillator with a slightly different frequency. Somehow this change resulted in a 10-fold (!) increase of the oscillator phase coupling. The best explanation I have is that this somehow changed the amount of light coupled into higher order modes ($l = 1, 2$) after the mode cleaner.

The only way we were able to reduce the phase noise coupling was with the TCS system - see section 2.8.6. But even this only bought us a factor of a couple. So
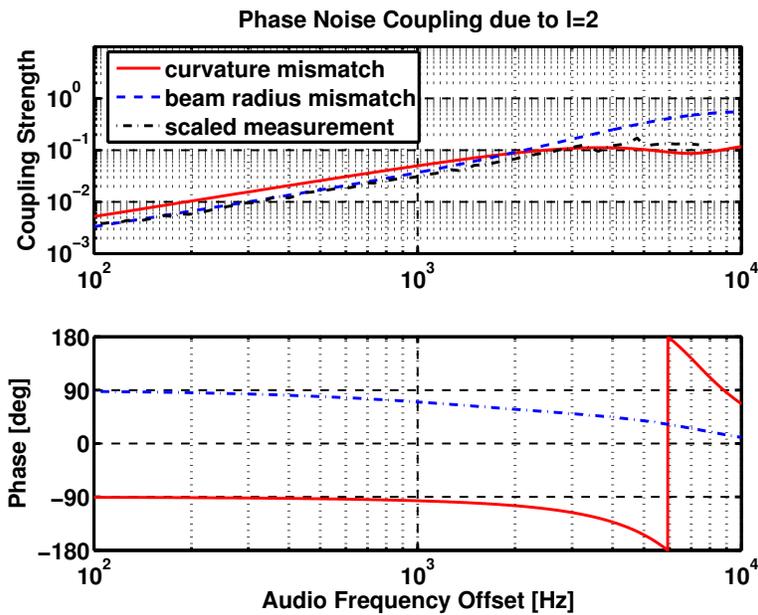
Figure 2-5: **Oscillator Phase Noise Transfer function** [oscillator phase modulation → photo diode power] due to the l=2 modes. The scale is chosen arbitrary because the strength depends on the amount of carrier power in the $l = 2$ mode. The mode cleaner (MC) pole at 4.5 kHz has also been included - note that the population of the $l = 2$ mode has to happen after the MC. Also shown is the arbitrary scaled measurement from Feb 2004.

we had to get a better signal generator - the one we were using had a phase noise performance of about 6×10^{-7} radians/$\sqrt{\text{Hz}}$. We installed an ultra-low noise crystal oscillator from Wenzel Associates, Inc. It has about 15 times less phase noise at 1kHz.

2.6 Oscillator amplitude noise

The oscillator amplitude noise is related to the oscillator phase noise because the individual audio sidebands see the same transfer function through the interferometer. There are however 2 key differences.

- There is no natural cancellation effect as for the phase noise. However the LO is squared up (saturated) before it is fed to the mixer, so amplitude fluctuations on the LO should not affect the demodulation.

- The basic coupling is given by $S_{\text{AS\_Q}} = S_{\text{AS\_Q},DC}\delta\Gamma_N(f)/\Gamma$. Since AS_Q is servoed to zero any coupling can only come from the remaining RMS value. This however is only true for the $l = 0$ mode and higher order modes will produce a signal similar to the phase noise coupling.

2.7 Noise Improvements below 100 Hz

2.7.1 The problem

After eliminating a couple of noise sources that were affecting frequencies below 100 Hz, such as noisy coil drive electronics and coupling from the local damping loops, it became clear that there was significant excess noise in the 40 Hz to 100 Hz band that was not explicable by linear noise prediction methods.

Ultimately we were able to pin down this noise to two sources. One part was coupled in from from excess noise in the poorly controlled auxiliary loops that held the beam splitter (BS) and recycling mirror (RM) in place (MICH and PRC loops). The other part was due to saturation effects in the RF amplifier at the output of the photo diodes.

Finding these two noise sources was complicated by the fact that they had roughly the same amplitude and shape, and a clear improvement was only obvious after both problems were fixed.

2.7.2   Auxiliary length control loops

Noise in the l_+ (PRC) and l_- (MICH) control loops for the recycling mirror (RM) and the beam splitter (BS) can couple to the interferometer L_- displacement signal. There are 2 different known coupling mechanisms (see [51]).

$$
\begin{aligned}
\delta L_-(f) &= \frac{r_c}{r_c'}\delta l_- \simeq \frac{1}{139}\delta l_- \\
\delta L_-(f) &= 2\delta r_c\frac{1}{r_c'}\frac{g_{sb}r_M}{t_{RM}t_M}\delta l_+(1+if/f_c)
\end{aligned}
\tag{2.25}
$$

The l_- coupling is straightforward - the dark port phase sensitivity to beam splitter motion compared to ETM motion is reduced by the arm cavity phase gain $r_c' = 2\mathcal{F}/\pi = 139$. The l_+ coupling comes from sidebands beating against the residual carrier at the dark port that is due to an arm reflectivity imbalance [51].

As always there are 2 ways to go about ameliorating this problem: reduce the noise and reduce the coupling.

2.7.3   Coupling reduction: MICH and PRC correction

Both MICH and PRC are limited by sensing noise in the band of interest (above ≈ 40 Hz), i.e. it is the control system that pushes the BS and RM. However we know both the noise and the coupling transfer function to DARM. Therefore we can send a scaled version of both the MICH and the PRC control signal to the ETMs to cancel out any linear coupling.

This trick, referred to as MICH and PRC correction, was amazingly successful, especially for the MICH loop because its coupling is well defined and does not change. A coupling reduction of up to 37dB was achieved with the MICH correction. For the PRC correction we had to fine-tune the frequency dependence - for unknown reasons

the coupling didn't quite follow the prediction (equation 2.25). After that we also got a reduction of about 20dB.

In practice the strength of the PRC coupling proved to be highly modulated on a time scale between about 0.1 Hz and 10Hz, presumably because the arm reflectivity imbalance is affected by angular seismic disturbances. The displacement noise floor will thus be very bursty if it is limited by PRC noise. Increasing the angular control system bandwidth indeed reduced these coupling fluctuations.

2.7.4 Auxiliary loop noise reduction

The goal of the auxiliary loops is to reduce the residual motion of BS and RM in the band of interest (above ≈ 40 Hz) as much as possible. Up to about 20 Hz there are a lot of environmental disturbances (seismic motion, coupling from angular degree of freedoms, suspension resonances such as bounce and roll mode) that jerk the optics around. Obviously we want as much gain as possible in that band in order to avoid saturation of the sensing electronics. However both auxiliary loops are shot noise limited at 100Hz at a level of a couple times 10^{-15} m/$\sqrt{\text{Hz}}$ (MICH) and 10^{-16} m/$\sqrt{\text{Hz}}$ (PRC).

Especially for MICH this was a problem: up to the S3 science run we didn't use the MICH correction, i.e. we polluted the DARM signal with noise at $\approx 10^{-15}$ m/$\sqrt{\text{Hz}} \times$ $\text{OLG}_{\text{MICH}}/139$ above 100 Hz, where OLG_{MICH} is the MICH open loop gain. Thus the MICH open loop gain had to be smaller than $\approx 1/100$ at 100Hz. This meant that the only possible way to get good sensitivity above 100 Hz was to choose a very low unity gain frequency (UGF) for the MICH loop (≈ 11 Hz) and add a steep low-pass filter with a cut-off at about 50 Hz. As a consequence we didn't have the desired gain below 20 Hz and lots of up-converted noise dominated the auxiliary loop error signals up to almost 100Hz (see also [51]). This noise also showed up in all angular loops where it used up almost all of our actuation range for the ETMs and ITMs because of the steep dewhitening filters for those optics.

The MICH correction's effective coupling reduction of -37dB allowed us to change the strategy completely. We now were able to run with a high UGF (≈ 70 Hz for
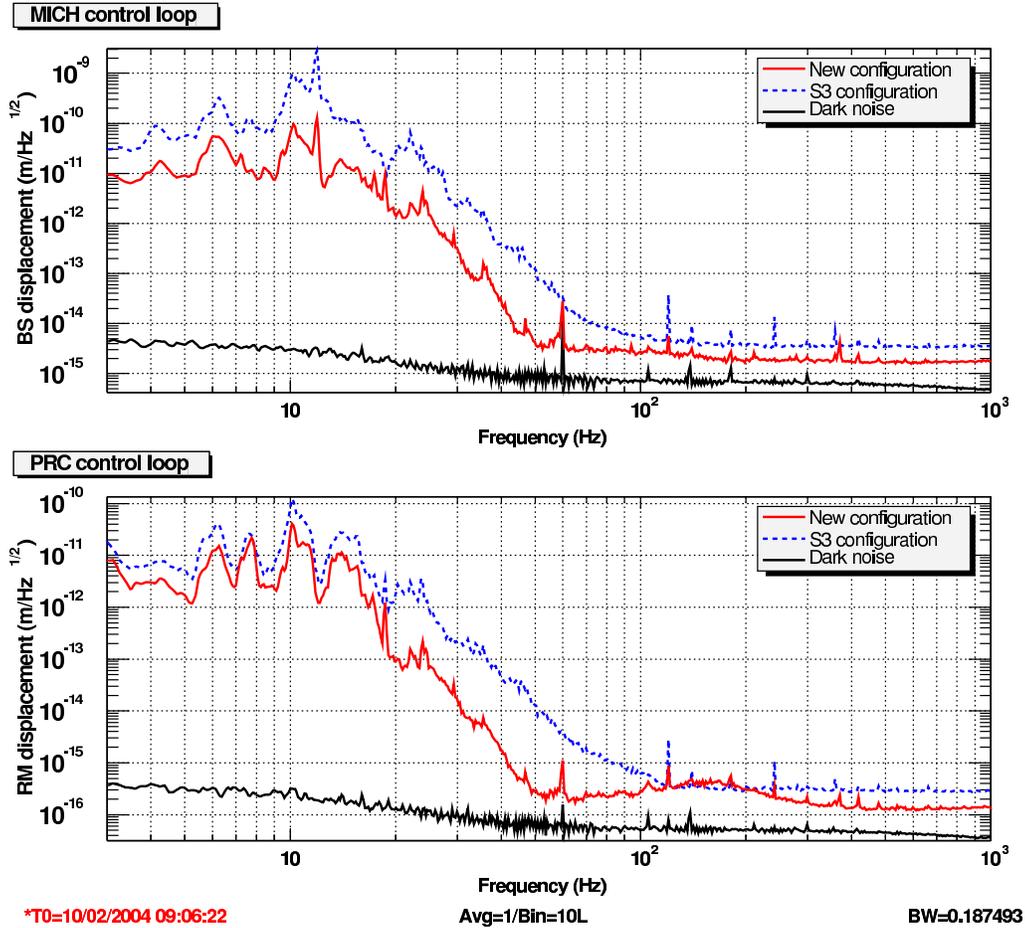
Figure 2-6: **Residual motion of the MICH (top) and the PRC (bottom) degree of freedom.** The dashed blue curves correspond to the S3 configuration with a very low MICH UGF. The solid red curves show the improvements that were made possible by the implementation of the MICH correction which allowed running with a higher loop gain (see text). The bump at about 150 Hz in the lower red trace is due to gain peaking in the PRC loop. This was later resolved by rolling off the BS and RM dewhitening filters at 160 Hz which in turn allowed moving the PRC control signal roll off up to 1kHz effectively increasing the phase margin. (The dewhitening filters are analog low-pass filters in the actuation chain and deal with the DAC noise.) The black curves show the level of the dark noise (thermal noise in the photo diode tank circuit above 40 Hz, ADC noise below that.

MICH, $\approx$ 110 Hz for PRC) which dramatically reduced the up-converted noise (see Figure 2-6). Additionally the reduced RMS signal at low frequency allowed us to detect all available power in the pick-off port - where it was possible we even used 2 pick-off ports. This lead to a further reduction of the shot noise in the auxiliary loops.

2.7.5   RF saturation at the photo diode output amplifier

Since the light at the anti-symmetric port is dominated by the sidebands, the by far biggest RF signal in the photo current is the sideband beat signal at twice the main modulation frequency of 24.48 MHz (2ω signal). To mitigate this, the photo diode tank circuit not only has a resonance at 24.48 MHz, but is also equipped with an about 40 dB deep notch at 48.96 MHz. After that the signal is amplified and shipped to the demodulation board in the electronics rack.

Unfortunately it turned out that, despite the notch at 48.96 MHz, the 2ω RF signal at this photo diode output amplifier was too big and was running into the slew rate limit, causing the up-converted noise that was visible in the DARM loop. The problem was mitigated by adding a notch, consisting of a coil and a trim-cap, in the feed-back path of the amplifier. This changed the total 2ω notch depth from about 40 dB to about 60 dB. After this fix, the RF signal at this photo diode output amplifier was no longer dominated by the 2ω signal, but rather by higher order modulation products for which we had no notch in the circuit.

With this fix in place and the auxiliary loops under high bandwidth control, the noise in the 40 Hz to 100 Hz band dropped by almost an order of magnitude. However there is still some noise left in this band that so far could not be successfully explained.

2.8　The Thermal Compensation System

2.8.1　The problem

The original design for the radius of curvature of the LIGO optics assumed a certain level of thermal lensing based on the estimated absorption and an anticipated power into the IFO of about 6 Watts. The absorption in the ITM's and ETM's is expected to be due to HR coating absorption (about 1 ppm [71]) and substrate absorption (4-5 ppm/cm).

As a result the LIGO interferometers had a slightly wrong radius of curvature in the ITM's and ETM's during the initial phase of commissioning (up to S2, after which we started increasing the input power). This is a tiny effect for the stable arm cavities. The arms define the spatial mode of the carrier, which therefore is only slightly affected. The biggest thermal lens though is generated in the ITM substrate. It mostly affects the sideband because the sideband only resonates in the recycling cavity which was designed to be marginally stable. Consequently the sideband mode size is critically dependent on the thermal lens.

In its cold state the recycling cavity is even unstable which gives rise to ring-shaped resonating modes and a significant reduction in power buildup due to mode mismatching and spill-over. We indeed only achieved a sideband recycling gain of $G_{sb} = 13$ at that time, while theoretically one expects about

$$G_{sb} = \left(\frac{t_{RM}}{1 - r_{RM} r_M} \right)^2 = 30 \tag{2.26}$$

(see appendix A).

When the input power was increased on H1, the sideband recycling gain increased dramatically, as expected. However, we reached a maximum of $G_{sb} = 26.5$ at only 1.8 Watt into the MC (≈ 1.2 Watt into the IFO). When going to higher powers G_{sb} came down again and the sideband mode was shrinking in size. This was a clear indication that the absorption in at least one optic of the recycling cavity was too high, though figuring out which one turned out to be non-trivial since reopening

the vacuum is costly. Using spot size measurements at several IFO ports and in different heating states [70] finally allowed us to conclude that ITMX had the biggest absorption, 34 ± 4 mWatt per Watt of power into the MC. ITMY had about 2.6 times less absorption , but that's still more than expected.

From these measurements it is impossible to know whether the absorption is in the bulk or on the coating. Since the power hitting the HR surface is 140 times bigger than what travels through the ITM, and since it seems impossible to accidentally pollute the interior of the mirror during the installation, it seemed likely that this excess absorption is on the surface. We have about 2275 Watt of arm power per Watt into the MC. The inferred coating absorptions therefore are 15 ± 1.8 ppm for ITMX and 5.6 ± 0.7 ppm for ITMY; the specification was less than 1 ppm. (If it were due to bulk absorption the numbers would be 210 ppm/cm for ITMX and 78 ppm/cm for ITMY; the specification was less than 5 ppm/cm.)

2.8.2 The hardware

A possible way to address this problem was shown by R. Lawrence in his thesis [67]. He studied the feasibility of a thermal compensation system for Advanced LIGO. Based on this work an upgrade Thermal Compensation System for initial LIGO was developed [68, 69].

Two Thermal Compensation systems were installed for each interferometer, one for each ITM. Each system consists of a 10 Watt CO_2 Laser ($10.6\mu m$ wavelength) that illuminates a switchable mask. Using a telescope with a magnification of 26.5 this pattern is then projected on to the HR surface of an ITM - the $10.6\mu m$ light is almost completely absorbed on the optic. We chose to illuminate the HR surface because of existing geometrical constraints - we would have preferred the AR surface because we expected it to be less sensitive to heating laser intensity noise. As mask we either use a ring (or annulus) pattern to compensate for too much heat deposited in the center by the main Laser ("cooling"), or a mask with a hole in the center to add more heat at the center of the optic ("heating") (see Figures 2-7 and 2-8). For practical reasons the central mask is actually installed in the Fourier plane of the
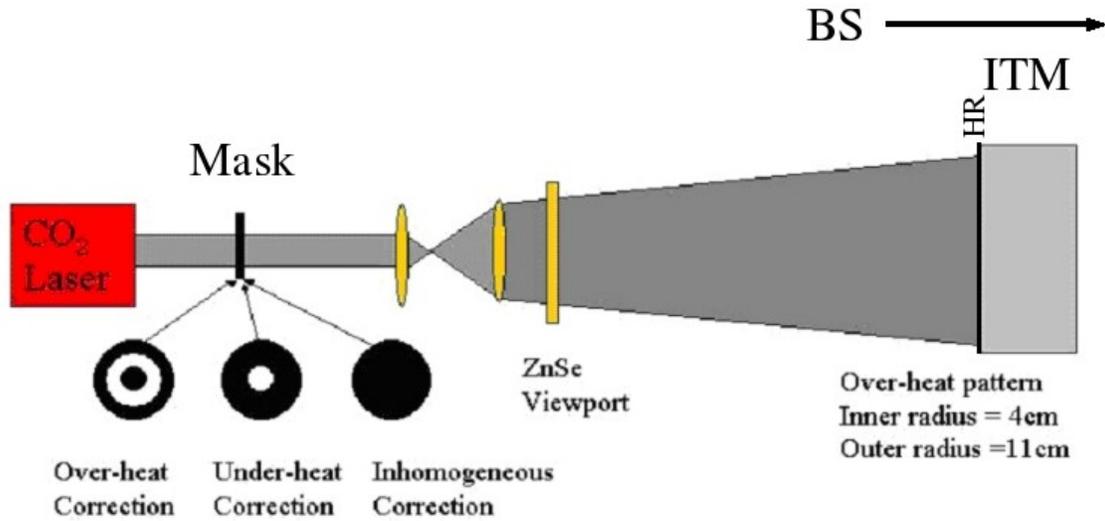
Figure 2-7: **A schematic of the Thermal Compensation System (TCS)** that was installed on both ITM's on all 3 interferometers. It consists of a $10.6\mu m$ CO_2 Laser, a set of masks and a projection system that produces an image of the mask on the optic. See text for more details.

projection system. A Bessel mask further downstream clips the higher order maxima of the Airy diffraction pattern, leaving only the central lobe of the Airy disk. It is a quite good approximation to the main laser Gaussian beam profile. A polarizer on a rotation stage was used to adjust the power.
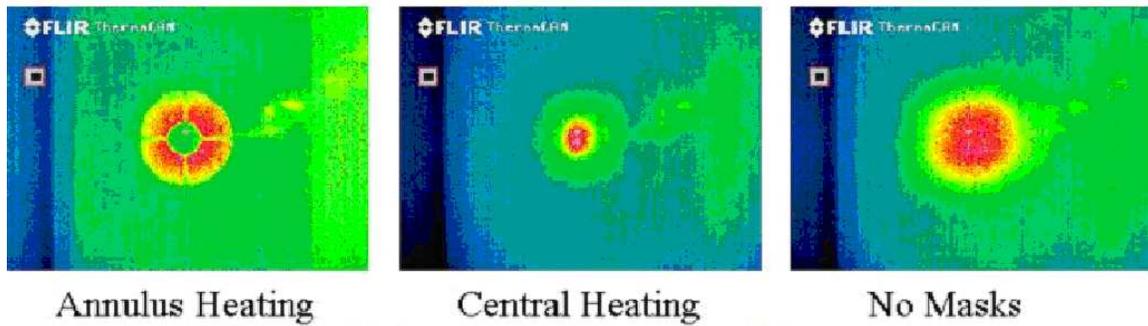
Figure 2-8: **Thermal images of the projected heating pattern** taken with an infrared camera in a test setup. From left to right the images were taken with an annulus mask, a central mask and no mask (illumination beam). The annulus mask image clearly shows the 4 spokes supporting the central part of the mask.

2.8.3 Time dependence of the thermal lens correction

There are two relevant time constants for the formation of the thermal lens. First there is the time to form the lens itself, given roughly by

$$\tau_{\text{therm}} = \frac{C\rho\,(\text{heated volume})}{(\text{conductive cooling})} = \frac{C\rho\left(\frac{2\pi}{3}w^3\right)}{2\pi\kappa w} \approx 10 \text{ min} \tag{2.27}$$

where κ is the thermal conductivity, C the specific heat and ρ the density (see Appendix A for numerical values for SiO_2). Then there is the time required to get the temperature across the whole optic into a stationary state, assuming only radiative cooling

$$\tau_{\text{stat}} = \frac{Cm_{\text{LOS}}}{(\text{radiative cooling})} = \frac{Cm_{\text{LOS}}}{(4A\sigma_B T_0^3)} \approx 3 \text{ hours} \tag{2.28}$$

$A = 0.13 \text{ m}^2$ is the surface area of the optic and $m_{\text{LOS}} = 10.5$ kg the mass of optic.

In order to get a more detailed understanding of the time dependence of the thermal lens induced by the new TCS system I numerically solved the heat diffusion equation

$$\frac{dT}{dt} = \frac{\kappa}{C\rho}\triangle T \tag{2.29}$$

using a simple finite difference 2-dimensional MATLAB code assuming cylindrical symmetry. Here T is the temperature field (deviation from ambient temperature T_0).

A surface heat source P_{heat} with the shape of the heating beam and linearized radiative cooling were used as boundary conditions:

$$C\rho\frac{dT}{dt}\bigg|_{\text{surface}} = P_{\text{heat}} - 4\sigma_B T_0^3 T \tag{2.30}$$

σ_B is Boltzmann's Constant. P_{heat} on the HR surface was modeled as a Gaussian beam with radius $w = 4$ cm (same as main interferometer beam on ITM) for the central heating case and as Gaussian beam with radius $w = 12$ cm, clipped at $r < 4$ cm and $r > 12.5cm$, for the annulus heating case. $P_{\text{heat}} = 0$ on all other surfaces.

Figure 2-9 shows snapshots of the temperature profile for the annulus heating case at different times. The CO$_2$ Laser was turned on at $t = 0$. The heat slowly propagates

toward the center of the optic. This is unfortunate since there it forms a convex lens that counteracts the intended concave one.
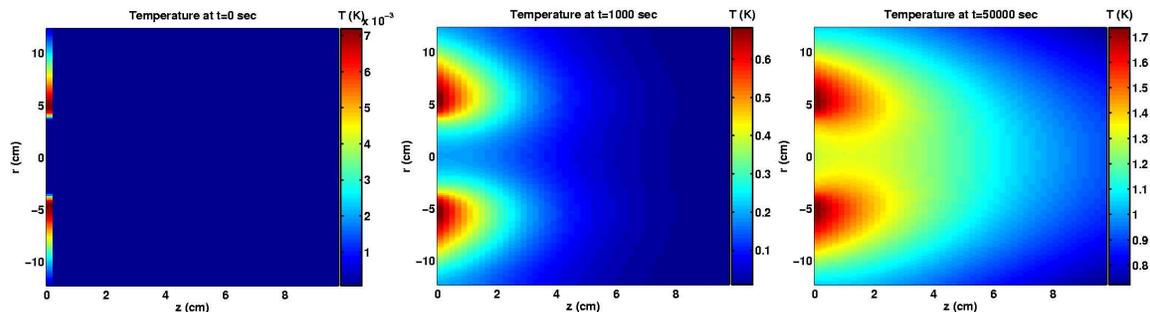
Figure 2-9: **Temperature profile** of a cross-section through the ITM at different times after the heat was turned on. The axis are radius (r) and depth (z). Initially the temperature profile forms a clean annulus pattern, but later on the heat propagates toward the center of the optic where it forms a lens with opposite sign and thus reduces the total efficiency.

The effective optical thickness of the thermal lens is given by

$$d_{opt}(r) = \left[(n-1)\alpha + \frac{dn}{dT} \right] \int dz T(r,z) \tag{2.31}$$

where α is the (linear) thermal expansion coefficient and dn/dT is the thermo-optic coefficient. Effects due to the the Poisson ratio are neglected since dn/dT is already the dominant term.

To convert this optical thickness into a lens power F, it is fitted with a quadratic function

$$d_{opt}(r) = \frac{1}{2}Fr^2 + \text{const} \tag{2.32}$$

taking into account only data points inside the beam radius of the main laser beam. The result is plotted in Figure 2-10. The lens power F peaks at 15min at a level of 9×10^{-5} m^{-1} and then drops by 45% with a time constant of 4.3 hours.

This long time constant posed a practical problem. In order to keep the interferometer at its desired operating point with a sideband recycling gain close to 30 it was now necessary to continuously adjust the compensation power for the first couple of hours of each lock. We thus needed a servo that can do this automatically. This servo
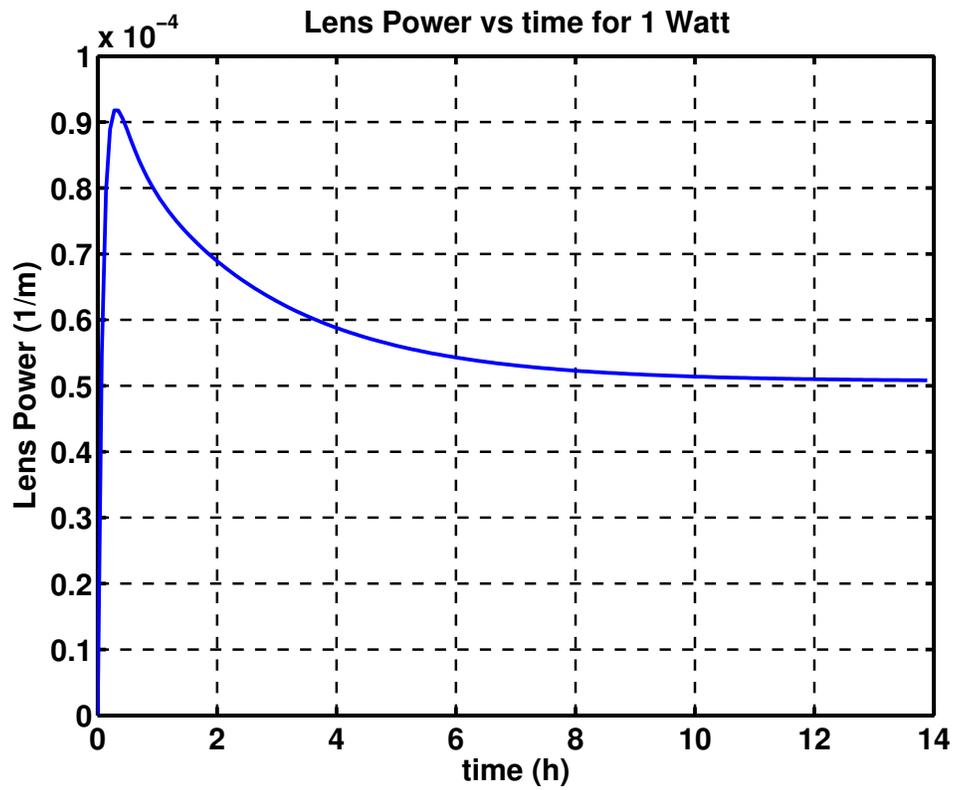
Figure 2-10: **Thermal lens power** F vs time for the annulus case. After peaking at 15min the lens power drops by 45% with a 1/e time constant of 4.3 hours.

is described in the next section, for now I will assume that we have such a servo.

In order to compare the model described in this paragraph to the real behavior of the interferometer I used the numerical code to compute the impulse response of the lens power F to a short burst of compensation power. (The Fourier transform of this impulse response is relevant for the servo system and is shown in Figure 2-12.) I then inverted this impulse response to get the required compensation power in order to keep a constant lens power F. This compensation power is plotted in Figure 2-11, together with the actuator output for a 12 hour lock during which the servo kept the interferometer at the optimal operation point. The agreement speaks for itself.
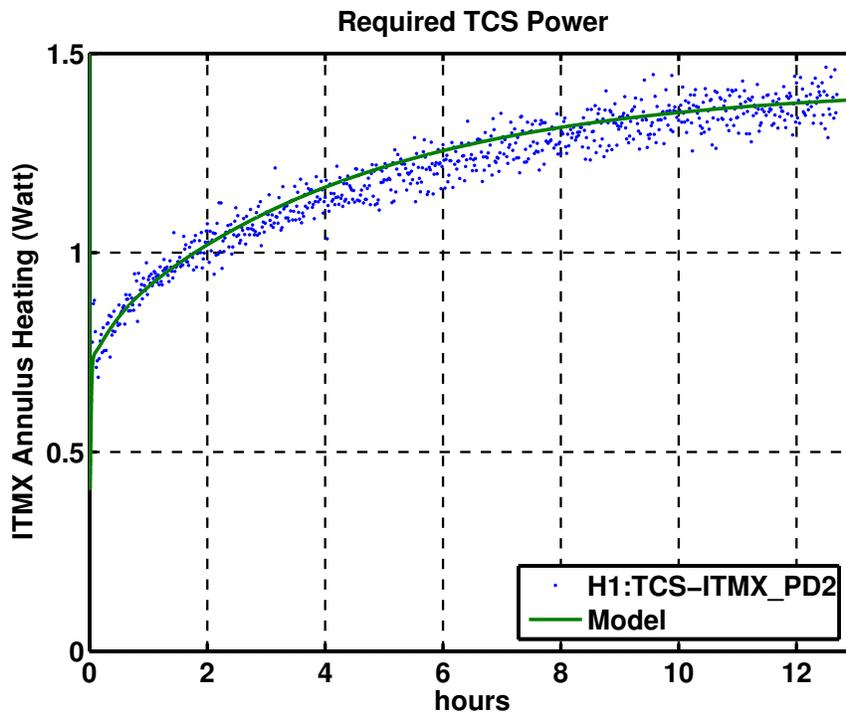
Figure 2-11:   **Annulus compensation power** required to keep the thermal lens constant. The solid green line is calculated as described in the text. The blue dots are photo diode read-backs of the applied compensation power over a 12 hour lock, during which the servo system kept the interferometer at the optimal operations point.

2.8.4 Servo system

As mentioned a TCS servo system was key to keeping the interferometer at the right operation point when the annulus heating mode was used. The critical part was getting a usable error signal for the common heating. Since common heating strongly affects the sideband mode size in the recycling cavity, and therefore the overlap between carrier and sideband in the recycling cavity, installing a radial RF mode matching wavefront sensor or bullseye detector in the interferometer BS pick-off port provided a clean error signal.

The bullseye detector was originally developed by the University of Florida and intended to improve the input beam mode matching [74]. It consists of a round central quadrature with a diameter of 2 mm and 3 outer quadratures with the same sensitive area placed in a tight circle around the central quadrature. The diode was tuned for the resonant sideband frequency (24.48 MHz) and an RF notch at 49.96 MHz was added. Since the bullseye mode $\Psi \propto (1 - 2\ r^2/w^2) \exp(-r^2/w^2)$ has a node at $r = w/\sqrt{2}$, and since the gap between inner and outer quadrants is at $r = 1$ mm, the beam radius on the bullseye detector has to be $w = 1.41$ mm. Furthermore in order to be sensitive to the wavefront curvature difference between carrier and sideband in the recycling cavity it has to be placed at the same Gouy phase as the recycling cavity. Both of these requirements can easily be fulfilled sufficiently by one focusing lens and placing the bullseye detector *before* the focus where the beam radius is $w = 1.41$ mm.

On H1, experimentally it was immediately clear that the AS_I signal was sensitive to the differential TCS heating. AS_I is known to be sensitive to a lot of different alignment parameters too (see section 2.4), but a non-zero AS_I signal hurts only because of the danger of RF saturation in the RF electronics. Therefore, servoing AS_I to zero by actuating the TCS systems differentially was the right thing to do - especially since this also reduced the Oscillator Phase noise coupling (see 2.8.6 and 2.5).

Once the error signals were available the servo loop was easy to close (Figure 2-13). The servo code was first implemented as Unix stand-alone with a sampling
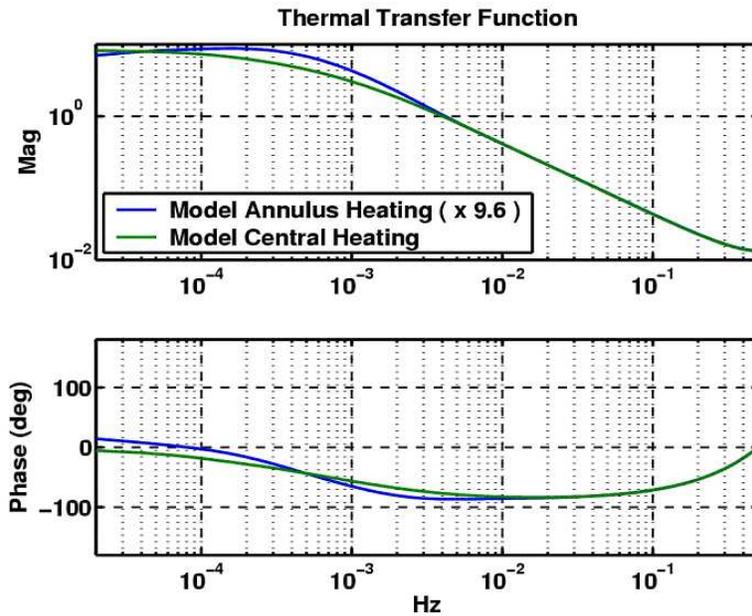
Figure 2-12: **Transfer function "actuation power to thermal lens power"** for the TCS system in both annulus and central heating mode. Both functions have been scaled to unity gain at 4 mHz, about the unity gain frequency of the servo loop. Central heating is 9.6 times more efficient, but the smaller central mask also blocks 3.9 times more power, leaving a factor 2.5 higher actuation range for the central mode. The functions were calculated as Fourier transforms of the numerically calculated impulse responses. The Nyquist frequency was 0.5 Hz, which is why both magnitude and phase show an unphysical behavior above 0.1 Hz.

frequency of 1 Hz and was later replaced by Epics code running at 5 Hz sampling rate, even though the effective update rate of the rotational stage is not that fast. The actuation function is given by Figure 2-12. Aiming for a simple $1/f$ open loop shape the control filters were simple integrators (pole at $f = 0$ Hz) with a thermal pole compensation zero at $f = 1/(10 \text{ min})$. The common servo loop was generally run with a unity gain frequency of about $1/(5 \text{ min})$, the differential servo loop at about 3 times lower gain.
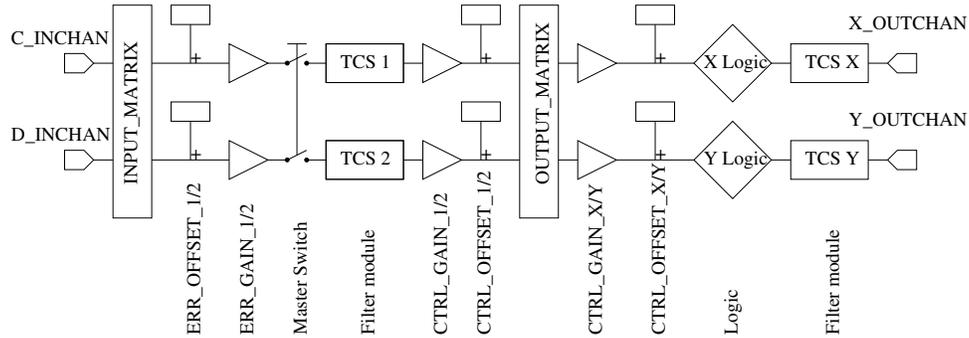
Figure 2-13: **Flow chart of the TCS servo system.** The common error signal (C_INCHAN) is the bullseye error signal. The differential error signal (D_INCHAN) is AS_I. X/Y_OUTCHAN are connected to the rotation stages that control the TCS power. The diamonds labeled with X/Y Logic contained code that automatically switched from annulus to central mode and adjusted the gain when a negative control signal was applied. However they were never used because a mask flip produces an intensity transient that is visible as a glitch in the displacement signal.

2.8.5   Noise couplings

The TCS system can convert intensity noise on the CO_2 laser into displacement noise. There are 2 mechanisms. Radiation pressure (Equation 2.33) is conceptually simpler, but not dominant at the sweet spot around $f = 150$Hz.

$$\langle \triangle z \rangle = \frac{P/c}{m_{\text{LOS}}(2\pi f)^2}\text{RIN} = 3.6 \times 10^{-19} \text{ m} \left(\frac{150 \text{ Hz}}{f}\right)^2 \left(\frac{P}{1 \text{ mWatt}}\right) \text{RIN} \quad (2.33)$$

RIN is the relative intensity noise on the CO_2 laser, P its DC power hitting the optic, c the speed of light and m_{LOS} the mass of the optic.

The dominant coupling is due to the same effect as the thermal lensing: expansion of the optic and change of the index of refraction n induced by temperature fluctuations. There are three somewhat distinct mechanisms that do contribute:

- **Expansion of the optic:** This mostly changes the cavity length. The change of the optical path length outside the cavity is small for this effect.

- **Change of index of refraction:** This changes the optical path length of the light outside the cavity.

- **Bending of the whole optic:** This effect was first pointed out to me by Phil Willems [57] after I tried in vain to understand the magnitude of the annulus transfer function. The deposited heat effectively curls the optic like a bimetallic strip. The center of mass does not move so the the area read out by the arm cavity beam will move even if there is no overlap with the heating beam. Therefore, this naturally becomes the dominant term for annulus heating. The effect does not exist for an infinitely large optic.

Expansion of the optic

From equation 2.29 one can see that the penetration depth d of fluctuations at frequency f is given by

$$d = \sqrt{\frac{\kappa}{2\pi f C \rho}} = 30\mu\text{m} \left(\frac{150 \text{ Hz}}{f}\right)^{\frac{1}{2}} \tag{2.34}$$

which is smaller than the scale on which the heating pattern $p(x, y)$ changes. Therefore the heat flow is essentially one-dimensional along the optical axis. The energy density in this surface layer is given by $E(x, y) = C\rho \int dz T$. Since $\dot{E}(x, y) = p(x, y)$ we have

$$p(x, y) = 2\pi i f C \rho \int dz T \tag{2.35}$$

The temperature fluctuations in this surface layer have 2 effects. The surface layer expands by

$$\triangle z_1 = (1 + \eta)\alpha \int dz T. \tag{2.36}$$

The factor $(1 + \eta)$ arises because only the surface layer is heated, i.e. no lateral expansion is permitted. This induces a lateral stress $\sigma_T = E_S \alpha T$ which in turn produces an additional expansion of $\epsilon_{||} = \eta \sigma_T / E_S$ along the optical axis. η is the Poisson ratio and E_S is the Young's modulus. Since only a thin layer with a mass much smaller than the rest of the optic is expanding all of the expansion $\triangle z_1$ goes into changing the arm cavity length.

Change of index of refraction

Additionally the optical thickness of the ITM is increased by

$$\triangle z_2 = \left[(n-1)(1+\eta)\alpha + \frac{dn}{dT}\right] \int dz T. \tag{2.37}$$

$\triangle z_2$ is bigger than $\triangle z_1$, but its effect is down by $r'_c = \frac{\pi}{2\mathcal{F}}$ because it only affects the light outside the arm cavity. $\mathcal{F}$ is the finesse of the arm cavity. Also the effect has the opposite sign compared the the expansion effect.

Putting together equations 2.35, 2.36 and 2.37 we get for the displacement induced by the heated surface layer

$$\triangle z(x,y) = \left[(1+\eta)\alpha\left(1 - \frac{\pi}{2\mathcal{F}}(n-1)\right) - \frac{\pi}{2\mathcal{F}}\frac{dn}{dT}\right] \frac{1}{2\pi i f C\rho} p(x,y) \tag{2.38}$$

Finally, to get the average displacement seen by the interferometer one has to average $\triangle z(x,y)$ over the main laser beam. Since the readout photo diode ultimately detects power the beam intensity is the right weighting factor, i.e.

$$\langle \triangle z \rangle = \frac{\int dx dy I(x,y) \triangle z(x,y)}{\int dx dy I(x,y)} \tag{2.39}$$

with $I(x,y) = 2/(\pi w^2)\exp(-2(x^2 + y^2)/w^2)$ the main laser beam profile with beam

radius $w = 4$ cm. In central heating mode the CO_2 laser heating pattern $p(x, y)$ has the same profile as the main laser and we get $\langle p \rangle = P/(\pi w^2)$, where $P = \int dx dy\, p(x, y)$ is the total heating power. In annulus mode there is an additional factor of about $1/30$ due to the reduced overlap of $p(x, y)$ and $I(x, y)$, which is more than observed experimentally, see figure 2-14.

Bending of the optic

A bimetallic strip with extreme thickness ratio $d \ll h$ and dimensions $(h + d) \ll$ *width* $\ll$ *length* will bend along its largest dimension with a radius of curvature R given by (see for instance [76, 57])

$$\frac{1}{R} = \frac{6d\Delta\epsilon}{h^2} \tag{2.40}$$

with $\Delta\epsilon$ being the misfit strain. In fact, for a small, unconstrained patch with *width* $\ll R$ and *length* $\ll R$ the same results holds for both the length and the width dimension. Corrections due to geometric constraints will only arise when the surface area is not heated uniformly (e.g. heat only in the center).

Nevertheless I will first naively apply this result to our case of an optic with a thin heated surface layer and worry about corrections afterward:

$$\frac{1}{R(r)} = \frac{6\alpha}{h^2} \int dz\, T(z, r) \tag{2.41}$$

Based on that we can estimate the displacement profile of the front surface as

$$z(r) = \left[\int_0^r dr \int_0^r dr \frac{1}{R(r)} \right] - \left[\frac{2}{R_{\text{optic}}^2} \int_0^{R_{\text{optic}}} dr\, r \int_0^r dr \int_0^r dr \frac{1}{R(r)} \right] \tag{2.42}$$

where the second term guarantees that the center of mass does not move. Again one has to average over the readout beam. I do this numerically an get

$$\langle \triangle z_3 \rangle = \frac{6\alpha}{h^2} \frac{P}{2\pi f C \rho} \times C_{\text{num}}(\text{beam shape}, R_{\text{optic}}). \tag{2.43}$$

For an annulus heating beam (illumination beam radius $w_{\text{illum}} = 11$ cm, inner mask radius $r_{\text{inner}} = 4$ cm) the numerical factor is $C_{\text{num}}^{\text{ann}} \approx 0.055$.

As mentioned this calculation is only correct for a strip that has no additional geometric constraint, i.e. there is a correction if we want to bend a plate into a sphere element. However in annulus mode heat is only deposited at the edge and the correction should be small. In appendix D I estimate that the correction to equation 2.43 for central heating is

$$\frac{1}{1 + \pi \ln \frac{r_2}{r_1}},\tag{2.44}$$

with $r_2 = R_{\text{optic}}$ the radius of the optic and $r_1 = w$ the radius of the heating beam. Including that correction the numerical factor for central heating is $C_{\text{num}}^{\text{cen}} \approx 0.12$. In both cases the sign of this effect is the same as for the expansion effect.

Total thermo-optical effect

For the magnitude of the thermo-optical intensity noise coupling in central heating mode we therefore get

$$
\begin{aligned}
\langle \triangle z \rangle &= \frac{P}{2\pi f C \rho} \left(\frac{1}{\pi w^2} \left[(1+\eta)\alpha \left(1 - \frac{\pi}{2\mathcal{F}}(n-1) \right) - \frac{\pi}{2\mathcal{F}} \frac{dn}{dT} \right] + \frac{6\alpha}{h^2} C_{\text{num}}^{\text{cen}} \right) \text{RIN} \\
&= 9.8 \times 10^{-17} \text{ m} \left(\frac{150 \text{ Hz}}{f} \right) \left(\frac{P}{1 \text{ mWatt}} \right) \text{RIN}.
\end{aligned}
$$

$$\tag{2.45}$$

Here $w = 4$ cm is the beam radius and $h = 10$ cm is the optic thickness. The thermo-optical effect thus dominates over the radiation pressure effect everywhere above 0.6 Hz. For the annulus mode the calculated number is

$$\langle \triangle z \rangle = 1.4 \times 10^{-17} \text{ m} \left(\frac{150 \text{ Hz}}{f} \right) \left(\frac{P}{1 \text{ mWatt}} \right) \text{RIN}.\tag{2.46}$$

It is dominated by the bending term.

To verify this prediction the heating beam was modulated with an acoustooptic modulator and the transfer function to displacement was measured with the locked
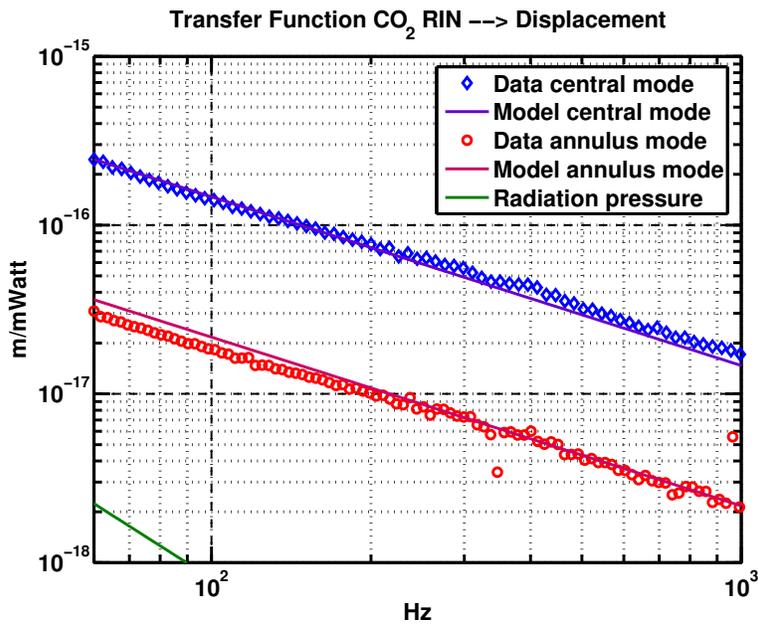
Figure 2-14: **TCS noise coupling** Comparison of modeled and measured "CO_2 intensity noise to displacement" coupling. Blue diamonds show data taken in central mode, red circles show data taken in annulus mode. The solid lines correspond to the model, no fitting was done. The model includes all three mechanisms of thermo-optical coupling. Also shown is the (small) coupling due to radiation pressure.

interferometer. The result is shown in figure 2-14. The transfer functions in both central mode and annulus agree with the model - almost too well for the approximations made.

Finally the relative intensity noise (RIN) of the installed 10 Watt CO_2 laser system was measured (Figure 2-15). Initially the RIN had several bad peaks that turned out to arise from reflections from the masks and the polarizer on the rotation stage back into the laser. Designing a solid mount for the rotation stage and carefully dumping all reflections fixed this problem. The RIN of the current system is around 2×10^{-6} in the critical 100 Hz - 500 Hz band, but only 1×10^{-5} at 2 kHz. With an active
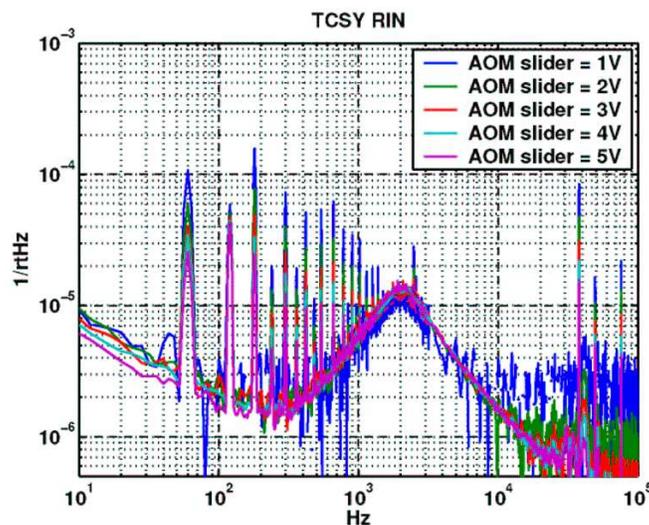
Figure 2-15: **Relative Intensity Noise** of the CO_2 lasers used in the TCS system. The measurement was repeated at different power levels (AOM voltage settings). Data points that vary systematically between the 5 traces are sensing noise limited (e.g. 60 Hz and harmonics, data above 20 kHz and below 60 Hz). The peak at 2 kHz however is real but fortunately outside the band around 150 Hz where we are most sensitive. Between 100 Hz and 500 Hz we have a RIN of about 2×10^{-6}.

intensity stabilization servo for the CO_2 lasers it should be possible to get the RIN as low as 5×10^{-7} at all relevant frequencies, but so far this was not necessary.

Combining the RIN measurement and the measured transfer function we can estimate the contribution of the TCS intensity noise to the L_- displacement noise. For the S5 configuration this is shown in figure 2-16 (black dashed line). It was

estimated assuming 30 mWatt of heating power per ITM (the actual value can vary because the required heat changes during a lock). The noise level is now about 30 times below the design sensitivity. During S4 (i.e. before the ITMX was replaced) however the noise contribution was about 6 times higher since we needed about 50 times more power but only won a factor of 8 due to the lower noise coupling in annulus mode.

2.8.6   Oscillator Phase noise reduction

The coupling mechanism of oscillator phase noise depends on the amount of both carrier and sideband light in the bullseye mode ($l = 2$). Indeed we noticed that applying heat differentially to the ITMs (e.g. annulus mode on ITMX and central mode on ITMY) affects the phase noise coupling. We were able to reduce the coupling by about a factor of 4 using this tuning.

After we replaced ITMX with a lower absorption optic the the coupling was at this lower level even without differential TCS tuning, so during S5 no differential control loop was running.

2.8.7   Optics replacement after S4

Since we wanted to further increase the circulating power after the fourth science run (S4), it was ultimately decided to open the vacuum system and replace the high absorption ITMX (see section 2.7.1) with a spare optic. During the same vent ITMY, which also showed an elevated absorption level, was wiped. This incursion proved to be quite successful - afterward the measured absorption levels were consistent with the specifications for both ITMs. As a consequence we then had to run with the TCS system in central mode.
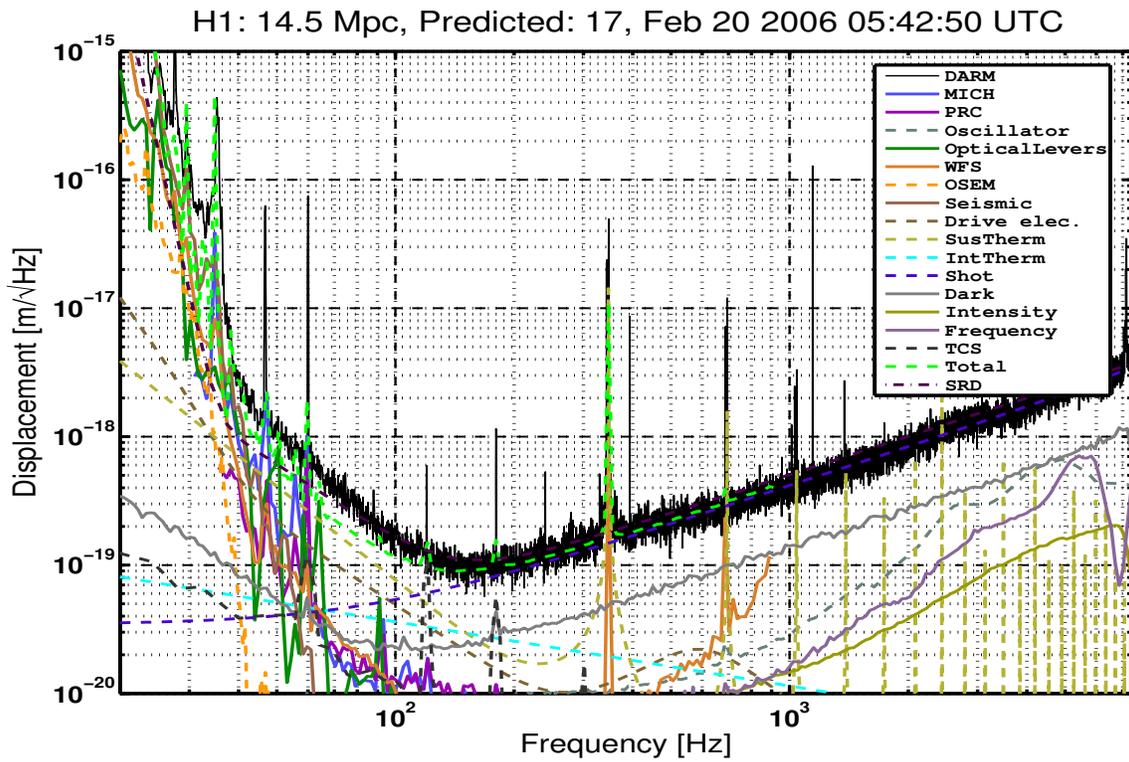
Figure 2-16: **H1 Noise Budget:** The displacement spectrum is shown in solid black. The incoherent sum of all noise sources is dashed green. The inspiral range for this displacement spectrum is 14.5 Mpc. See text for more information.
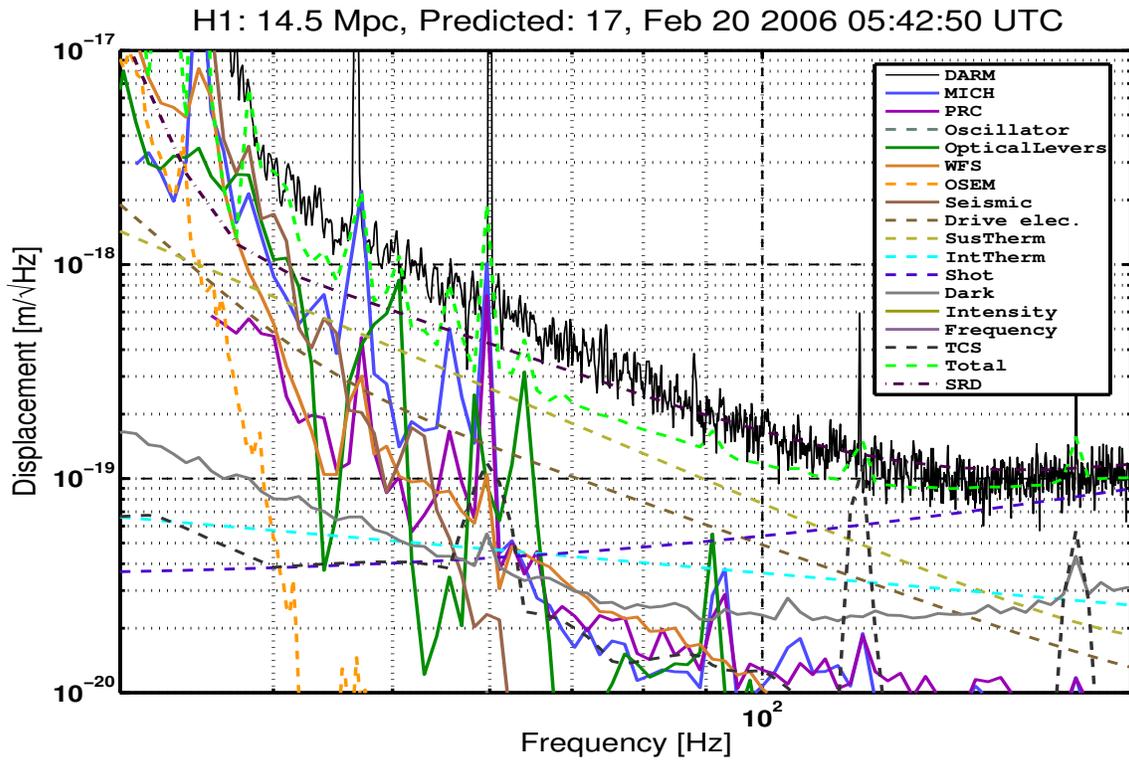
Figure 2-17: **H1 Noise Budget (zoom):** Zoomed version of figure 2-16. The displacement spectrum is shown in solid black. The incoherent sum of all noise sources is dashed green. See text for more information.

2.9 Summary of known noise sources

Figure 2-16 shows one of the best displacement spectra from H1 (solid black) together with estimates for all known noise sources. The inspiral range - the sky-averaged distance out to which a neutron star inspiral can be seen with an SNR of at least 8 - is 14.5 Mpc. The sum of all identified noise sources predicts an inspiral range of 17 Mpc. In particular those noise sources are

- **MICH:** This cross-talk estimate is based on the MICH_CTRL channel and the transfer function to displacement includes an estimate for the MICH correction efficiency, see section 2.7.2. Without that correction the MICH noise would be about 37dB higher and dominate the displacement sensitivity.

- **PRC:** This cross-talk estimate is based on the PRC_CTRL channel and the transfer function to displacement includes an estimate for the PRC correction efficiency, see section 2.7.2.

- **Oscillator Phase Noise:** The estimate is based on the phase noise specification of the Wenzel crystal oscillator and the measured transfer function to displacement, see section 2.5.

- **Optical Levers:** Noise due to angle to length cross-talk from the angular drive of the optical levers, see also [51], section 4.1.5.

- **Wave Front Sensors (WFS):** Noise due to angle to length cross-talk from the angular drive of the wave front sensing system, see also [51], section 4.1.5.

- **OSEM:** Noise due to local damping loops.

- **Seismic:** Seismic ground motion propagated through a model of the seismic isolation stack and the optics suspension. See [58, 51].

- **Drive electronics:** Combined noise of the ETM, ITM and BS drive electronics. See [51], section 4.1.4 and [56] for updates to the coil driver.

- **Suspension Thermal Noise:** Thermal noise of the single steel wire loop suspension. It has been analyzed in detail in [63]. The shown trace is for a wire loss angle of $\phi = 1.0 \times 10^{-3}$. Recent measurements by S. Penn and G. Harry at MIT suggest that the intrinsic wire loss angle of the steel wire is as low as $\phi = 1.7 \times 10^{-4}$. However in situ violin mode Q measurements suggest an effective loss angle closer to $\phi = 3 \times 10^{-3}$, with the worst inferred loss angle being $\phi = 5.6 \times 10^{-3}$. The clamping of the wire to the suspension cage is suspected to be responsible for this discrepancy. In the region around 100 Hz the suspension thermal noise scales as $\phi^{\frac{1}{2}}$.

- **Internal Thermal Noise:** Thermal motion of the test mass itself. There is still some uncertainty in the knowledge of the coating loss angle. The shown trace is for a coating loss angle of 2×10^{-4}. For more details see [62]. Other relevant references: [59, 60, 61, 51].

- **Shot Noise:** Photon shot noise at the AS port. The trace was calculated using the measured DC photo current. See also section 2.3. Note that the input power was recently increased by about 30%.

- **Dark Noise:** Sensing noise when no light is present at the AS port. Above roughly 60 Hz this is due to AS_I servo drive noise, which dominates the thermal noise in the photo diode tank circuit. Below that it is ADC noise.

- **Intensity Noise:** This estimate is based on a RIN measurement and a RIN to displacement transfer function measurement. For more details see [51], section 4.2.1.

- **Frequency Noise:** Also based on an out-of-loop REFL_I sensing noise (shot noise) measurement and a REFL_I to displacement transfer function measurement. For more details see [51], section 4.2.2.

- **TCS:** Thermal Compensation System intensity noise coupling, see section 2.8.5.

- **Total:** Incoherent (RMS) sum of all known noise sources. It explains the displacement noise everywhere except in the 60 Hz to 100 Hz band. This is also the band that shows dependence on seismic activity below 10 Hz. At this point it looks like up-conversion in the drive electronics could be responsible for this.

- **SRD:** This is the design sensitivity curve from the Science Requirement Document [39].

2.10   Limitations of the existing hardware

At the time of writing all three LIGO interferometers have reached or surpassed their design sensitivity. However, while this is a key milestone for the LIGO project, the current interferometers still have a potential for improvements.

From figures 2-16 and 2-17 it is clear that the interferometers are limited by shot noise everywhere above (and including) the sweet spot at 150Hz. Therefore the interferometer sensitivity can be improved by increasing the circulating power further. To be able to do that however, an upgraded laser is required. The currently installed lasers from Lightwave with a nominal output power of 10 Watts are getting close to the end of their lives, and the available laser power is maxed out on both the H1 and L1 interferometer.

Based on the experience with the installed thermal compensation system (section 2.8) and the optics absorption levels after the ITMX replacement, it seems plausible that the interferometers can run with at least 5 times more input power without suffering too much from thermal aberrations. However, the sensing photo diodes and electronics are already running out of headroom at the current power level, mostly due to a too big AS_I signal (section 2.4). Thus one would have to scale the number of photo diodes at the dark port from currently four to on the order of twenty, which just is very impractical.

A more attractive way around this problem is to install and commission an output mode cleaner [50]. It can remove all the junk light that is responsible for the AS_I signal before it hits the photo diode. But because an output mode cleaner introduces

a sensitivity to beam jitter, it has to be installed seismically isolated and in-vacuum. Tentative plans to both upgrade the laser and install an in-vacuum output mode cleaner after the one year long S5 science run are in place [50].

Chapter 3

Searching for an anisotropic background of gravitational waves

The LIGO Scientific Collaboration has analyzed the data from the first three science runs for an isotropic stochastic background of gravitational waves [90, 91].

It is possible though that the dominant source of stochastic gravitational waves in the LIGO frequency band comes from an ensemble of astrophysical sources (e.g. [95, 9]). If such an ensemble turns out to be dominated by its strongest members then the assumption of isotropy is no longer valid. Instead one should look for anisotropies in the stochastic gravitational wave background. In this chapter I introduce an analysis that, based on the cross-correlation of the data streams from two spatially separated gravitational wave interferometers, allows to resolve such anisotropies.

Any search for stochastic gravitational waves by definition assumes two things about the targeted source(s):

- *The duty cycle η is significant* (≈ 1), i.e. it is not a transient source. This is a key assumption since the signature of transient sources is overwhelmed by the integration over the whole run.

- *The wave form is unknown.* This is not a requirement - after all we are free to ignore that knowledge. But if the wave form is known, a matched template search (e.g. the LIGO Pulsar search [87, 88]) would be more sensitive.

Of course one still has to know, or assume, the frequency content of the signal. This information is specified by the signal strain power spectrum $H(f)$ (see appendix C.1 for a definition). Under the assumption that this signal strain power spectrum $H(f)$ is known, the analysis presented in the chapter is optimal.

First though I will introduce the properties of a stochastic background of gravitational waves and discuss the existing indirect and direct experimental limits on such a background.

3.1   Cosmological source

A cosmological stochastic background of gravitational waves is in many ways similar to the Cosmic Microwave Background from the early universe (CMB, [5, 6]), which is a background of electromagnetic waves. As with the CMB it is useful to characterize the gravitational background by normalizing the energy density ρ_{gw} per logarithmic frequency f by the energy density required to close the universe, ρ_c.

$$\Omega_{\mathrm{gw}}(f) = \frac{1}{\rho_c} \frac{d\rho_{\mathrm{gw}}}{d\ln f} \tag{3.1}$$

The critical energy density ρ_c follows from the Friedman equation and is

$$\rho_c = \frac{3c^2 H_0^2}{8\pi G} \approx 1.7 \times 10^{-8} h^2 \frac{\mathrm{ergs}}{\mathrm{cm}^3}. \tag{3.2}$$

Here $H_0 = h \times 100 \ \mathrm{km \ sec^{-1} Mpc^{-1}}$ is the Hubble constant (today). $\Omega_{\mathrm{gw}}(f)$ is related to the strain power spectrum $S_{gw}(f)$ visible to an interferometer through

$$\Omega_{\mathrm{gw}}(f) = \frac{10\pi^2}{3H_0^2} f^3 S_{\mathrm{gw}}(f) \tag{3.3}$$

See appendix C for a derivation.

The main difference relative to the CMB is that a gravitational wave background decouples much earlier in the history of the universe. Depending on the model this could happen during the inflationary epoch, i.e. around the grand unification scale

(10^{16} GeV) or during the Planck era ($\sqrt{c^5 \hbar G^{-1}} \approx 10^{19}$ GeV), when Quantum Gravity still was important. The predictions on the spectral shape and amplitude of $\Omega_{\text{gw}}(f)$ also vary a lot depending on the model. A good summary is given in [94].

3.1.1 Existing bounds on $h^2 \Omega_{\text{gw}}(f)$

Nucleosynthesis: The successful prediction of the cosmic abundances of the lightest elements (^{3}He, ^{4}He and ^{7}Li) by the Big Bang Nucleosynthesis can be used to set a constrain on the gravitational wave energy density during Nucleosynthesis [94].

This can be understood as follows: Just before the neutrino freeze-out at a temperature $T_F \approx 1.2 \times 10^{10}$K or about 1 MeV the neutron to proton ratio is given by $n_n/n_p = \exp(-Q/T_F)$, where $Q = m_n - m_p = 1.3$MeV. After the neutrinos freeze out some of the remaining neutrons decay, but most of them end up in ^{4}He. Hence the ^{4}He abundance is exponentially sensitive to the neutrino freeze-out temperature T_F.

The neutrino freeze-out temperature T_F on the other hand is defined by the reaction rate $\Gamma_{pe \to n\nu}$ being equal to the Hubble expansion rate $H = \sqrt{8\pi G\rho/3}$. The reaction rate is roughly $\Gamma_{pe \to n\nu} \approx G_F^2 T^5$ (really only appropriate for $T > Q$). $G_F = 1.1664 \times 10^{-5}$GeV^{-2} is the Fermi coupling constant describing the weak interaction. The total energy density ρ during this period can be expressed as

$$\rho = \frac{\pi^2}{30} \frac{k_B^4}{\hbar^3 c^3} g_* T^4 = \frac{g_*}{2} a T^4. \tag{3.4}$$

Here $a = 7.57 \times 10^{-15}$ erg cm^{-3} K^{-4} is the radiation constant and g_* is the effective number of species (i.e. relativistic particles) during the epoch of Nucleosynthesis. This shows that $T_F \propto g_*^{\frac{1}{6}}$, i.e. the ^{4}He abundance is sensitive to the effective number of species during Nucleosynthesis.

The number of species g_* is defined through

$$g_* = \sum_{i=\text{bosons}} g_i \left(\frac{T_i}{T}\right)^4 + \frac{7}{8} \sum_{i=\text{fermions}} g_i \left(\frac{T_i}{T}\right)^4, \tag{3.5}$$

where g_i counts the internal degrees of freedom of the i-th particle (spin, color,...) and T_i is its temperature. For gravitons we have $\rho_{gw} = aT_{gw}^4$, defining the partial temperature T_{gw}, even though they are not in thermal equilibrium. The photons are in thermal equilibrium, $T_\gamma = T$, and we have $\rho_\gamma = aT^4$. Thus the contribution from gravitational waves to the number of species g_* is given by

$$\Delta g_* = 2\frac{\rho_{gw}}{\rho_\gamma} \tag{3.6}$$

Also note that often limits on Δg_* are given as number of extra neutrinos ΔN_ν. The conversion is $\Delta g_* = 7/4\Delta N_\nu$.

The measured abundance of ^{4}He restricts $\rho_{\rm gw}$ to be at most of the same magnitude as the photon energy density ρ_γ during the epoch of Nucleosynthesis [94]. Both $\rho_{\rm gw}$ and ρ_γ scale as $T^4 \propto (1+z)^4$, but the later annihilation of electron-positron pairs increases the photon energy density ρ_γ by a factor $(11/4)^{4/3} \approx 3.8$. Finally, the transition from a radiation to a matter dominated universe happened at $z \approx 4\times10^4 h^2$, resulting in

$$h^2\Omega_\gamma = h^2\frac{\rho_\gamma}{\rho_c} \approx 2.5 \times 10^{-5} \tag{3.7}$$

and therefore an upper limit for the gravitational wave energy density $\Omega_{\rm gw}$ of

$$h^2 \int d(\ln f)\Omega_{\rm gw}(f) = h^2\Omega_{\rm gw} = h^2\frac{\rho_{\rm gw}}{\rho_c} \lesssim 6 \times 10^{-6}. \tag{3.8}$$

This limit spans all frequencies, but it only applies to gravitational waves that were already present during Nucleosynthesis at $z \approx 10^9$.

CMB: The measurement of the large angle fluctuations in the CMB by COBE [5] and WMAP [6] can be used to derive an upper limit for frequencies that are inside the horizon today ($f > 3 \times 10^{-18}$ Hz), but were still outside the horizon during the time of last scattering ($f < 10^{-16}$ Hz)[94, 5]:

$$h^2\Omega_{\rm gw}(f) \lesssim 10^{-13} \left(\frac{10^{-16}\text{ Hz}}{f}\right)^2, \quad 3 \times 10^{-18}\text{ Hz} < f < 10^{-16}\text{ Hz}. \tag{3.9}$$

Radio Pulsar Timing: Radio Pulsars are extremely precise clocks - for some of them the spin frequency is know with a relative precision of a couple $\times 10^{-16}$. They can thus be used to measure time of flight variations due to gravitational waves crossing the line of sight. The longest accessible wavelength is determined by the distance to the pulsar and the sensitivity to shorter wavelength drops rapidly since the signal is averaged out over many wavelengths [86].

$$h^2\Omega_{\mathrm{gw}}(f) \lesssim 4.8 \times 10^{-9} \left(\frac{f}{f_*}\right)^2, \quad f > f_* = 4.4 \times 10^{-9} \text{ Hz.} \tag{3.10}$$

Spacecraft Doppler Tracking: This is analogous to the radio pulsar timing. The upper limit based on measurements with the Cassini Spacecraft [85] is

$$h^2\Omega_{\mathrm{gw}}(f) \lesssim 0.025, \quad \text{at } f \approx 1.2 \times 10^{-6} \text{ Hz.} \tag{3.11}$$

Direct measurement: The frequency band above roughly 10 Hz is accessible to terrestrial experiments. The first experimental upper limits came from resonant bar detectors for a narrow band around 1 kHz. They were first operating on their own and later in pairs, allowing for a correlation analysis [79, 80, 81, 82, 83]. The first upper limit using an interferometer was published in 1994 [84]. In 2005 the LIGO collaboration published its best upper limit so far, achieving $h^2\Omega_{\mathrm{gw}}(f) \lesssim 4.4 \times 10^{-4}$ [91]. Table 3.1 lists the published upper limits that were achieved.

3.2 Astrophysical sources

It is possible that the dominant source of stochastic gravitational waves in the LIGO frequency band comes from an ensemble of astrophysical sources (e.g. [95, 9]). In this case the Nucleosynthesis bound - the tightest existing bound in the LIGO frequency band - is not applicable. Furthermore, if such an ensemble turns out to be dominated by its strongest members then the assumption of isotropy is no longer valid. Instead one should look for anisotropies in the stochastic gravitational wave background. This was addressed in Ref. [96, 97], but they characterized the anisotropies in terms

Experimental Limits			
Experiment	Limit on $h^2\Omega_{\text{gw}}(f)$	Frequency	Reference
Room Temperature Resonant Bar (correlation)	$\lesssim 3000$	$f_0 = 985 \pm 80$ Hz	Glasgow [79]
Cryogenic Resonant Bar (single)	$\lesssim 300$ $\lesssim 5000$	$f_0 = 907$ Hz $f_0 = 1875$ Hz	Explorer [80] ALTAIR [81]
Cryogenic Resonant Bar (correlation)	$\lesssim 60$	$f_0 = 907$ Hz	Explorer + Nautilus [82, 83]
Interferometers	$\lesssim 3 \times 10^5$ $\lesssim 4.4 \times 10^{-4}$	100 Hz $\lesssim f \lesssim$ 1 kHz 69 Hz $\lesssim f \lesssim$ 156 Hz	Garching-Glasgow [84] LIGO S3 Run [91]

Table 3.1: **Published direct upper limits on $\Omega_{\text{gw}}(f)$ achieved by terrestrial detectors**

of spherical harmonics, and focused on getting optimal estimates for each spherical harmonic. If the stochastic gravitational wave background is indeed dominated by individual sources one can get a better signal-to-noise ratio by obtaining optimal filters for small patches of the sky (see section 3.3). This is the motivation for the radiometer analysis.

While the real strength of the radiometer analysis is its sensitivity to sources with an unknown wave form it is still useful to see how good it can do for known sources. As mentioned at the beginning of this chapter, the key requirement for the radiometer analysis to be applicable is that the targeted source has a significant duty cycle. This excludes individual collisions of compact objects and stellar explosions. The only known astrophysical sources that fulfill this criterion are rotating neutron stars (pulsars).

Of particular interest are accreting neutron stars, for two reasons:

- The power radiated in gravitational waves is proportional to the sixth power of the spin frequency, and the fastest spinning known pulsars were all spun up by accreting matter.

- In order to radiate gravitational waves the pulsar has to have a non-vanishing

quadrupole momentum and matter falling on to the surface seems to be a natural mechanism to produce such a deviation from spherical symmetry.

Binary star systems with ongoing accretion on to a compact object are known as X-ray binaries. Two types are distinguished, Low-Mass X-ray Binaries (LMXB) and High Mass X-ray Binaries (HMXB). I want to focus on the Low-Mass X-ray Binaries because as far as I can tell they are the strongest predicted continuous source of gravitational waves that is known to exist.

3.2.1 Accretion driven pulsars: Low-Mass X-ray Binaries (LMXB)

Whether a neutron star in a close binary system is accreting mass depends on the ratio of the mass of the neutron star to that of the companion. Stable mass transfer in such a system only occurs when the companion fills its Roche lobe and has a smaller mass than the neutron star. Systems with such a low-mass companion are called Low-Mass X-ray Binaries (LMXBs).

Accretion in systems with a high mass companion has to be driven by the companion's stellar wind. These systems are referred to as High-Mass X-ray Binaries (HMXBs) and typically have lower accretion rates.

Accreting neutron stars with a high mass accretion rate will spin up until some mechanism can radiate away the angular momentum of the matter falling in. The two possible candidates are electromagnetic dipole radiation and gravitational quadrupole radiation [9, 10]. The radiated power P is given by

$$P_{em} = \frac{4\pi}{6c^3\mu_0}B_{\mathrm{pole}}^2 R^6 \sin^2(\theta)\omega^4 \tag{3.12}$$

for magnetic dipole radiation and

$$P_{gw} = \frac{32G}{5c^5}M^2 R^4 \epsilon^2 \omega^6 \tag{3.13}$$

for gravitational radiation. The corresponding radiational torque is $T = P/\omega$. B_{pole}

is the magnetic field at the pole, R and M the radius and mass of the neutron star, θ the angle between magnetic and rotational axis, ω the spin angular frequency and $\epsilon^2 = Q_{ij}Q_{ij}/(MR^2)^2$ with $Q_{ij} = \int d^3x\rho(x_ix_j - \delta_{ij}r^2/3)$ the quadrupole moment of the neutron star. Clearly if the accretion rate is large enough and the magnetic field weak enough gravitational radiation will eventually dominate.

There is observational evidence that the spin frequencies of LMXBs with high accretion rate ($\dot{M} \gtrsim 10^{-11} M_\odot \mathrm{yr}^{-1}$) and low magnetic fields ($B \ll 10^{11}$ G) cluster between about 300 Hz and 730Hz. No neutron star spinning faster than 730Hz has been found so far [11]. The low magnetic fields B suggest that these systems are not balanced by electromagnetic radiation and thus balancing by gravitational radiation is a possibility and would require a quadrupole moment of [9]

$$Q \approx 4.5 \times 10^{30} \text{ kg m}^2 \left(\frac{\dot{M}}{10^{-9}M_\odot \text{ yr}^{-1}}\right)^{\frac{1}{2}} \left(\frac{2\pi\,300 \text{ Hz}}{\omega}\right)^{\frac{5}{2}} \approx 10^{-7} \times I. \qquad (3.14)$$

The neutron star moment of inertia is $I \approx 10^{38}$ kg m^2.

The X-ray luminosity of a LMXB is given by the potential energy of the accreting mass $\dot{M}$

$$L_X = \dot{M}\frac{GM}{R} \qquad (3.15)$$

and exerts a torque of about

$$T = \dot{M}\sqrt{GMR}. \qquad (3.16)$$

If gravitational radiation is indeed the relevant angular momentum balancing mechanism the gravitational wave luminosity is tied to the X-ray luminosity by

$$L_{GW} = \frac{\omega}{\omega_{\text{Kepler}}}L_X \qquad (3.17)$$

where $\omega_{\text{Kepler}} = \sqrt{GM/R^3}$ and ω is the pulsar spin frequency. A typical value for $\omega/\omega_{\text{Kepler}}$ is 0.2. It turns out that the brightest X-ray source in the sky (short of the sun), Sco-X1, is actually a LMXB and thus a prime candidate as a gravitational wave source. Its magnetic field is indeed weak ($\approx 10^7 G$, [12]) but unfortunately so far

its spin frequency is not known, even though quasi periodic oscillations (QPOs) are observed in the X-ray [15]. The two observed QPOs are relatively coherent ($Q \approx 100$) and have frequencies of about 700 Hz and 1000 Hz, but their frequency increases with the accretion rate. There are speculations that the difference between the 2 frequencies might be the pulsar spin frequency, but a recent study seems to to exclude this theory [16]. Table 3.2 summarizes known relevant parameters of Sco-X1 (V818 Sco).

Sco-X1	
Parameter	Value
Right ascension	16h 19m 55.0850s
Declination	-15° 38' 24.9"s
Distance	2.8 ± 0.3 kpc
X-ray luminosity	2.3×10^{38} erg/sec
X-ray flux at earth	2.5×10^{-7} erg/sec/cm^2
Magnetic field near NS	$\approx 1 \times 10^7$ Gauss
Orbital period	68023.84 ± 0.08 sec
Orbital velocity	40 ± 5 km/sec
Eccentricity	≈ 0
Companion star mass	$\approx 0.42 M_\odot$

Table 3.2: **Parameters for Sco-X1.** (References: [13], [14], [12])

Interestingly Sco-X1 dominates the X-ray flux due to all LMXB's at the earth. To estimate this we can tie the X-ray luminosity density to the stellar mass density by $L_{X,\mathrm{Gal}}(z) \approx 10^{40} erg/s \times M_{\mathrm{Gal}}(z)/(10^{11} M_\odot)$ and estimate the stellar mass density as a function of z by $M_{\mathrm{Gal}}(z) \approx 5 \times 10^8 M_\odot \mathrm{Mpc}^{-3} \times (1+z)^{-1}$,[17]. Thus, for the standard cosmological parameters ($H_0 = 72$ km s^{-1} Mpc^{-1}, $\Omega_m = 0.3$, $\Omega_\Lambda = 0.7$), we get the x-ray flux:

$$
\begin{aligned}
F_{\mathrm{LMXB,cosm}} &\approx \int_0^\infty 4\pi r^2 \frac{\partial r}{\partial z} dz \frac{L_{X,\mathrm{Gal}}(z)}{4\pi r^2 (1+z)^2} \\
&= L_{X,\mathrm{Gal}}(0) \frac{c}{H_0} \int_0^\infty dz \frac{1}{\Omega_m (1+z)^3 + \Omega_\Lambda} \frac{1}{(1+z)^3} \\
&\approx 8 \times 10^{-9} \frac{\mathrm{erg}}{\mathrm{sec\ cm}^2}
\end{aligned} \tag{3.18}
$$

We can also estimate the flux from the Virgo cluster

$$F_{\text{LMXB,Virgo}} \approx 3000 \text{ Galaxies} \times 10^{40} \frac{\text{erg}}{\text{sec Galaxy}} \times \frac{1}{4\pi(15 \text{ Mpc})^2}$$
$$\approx 1 \times 10^{-9} \frac{\text{erg}}{\text{sec cm}^2}$$
(3.19)

Since the apparent diameter of the Virgo cluster is about 15 degree it covers about 1/230 of the whole sky. Together with the numbers from equations 3.18 and 3.19 this implies that X-ray flux due to LMXB - and therefore also the GW flux due to LMXB - is about 30 times stronger than average when looking at the Virgo cluster.

Values for the expected gravitational wave flux can be obtained through equation 3.17. The strain power spectrum $H(f)$ is connected to the gravitational wave flux through

$$F_{GW} = \int df \, F_{f,GW} = \frac{\pi}{4} \frac{c^3}{G} \int df \, f^2 H(f).$$
(3.20)

For Sco-X1 with $\omega/\omega_{\text{Kepler}} = 0.5 f_{\text{gw}}/f_{\text{Kepler}}$ and $F_X = 2.5 \times 10^{-7}$ erg/sec/cm^2 we get

$$H_{\text{Sco-X1}}(f)df = \frac{2G}{\pi c^3} \frac{1}{f_{\text{Kepler}} f} F_{X,\text{Sco-X1}} \approx 3.6 \times 10^{-52} \left(\frac{500 \text{ Hz}}{f} \right).$$
(3.21)

The main contribution to H(f) is at twice the pulsar spin frequency. The bandwidth is limited by the orbital frequency broadening of the binary star

$$df = f_{GW} \frac{v_{\text{orbital}}}{c} < 0.2 \text{ Hz}$$
(3.22)

where I used $f_{GW} < 2 \times 730$ Hz. 730 Hz is the highest spin frequency ever observed on a neutron star. If we want to choose a narrower bandwidth we will have to correct for this orbital frequency shift.

The earth's orbital motion has an effect of the same order of magnitude ($df/f \approx 1 \times 10^{-4}$, but longer period), while the earth's rotation only produces $df/f \approx 1.5 \times 10^{-6}$. These are all effects that can be corrected for in a specialized analysis looking only at Sco-X1. This is not done in the radiometer code because the code is optimized for broadband signals.

Finally the intrinsic frequency stability of the accreting pulsar can be estimated by assuming that the torque from the accreting matter is not balanced:

$$\dot{f} = \frac{T}{2\pi I} = \frac{5}{4\pi} \frac{L_X}{\sqrt{GM^3 R}} \approx 8 \times 10^{-5} \text{ Hz yr}^{-1} \tag{3.23}$$

3.3 The Radiometer

3.3.1 Introduction

In this section I present a directional method to search for an anisotropic gravitational wave background that implements a gravitational wave radiometer [93]. The algorithm has been implemented in MATLAB and was used to analyze the LIGO S4 science run. A summary of the relevant formulas can also be found in appendix C.

3.3.2 Search for an isotropic background

The data from the first three LIGO science runs was analyzed with a method described in detail in Ref. [98, 90, 91, 92]. The data streams from a pair of detectors were cross-correlated with a cross-correlation kernel Q chosen to be optimal for an assumed strain power spectrum $S_{\text{gw}}(f) = S_{\text{gw}}(|f|)$ and angular distribution $P(\hat{\Omega}) = 1$ (isotropic distribution). Specifically, with $S_1(f)$ and $S_2(f)$ representing the Fourier transforms of the strain outputs of two detectors, this cross-correlation is computed in frequency domain segment by segment as:

$$Y = \int_{-\infty}^{\infty} df \int_{-\infty}^{\infty} df' \delta_T(f - f') S_1^*(f) Q(f') S_2(f') \tag{3.24}$$

where δ_T is a finite-time approximation to the Dirac delta function. The optimal filter Q has the form:

$$Q(f) = \lambda \frac{\gamma_{\text{iso}}(f) S_{\text{gw}}}{P_1(f) P_2(f)} \tag{3.25}$$

where λ is a normalization factor, P_1 and P_2 are the strain noise power spectra of the two detectors, S_{gw} is the strain power spectrum of the stochastic background being

searched for (see ref [91, 90]) and the factor γ_{iso} takes into account the cancellation of an isotropic omni-directional signal $(P(\hat{\Omega}) = 1)$ at higher frequencies due to the detector separation. γ_{iso} is called the overlap reduction function [99] and is given by (the normalization is such that $\gamma_{\text{iso}}(f=0)=1$ for aligned and co-located detectors):

$$\gamma_{\text{iso}}(f) = \frac{5}{8\pi} \sum_A \int_{S^2} d\hat{\Omega} \; e^{i2\pi f \hat{\Omega} \cdot \frac{\vec{\Delta x}}{c}} \; F_1^A(\hat{\Omega}) F_2^A(\hat{\Omega}) \tag{3.26}$$

where $\vec{\Delta x} = \vec{x}_2 - \vec{x}_1$ is the detector separation vector, $\hat{\Omega}$ is the unit vector specifying the sky position and

$$F_i^A(\hat{\Omega}) = e_{ab}^A(\hat{\Omega}) \frac{1}{2}(\hat{X}_i^a \hat{X}_i^b - \hat{Y}_i^a \hat{Y}_i^b) \tag{3.27}$$

is the response of detector i to a zero frequency, unit amplitude, $A = +$ or $\times$ polarized gravitational wave. $e_{ab}^A(\hat{\Omega})$ is the spin-two polarization tensor for polarization A and $\hat{X}_i^a$ and $\hat{Y}_i^a$ are unit vectors pointing in the directions of the detector arms (see [98] for details).

The optimal filter Q is derived assuming that the intrinsic detector noise is Gaussian and stationary over the measurement time, uncorrelated between detectors, and uncorrelated with and much greater in power than the stochastic gravitational wave signal. Under these assumptions the expected variance, σ_Y^2, of the cross-correlation is dominated by the noise in the individual detectors, whereas the expected value of the cross-correlation Y depends on the stochastic background power spectrum:

$$\sigma_Y^2 \equiv \langle Y^2 \rangle - \langle Y \rangle^2 \approx \frac{T}{4}(Q, Q) \;, \qquad \langle Y \rangle = T\left(Q, \frac{\gamma_{\text{iso}} S_{\text{gw}}}{P_1 P_2}\right) \tag{3.28}$$

Here the scalar product $(\cdot, \cdot)$ is defined as $(A, B) = \int_{-\infty}^{\infty} A^*(f) B(f) P_1(f) P_2(f) df$ and T is the duration of the measurement.

In order to address the long-term non-stationarity of the detector noise the data set from a given interferometer pair is divided into equal-length intervals, and the cross-correlation Y and theoretical σ_Y are calculated for each interval, yielding a set $\{Y_I, \sigma_{Y_I}\}$ of such values, with I labeling the intervals. The interval length can be

chosen such that the detector noise is relatively stationary over one interval. In Ref. [91, 90] the interval length was chosen to be 60 sec. The cross-correlation values are combined to produce a final cross-correlation estimator, Y_{opt}, that maximizes the signal-to-noise ratio, and has variance σ^2_{opt}:

$$Y_{\mathrm{opt}} = \sum_I \sigma_{Y_I}^{-2} Y_I / \sigma_{\mathrm{opt}}^{-2} \ , \qquad \sigma_{\mathrm{opt}}^{-2} = \sum_I \sigma_{Y_I}^{-2} \ . \qquad (3.29)$$

In practice the intervals are typically overlapping by 50% to avoid the effective loss of half the data due to the required windowing (Hanning). Thus equation 3.29 has to be modified slightly to take the correlation of neighboring segments into account (see [101]).

Since the LIGO Hanford and Livingston sites are separated by 3000km the overlap reduction function for this pair has already dropped below 5% around each interferometer's sweet spot of 150 Hz, where the GW wavelength, 2000 km, is no longer large compared to the site separation. One unfortunate drawback of this analysis thus is the limited use it makes of the individual interferometer's most sensitive frequency region. Moreover, if the dominant gravitational wave background would be of astrophysical origin the assumption of an isotropic background is not well justified. If, for example, the signal is dominated by a few strong sources, a directed search can achieve a better signal-to-noise ratio.

3.3.3 Directional search: a gravitational wave radiometer

A natural generalization of the method described above can be achieved by finding the optimal filter for an angular power distribution $P(\hat{\Omega})$. In this case Eq. 3.28b generalizes to

$$\langle Y \rangle = T\left(Q, \frac{\int_{S^2} d\hat{\Omega} \gamma_{\hat{\Omega}} P(\hat{\Omega}) H}{P_1 P_2}\right) \qquad (3.30)$$

where $\gamma_{\hat{\Omega}}$ is now just the integrand of γ_{iso}, i.e.

$$\gamma_{\hat{\Omega}} = \frac{1}{2} \sum_A e^{i 2\pi f \hat{\Omega} \cdot \frac{\overrightarrow{\Delta x}}{c}} \ F_1^A(\hat{\Omega}) F_2^A(\hat{\Omega}) \qquad (3.31)$$

and $H(f)$ is the strain power spectrum of an unpolarized point source, summed over both polarizations (see appendix C.1). Note that $\gamma_{\hat{\Omega}}$ also becomes sidereal time dependent both through $\Delta\vec{x}$ and $F_i^A(\hat{\Omega})$.

Eq. 3.30 was used in Ref. [96] as a starting point to derive optimal filters for each spherical harmonic. However if one wants to optimize the method for well localized astrophysical sources it seems more natural to use a $P(\hat{\Omega})$ that only covers a localized patch in the sky. Furthermore, for most reasonable choices of $H(f)$, the maximal resolution of this method will be no better than several tens of square degrees, so that most astrophysical sources would not be resolved. It makes sense therefore to optimize the method for true point sources, i.e. $P(\hat{\Omega}) = \delta^2(\hat{\Omega}, \hat{\Omega}')$.

With this choice of $P(\hat{\Omega})$, the optimal filter $Q_{\hat{\Omega}'}$ for the sky direction $\hat{\Omega}'$ becomes

$$Q_{\hat{\Omega}'}(f) = \lambda \frac{\gamma_{\hat{\Omega}'}(f)H(f)}{P_1(f)P_2(f)} \tag{3.32}$$

and the expected cross-correlation $Y_{\hat{\Omega}'}$ and its expected variance $\sigma^2_{Y_{\hat{\Omega}'}}$ are

$$\sigma^2_{Y_{\hat{\Omega}'}} \equiv \langle Y^2_{\hat{\Omega}'} \rangle - \langle Y_{\hat{\Omega}'} \rangle^2 \approx \frac{T}{4}\left(Q_{\hat{\Omega}'}, Q_{\hat{\Omega}'}\right), \qquad \langle Y_{\hat{\Omega}'} \rangle = T\left(Q_{\hat{\Omega}'}, \frac{\gamma_{\hat{\Omega}'}H}{P_1 P_2}\right) \tag{3.33}$$

Integration over sidereal time

Just as in the isotropic case, the long-term non-stationarity of the detector noise can be addressed by processing the data on a segment by segment basis. However $\gamma_{\hat{\Omega}'}$ changes continuously with sidereal time. By setting $\gamma_{\hat{\Omega}'}$ to its mid-segment value one can get rid of the 1st order error, but a 2nd order error remains and is of the order

$$Y_{\text{err}}(T_{\text{seg}})/Y = \frac{T_{\text{seg}}^2}{24} \frac{\int_{-\infty}^{\infty} \frac{\partial^2 \gamma^*_{\hat{\Omega}'}}{\partial t^2} \gamma_{\hat{\Omega}'} \frac{H^2}{P_1 P_2} df}{\int_{-\infty}^{\infty} |\gamma_{\hat{\Omega}'}|^2 \frac{H^2}{P_1 P_2} df} = O\left(\left(\frac{2\pi f d}{c} \frac{T_{\text{seg}}}{1 \text{ day}}\right)^2\right) \tag{3.34}$$

with f the typical frequency and d the detector separation. For $T_{\text{seg}} = 60$ sec, $f = 2$ kHz and $d = 3000$ km this error is less than 1%.

Thus, for sufficiently short segment length, the integration over sidereal time for each $\hat{\Omega}'$ again reduces to the optimal combination of the set $\{Y_I, \sigma_{Y_I}\}_{\hat{\Omega}'}$ given by Eq.

3.29. The only difference to the isotropic $P(\hat{\Omega})=1$ case is that the optimal filter $Q_{\hat{\Omega}'}$ is different for each interval I and each sky direction $\hat{\Omega}'$.

3.3.4 Numerical aspects

To implement this method one thus has to calculate

$$Y_{\hat{\Omega}'} = \lambda T \int_{-\infty}^{\infty} df \frac{\gamma_{\hat{\Omega}'}^* H}{P_1 P_2} S1^* S2 \,, \qquad \sigma_{\hat{\Omega}'}^2 = \lambda^2 \frac{T}{4} \int_{-\infty}^{\infty} df \frac{|\gamma_{\hat{\Omega}'}|^2 H^2}{P_1 P_2} \qquad (3.35)$$

for each sky direction $\hat{\Omega}'$ and each segment I. This can be done very efficiently by realizing that $\gamma_{\hat{\Omega}}$ splits into a DC part, $1/2 \sum_A F_1^A(\hat{\Omega}) F_2^A(\hat{\Omega})$, and a phasor, $\exp(i2\pi f \hat{\Omega} \cdot \Delta\vec{x}/c)$. For both integrals the DC part can be taken out of the frequency integration, leaving all the directional information of the integrands in the phasor:

$$Y_{\hat{\Omega}'} = \lambda T \left(\frac{1}{2} \sum_A F_1^A(\hat{\Omega}') F_2^A(\hat{\Omega}') \right) \int_{-\infty}^{\infty} df \frac{H}{P_1 P_2} S1^* S2 \, e^{-i2\pi f \hat{\Omega} \cdot \Delta\vec{x}/c}$$

$$\sigma_{\hat{\Omega}'}^2 = \lambda^2 \frac{T}{4} \left| \frac{1}{2} \sum_A F_1^A(\hat{\Omega}') F_2^A(\hat{\Omega}') \right|^2 \int_{-\infty}^{\infty} df \frac{H^2}{P_1 P_2} \qquad (3.36)$$

Thus, with N the number of sky directions $\hat{\Omega}'$, the computational load per segment is reduced from $2N$ integrations to one fast Fourier transform, one integral and N readouts of the cross-correlation $Y_{\hat{\Omega}'}$ at the time shifts $\tau = \hat{\Omega}' \cdot \Delta\vec{x}/c$.

Since the fast Fourier transform of $S1^* S2 \, H/(P_1 P_2)$ is sampled at $f_{\text{sample}} = 2 f_{\text{Nyquist}}$ it is necessary to interpolate to get the cross-correlation $Y_{\hat{\Omega}'}$ at the time shift τ. However, by choosing a high enough Nyquist frequency and zero-padding the unused bandwidth this interpolation error can be kept small while the overall computational efficiency is still maintained.

3.3.5 Comparison to the isotropic case

It is interesting to look at the potential signal-to-noise ratio improvement of this directional method compared to the isotropic method if indeed all correlated signal would come from one point $\hat{\Omega}'$, i.e. $\langle S_1^* S_2 \rangle = \gamma_{\hat{\Omega}'} H$. The ratio between the two signal-to-noise ratios works out to

$$\frac{\text{SNR}_{\text{iso}}}{\text{SNR}_{\hat{\Omega}'}} = \frac{\langle Y_{\text{iso}}^{\text{opt}} \rangle / \sigma_{\text{iso}}^{\text{opt}}}{\langle Y_{\hat{\Omega}'}^{\text{opt}} \rangle / \sigma_{\hat{\Omega}'}^{\text{opt}}} = \frac{[\gamma_{\text{iso}}, \gamma_{\hat{\Omega}'}]}{\sqrt{[\gamma_{\text{iso}}, \gamma_{\text{iso}}] [\gamma_{\hat{\Omega}'}, \gamma_{\hat{\Omega}'}]}} \tag{3.37}$$

with $[A, B] = \sum_i (A_i H/(P_{1,i} P_{2,i}), B_i H/(P_{1,i} P_{2,i}))$ and i the index summing over sidereal time. This ratio is bounded between -1 and 1, i.e. the directional search not only performs better in this case but, for a point source at an unfortunate position, the isotropic search can even yield negative or zero correlation.

It is also possible to recover the isotropic result as an integral over the sky. The definitions of γ_{iso} and $\gamma_{\hat{\Omega}}$ (Eq. 3.26 and 3.31) imply (see also appendix C.4)

$$Y_{\text{iso}} \sigma_{\text{iso}}^{-2} = \frac{5}{4\pi} \int d\hat{\Omega} \; Y_{\hat{\Omega}} \sigma_{\hat{\Omega}}^{-2} \, , \qquad \sigma_{\text{iso}}^{-2} = \left(\frac{5}{4\pi}\right)^2 \int d\hat{\Omega} \int d\hat{\Omega}' \hat{\sigma}_{\hat{\Omega}, \hat{\Omega}'}^{-2} \tag{3.38}$$

The quantity $\hat{\sigma}_{\hat{\Omega}, \hat{\Omega}'}$ is a generalization of $\sigma_{\hat{\Omega}}$ and is defined by

$$\hat{\sigma}_{\hat{\Omega}, \hat{\Omega}'}^{-2} = \frac{4}{T} \int df \frac{\gamma_{\hat{\Omega}}^* \gamma_{\hat{\Omega}'} H^2}{P_1 P_2} \tag{3.39}$$

However there is a difference between this $\hat{\sigma}_{\hat{\Omega}, \hat{\Omega}'}$ and the the covariance $\sigma_{\hat{\Omega}, \hat{\Omega}'}^2 = \langle Y_{\hat{\Omega}} Y_{\hat{\Omega}'} \rangle$ of the 2 sky directions $\hat{\Omega}$ and $\hat{\Omega}'$. The two are related by $\sigma_{\hat{\Omega}, \hat{\Omega}'}^2 = \sigma_{\hat{\Omega}}^2 \sigma_{\hat{\Omega}'}^2 / \hat{\sigma}_{\hat{\Omega}, \hat{\Omega}'}^2$ (see appendix C.4).

The antenna lobe of the gravitational wave radiometer is described by

$$A(\hat{\Omega}, \hat{\Omega}') = \frac{\sigma_{\hat{\Omega}, \hat{\Omega}'}^2}{\sigma_{\hat{\Omega}', \hat{\Omega}'}^2} = \frac{\langle Y_{\hat{\Omega}} Y_{\hat{\Omega}'} \rangle}{\langle Y_{\hat{\Omega}'} Y_{\hat{\Omega}'} \rangle} = \frac{(Q_{\hat{\Omega}}, Q_{\hat{\Omega}'})}{(Q_{\hat{\Omega}'}, Q_{\hat{\Omega}'})} \tag{3.40}$$

In other words, if $Y_{\hat{\Omega}'} = \bar{Y}$, either because of a source $\hat{\Omega}'$ with strength $\bar{Y}$ or because of a random fluctuation, then the expectation value $\langle Y_{\hat{\Omega}} \rangle$ is $\langle Y_{\hat{\Omega}} \rangle = A(\hat{\Omega}, \hat{\Omega}') \bar{Y}$. Figure 3-
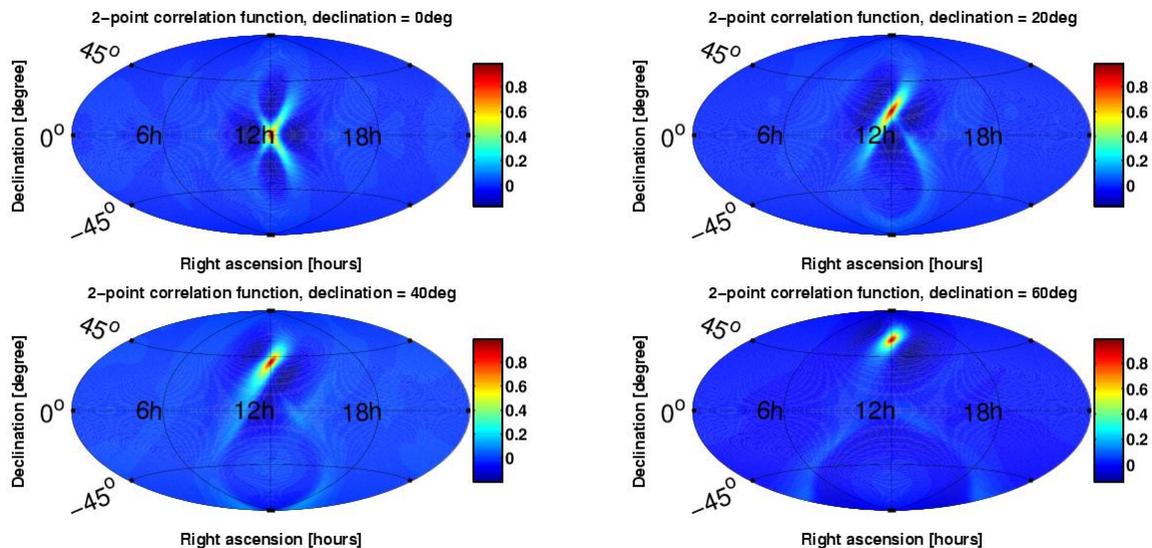
Figure 3-1: **Antenna lobe** $A(\hat{\Omega}, \hat{\Omega}')$ of the radiometer for a flat source spectrum (H = const). Plotted is the expected signal strength assuming a source at right ascension 12 h and declination 0 deg (top left), 20 deg (top right), 40 deg (bottom left) and 60 deg (bottom right). Uniform day coverage was assumed, so the resulting shapes are independent of right ascension. Typical S4 interferometer power spectra were assumed.

1 shows $A(\hat{\Omega}, \hat{\Omega}')$ for different source declinations, assuming continuous day coverage, a flat source spectrum H = const and typical S4 interferometer power spectra.

3.3.6 Achievable sensitivity

The 1-σ sensitivity of this method is given by

$$H_{\text{sens},\hat{\Omega}}(f) = \frac{\sigma_{\hat{\Omega}}}{T} H(f) = \frac{H(f)}{2\sqrt{T}\sqrt{\langle \int_{-\infty}^{\infty} \frac{|\gamma_{\hat{\Omega}}|^2 H^2}{P_1 P_2} df \rangle_{\text{sidereal day}}}} \tag{3.41}$$

H_{sens} is somewhat dependent on the declination and, in theory, independent of right ascension. In practice though an uneven coverage of the sidereal day due to down-time and time-of-day dependent sensitivity will break this symmetry, leaving only an antipodal symmetry.

For the initial LIGO Hanford 4km - Livingston 4km pair (H1-L1), both at design sensitivity, and a flat source power spectrum ($H(f)$ independent of frequency), this

91

works out to

$$H_{\text{sens}}^{H1-L1} \approx 1.5 \times 10^{-50} \text{ Hz}^{-1} \left(\frac{1 \text{ yr}}{T} \right)^{\frac{1}{2}} \tag{3.42}$$

with a 35% variation depending on the declination. This can be converted into an energy flux of

$$F_{\text{gw,f}} df = \frac{c^3 \pi f^2}{4G} H(f) df \tag{3.43}$$

Thus eq. 3.42 corresponds to a gravitational wave energy flux density of

$$F_{\text{gw,f}} df \approx 5 \times 10^{-8} \frac{\text{erg}}{\text{sec m}^2 \text{ Hz}} \cdot \left(\frac{f}{100 \text{ Hz}} \right)^2 \cdot \left(\frac{1 \text{ yr}}{T} \right)^{\frac{1}{2}} df \tag{3.44}$$

3.4 Code Validation

3.4.1 Results from simulated data

In order to test the code, the real data was blanked out and simulated Gaussian noise uncorrelated between the 2 detectors and with a power spectrum shape equal to the LIGO design sensitivity was added. To take into account the non-uniform day coverage, real lock segment start and stop times were used. To get a shorter turn-around time during testing, the code was only run on 1.7 days of integrated simulated data. The signal power spectrum was assumed to be flat, $H(f) = \text{const}$.

The algorithm was run on a 360×181 point grid covering the whole sky. While this clearly over-samples the intrinsic resolution - for the $H(f) = \text{const}$ case the antenna lobe has a FWHM area of $50 - 100 \text{ deg}^2$, depending on declination - it produces nicer pictures, as shown in Figure 3-2. For $H(f) = f^{-3}$ the antenna lobe FWHM is even about 4 times bigger.

For figure 3-3 a stochastic signal was added: coherent noise with a flat power spectrum $H(f)$ and a sidereal time dependent time shift and amplitude modulation appropriate for a true unpolarized point source.

This simulated signal was produced and calibrated piecewise in frequency domain and multiplied by a phasor $\exp(i2\pi f \tau_i)$ to encode the time shift τ_i appropriate for the source location, the current sidereal time and detector i. Both polarizations were
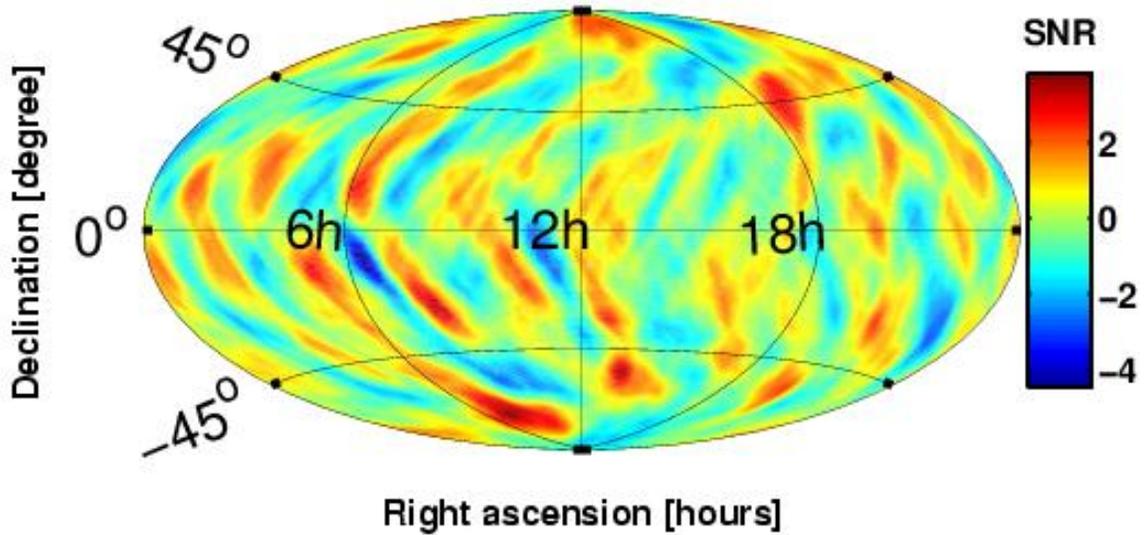
Figure 3-2: An example map of the signal-to-noise ratio SNR = $Y_{\text{opt}}/\sigma_{\text{opt}}$ for simulated Gaussian noise (see text). The visible structure - fringes with opposite tilt on the northern and southern hemisphere as required by the antipodal symmetry of the antenna lobe - is due to the antenna lobe.
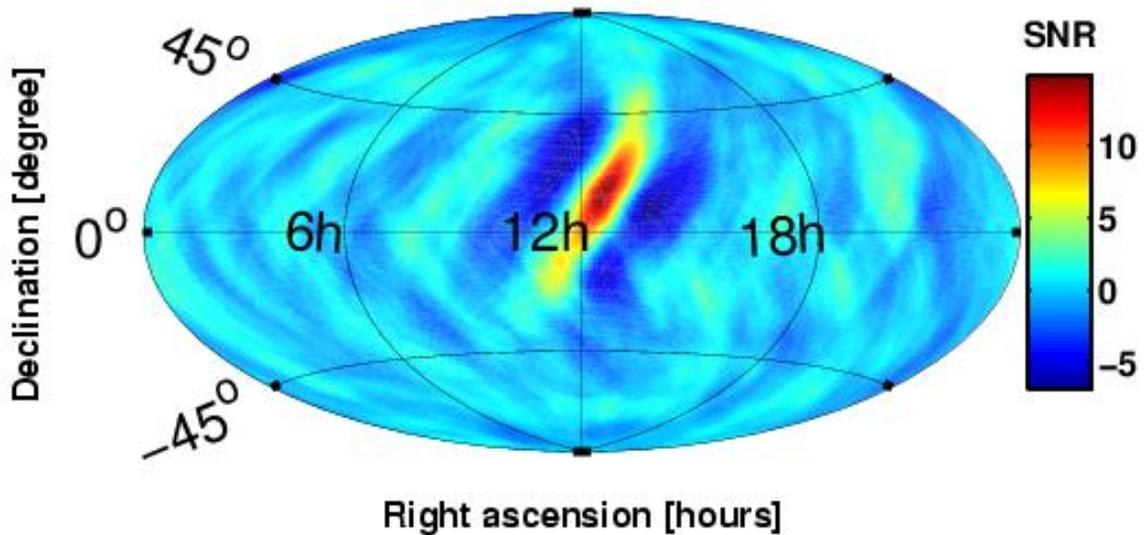
Figure 3-3: A point source with signal-to-noise ratio (SNR) of 14 was injected at the position of the Virgo galaxy cluster (12.5h, 12.7°). It is nicely recovered. This map also shows the typical structure of the antenna lobe including negative correlation in regions adjacent to the main peak.

produced independent of each other and chosen to have the same power spectral density, as required for an unpolarized source. Then, for each detector, the signal was transformed back to time domain using a fast Fourier transform and multiplied by the DC antenna acceptance $F_i^A(t)$, resulting in periodic segments of 32 second duration. These segments were then spliced together using a sin window and 50% overlap, thus preserving the power spectral density.

The injected source in figure 3-3 has a signal-to-noise ratio of 14 and is clearly recovered. This figure also shows the typical shape of the radiometer antenna lobe which is given by Eq. 3.40. In particular it shows that areas adjacent to the main lobe get a negative correlation. This means that a particularly unfortunate set of sources could in principle cancel a lot of the signal.

3.4.2 Bias factor

In [100] is was shown that using the same data for PSD estimation and cross-correlation results in a bias (underestimate) for both point estimate and standard deviation estimate. This is why the PSD is now estimated using adjacent data segments. This eliminates the bias in the point estimate, but a bias in the standard deviation estimate remains. It can be calculated by

$$\sigma_{\text{estimate}} \approx \sigma_{\text{true}} \frac{N-1}{N} \tag{3.45}$$

where N is effective number of samples used for the PSD estimate. It is given by

$$N = 2 \times \frac{9}{11} \times 29 \approx 47.5 \tag{3.46}$$

The factors are: 2 60sec segments used; 9/11 due to use of Welch's method; in each 60 sec segment there are 29, 50% overlapping, 4sec long sub-segments that are used for Welch's method.

All reported standard deviations are thus corrected (multiplied) with the factor

$$\text{bias factor} = \frac{N}{N-1} = 1.022 \tag{3.47}$$

3.4.3 Hardware injections

Hardware injections are useful because they unambiguously test the whole detection and analysis system. They are expensive though in terms of using up valuable interferometer time. For that reason no directional broadband stochastic injections were made. However both short isotropic stochastic and pulsar injections were made and can be used to verify the radiometer search code.

The isotropic stochastic injections are broadband coherent noise injections designed to mimic an isotropic primordial stochastic gravitational wave background - except that they are stronger. They were used to verify the isotropic search code (see e.g. [90, 91]). The isotropic result is related to the radiometer output through equation 3.38. Rather than rerunning on the stochastic injections, I verified that equation 3.38 is fulfilled, which has to be the case even without injections.

The pulsar injections have the advantage that they were on during roughly half of the S4 run, but they are narrow-band and have a well-defined polarization. In particular a pulsar wave form is given by

$$h_i(t) = h_+ \cos(2\pi f t) + h_\times \sin(2\pi f t) \tag{3.48}$$

with

$$h_+ = E_i^+(t, \psi) h_0 \frac{1 + \cos^2 \iota}{2}$$
$$h_\times = E_i^\times(t, \psi) h_0 \, \cos \iota \tag{3.49}$$

Here ι is the angle between the neutron star's spin direction and the wave propagation direction, f the spin frequency, h_0 the wave amplitude and $E_i^A(t, \psi)$ the projection operator of polarization A on to detector i - it differs from $F_i^A(t)$ in that the $+$ and

$\times$ polarization are defined relative to the neutron star's spin axis. ($F_i^A(t)$ are defined relative to the earth's pole.) They are related by

$$\begin{pmatrix} E_i^+ \\ E_i^\times \end{pmatrix} = \begin{pmatrix} \cos 2\psi & \sin 2\psi \\ -\sin 2\psi & \cos 2\psi \end{pmatrix} \begin{pmatrix} F_i^+ \\ F_i^\times \end{pmatrix} \tag{3.50}$$

The radiometer code assumes that any correlation is due to an unpolarized source and weights the different observation times accordingly. Therefore the radiometer will estimate the strength of the pulsar as

$$H(f)df = \frac{\sum_{t_i}(E_1^+ E_2^+ + E_1^\times E_2^\times)(E_1^+ E_2^+ h_+^2 + E_1^\times E_2^\times h_\times^2)}{\sum_{t_i}(E_1^+ E_2^+ + E_1^\times E_2^\times)^2} \tag{3.51}$$

The sum has to be taken over all observation times t_i. Note that both h_+ and $h_\times$ are peak amplitudes, while $H(f)df$ is the RMS power due to the pulsar that is estimated by the radiometer. Equation 3.51 assumes that the interferometer noise stays constant, an assumption that is certainly broken by diurnal variations in the noise floor. This will introduce some systematics.

The parameters of the 3 strongest inject pulsars - named Pulsar3, Pulsar4 and Pulsar8 - are given in table 3.3.

Strongest injected pulsars during S4			
Parameter	Pulsar3	Pulsar4	Pulsar8
Freq. during S4	108.86 Hz	1402.20 Hz	193.94 Hz
h_+	6.5532×10^{-20}	9.8258×10^{-19}	6.3851×10^{-20}
$h_\times$	-1.0504×10^{-20}	5.0606×10^{-19}	9.3864×10^{-21}
Right ascension	$11h\ 53m\ 29.4s$	$18h\ 39m\ 57.0s$	$23h\ 25m\ 33.5s$
Declination	$-33d\ 26'\ 11.8''$	$-12d\ 27'\ 59.8''$	$-33d\ 25'\ 6.7''$
Hdf [(*)]	1.74×10^{-46}	4.28×10^{-44}	1.54×10^{-46}

Table 3.3: Table summarizing the parameters of the fake pulsars injected into Hardware during the S4 run. [(*)]: Hdf is the equivalent unpolarized RMS power that the radiometer should detect for the pulsar. It was calculated using equation 3.51, the actual pulsar injection times and a calibration correction amounting to 20%.

Table 3.4 summarizes the result of the pulsar hardware injection. Pulsar3 and Pulsar8 are consistent within the error bar. The high-SNR Pulsar4 strength is un-
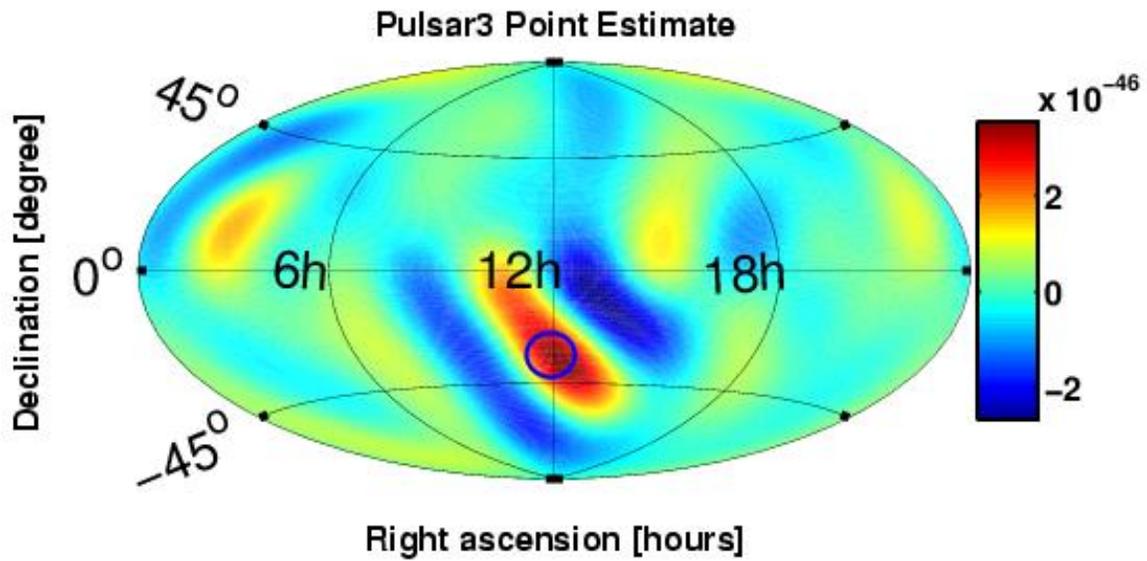
Figure 3-4: **Hardware Injection:** Pulsar3, 108.625 Hz - 109.125 Hz The circle marks the position of the injected pulsar.
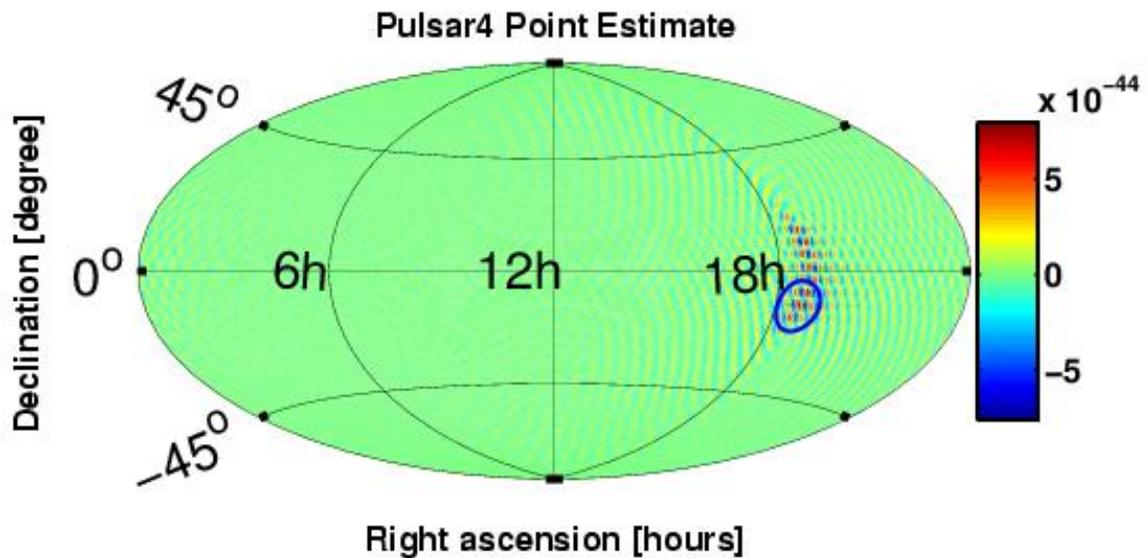
Figure 3-5: **Hardware Injection:** Pulsar4, 1401.875 Hz - 1402.375 Hz The circle marks the position of the injected pulsar.
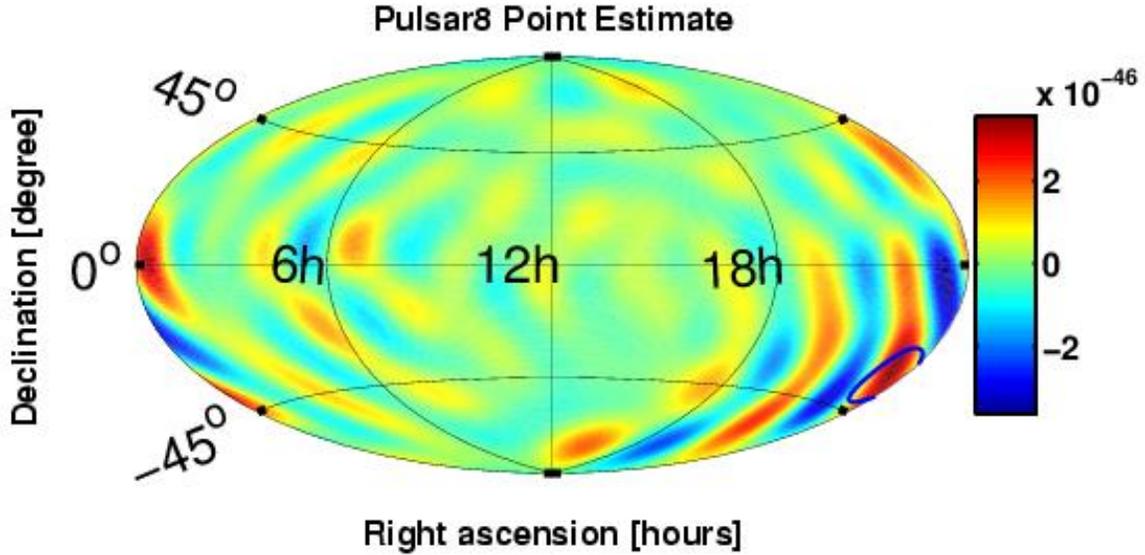
Figure 3-6: **Hardware Injection:** Pulsar8, 193.625 Hz - 194.125 Hz The circle marks the position of the injected pulsar.

Pulsars Hardware Injection			
Parameter	Pulsar3	Pulsar4	Pulsar8
Freq. during S4	108.86 Hz	1402.20 Hz	193.94 Hz
Max. SNR at	$12h$ $12m$	$18h$ $40m$	$23h$ $16m$
	$-37d$	$-13d$	$-32d$
Max. estimate at	$12h$ $12m$	$18h$ $40m$	$23h$ $12m$
	$-36d$	$-12d$	$-31d$
Max estimate Hdf	1.80×10^{-46}	4.05×10^{-44}	1.82×10^{-46}
Estimate Hdf on source	1.74×10^{-46}	4.05×10^{-44}	1.79×10^{-46}
Error bar	1.89×10^{-47}	6.04×10^{-46}	1.73×10^{-47}
SNR	9.2	67.1	10.3
inj. Hdf	1.74×10^{-46}	4.28×10^{-44}	1.54×10^{-46}

Table 3.4: Table summarizing the pulsar hardware injections. The effective power Hdf is given for both the location of the maximum and the true source location. The last line is the injected strength, see table 3.3. The resulting underestimate for the high-SNR Pulsar4 is probably due to a systematic bias in the power spectrum estimate when a strong signal is present [100]. The pulsar location is found accurately.

derestimated by 5%. Possible contributers to this factor are a systematic bias in the power spectrum estimate when a strong signal is present (see [100]), the bias arising from the diurnal sensitivity variations (see above) and a frequency bin acceptance

correction for the narrow-band pulsar signal that is due to the Hanning windowing.

3.4.4   Timing Transient

The first maps that I produced for the whole S4 run had an anomaly (low SNR) at the poles. The poles are special because they do not require a sidereal time dependent time shift. Thus I calculated the cross-correlation time series without sidereal time dependent time shift ($\gamma = 1$) and $H(f) = \frac{1\,\mathrm{Hz}^2}{f^3}$. The result was a -5σ correlation between H1 and L1 - the cross-correlation as a function of time shift and the square root of the integrated number of segments is shown in figure 3-7.
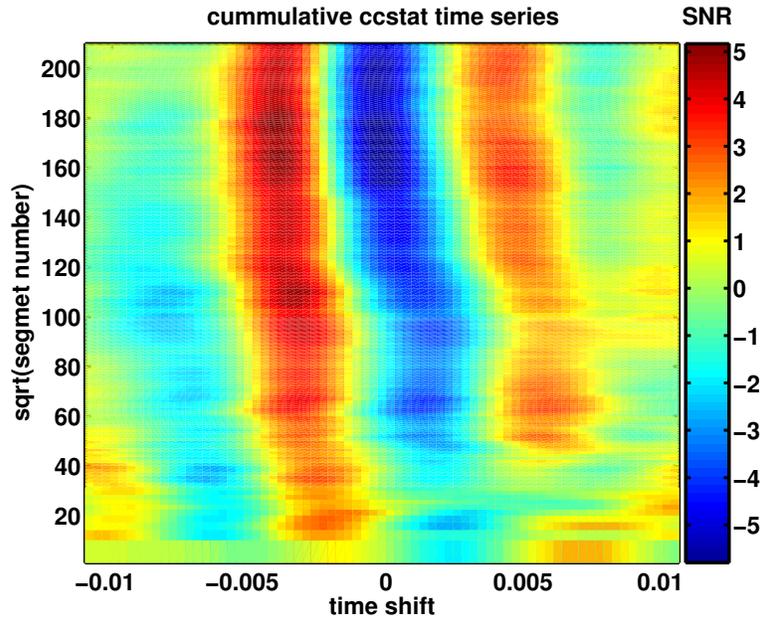
Figure 3-7: **Effect of timing transient:** Cross-correlation time series for a unity overlap reduction function ($\gamma = 1$) and $H(f) = \frac{1\,\mathrm{Hz}^2}{f^3}$ as a function of the square root of the integrated number of segments. For the whole S4 run there is a -5σ correlation between H1 and L1. This correlation is due to a periodic timing transient that was present in both interferometers (see figure 3-8).

This correlation was found to be due to an exactly 1-sec periodic signal in both interferometers (figure 3-8), which was caused by cross-talk from the GPS_RAMP signal. The GPS_RAMP signal is synchronized with the GPS receivers and consists of a 10 msec saw-tooth signal that starts at every full GPS second and lasts for 1

msec (see figure 3-8). This ramp was used as an off-line monitor of the ADC card timing and thus was hooked up to an LSC ADC card, which resulted in a non-zero cross-talk.
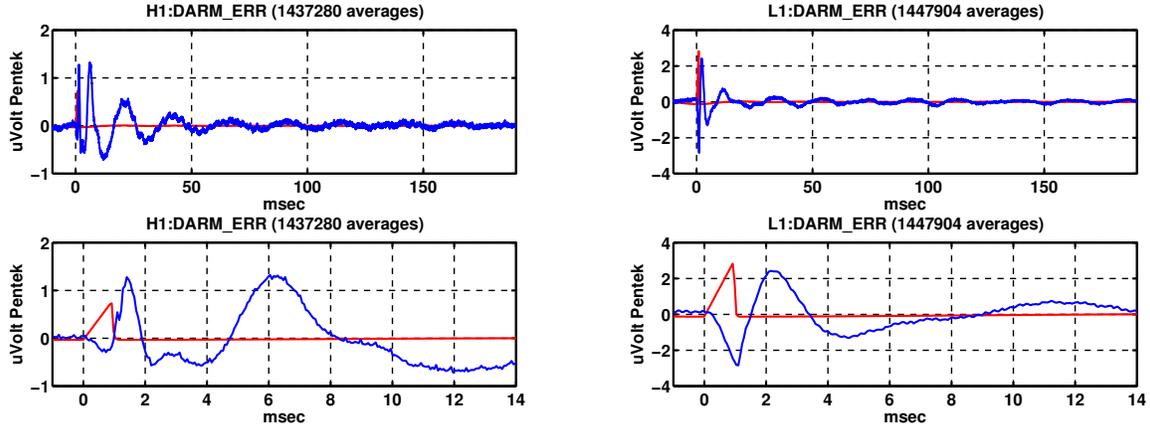
Figure 3-8: **Periodic timing transient** in DARM_ERR calibrated in μVolt at the ADC (Pentek card) for H1 (left) and L1 (right) shown with a span of 200 msec (top) and 14 msec (bottom) in blue. The x-axis is the offset from a full GPS second. About 1.4 million seconds of DARM_ERR data was averaged to get this trace. Also shown in red is the GPS_RAMP signal that was used as a timing monitor. It was identified as cause for the periodic timing transient in DARM_ERR. The H1 trace shows an additional feature at 6 msec since its GPS_RAMP signal was routed through a whitening board.

There are two ways to remove this signal from the data stream. On can notch every full Hz frequency bin. To reduce the amount of lost data this requires longer time segments which in turn makes the handling of the non-stationarity harder and increases the memory usage of the code. While these are both solvable problems, I chose the second way mostly because it is more elegant.

This second way is to subtract the transient in time domain. This has the advantage that only a very narrow band ($1/\text{runtime} \approx 1 \times 10^{-6}$ Hz) is removed while the rest of the analysis is completely unaffected. The wave form for subtraction from the raw (uncalibrated) data was recovered by averaging the data from the whole run together to produce a typical second. Additionally - since this typical second only showed significant features in the first 80 msec - the transient subtraction template was set to zero (with a smooth transition) after 120 msec (figure 3-9).
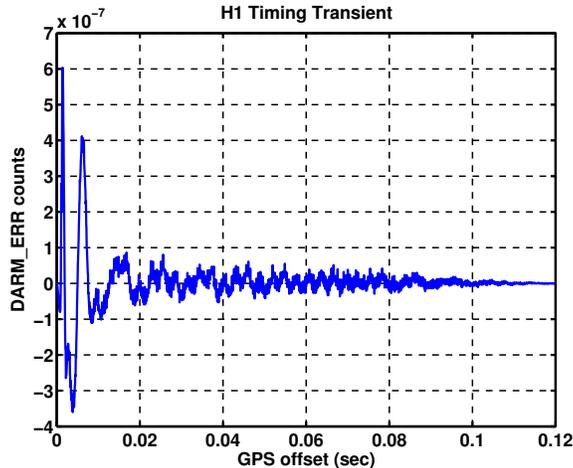
Figure 3-9: **H1 timing transient** in raw DARM_ERR counts that was used in the analysis to remove the effect. The first 80 msec are identical to the trace shown in figure 3-8A, after that it smoothly transitions to zero. No similar subtraction was made to L1 to avoid introducing accidental correlation.

This subtraction was only done for H1 since adding repetitive data to both detectors can introduce artificial correlation. This subtraction efficiently eliminated the observed correlation. Furthermore all hardware injection results (section 3.4.3) were obtained with this subtraction. For the S5 run the GPS_RAMP signal was replaced with a two-tone signal at 900 Hz and 901 Hz. The beat between the two is now used to monitor the timing.

3.4.5 Data cuts and post processing

The LIGO Detector Characterization working group has put together a list of all known types of data degradation, including the times during which they occurred [102]. Some of these so called Data Quality Flags indicate problems that should be excluded a priori form the analysis.

Table 3.5 summarizes the data quality flags that were excluded a priori. Most of them are obviously required, the rest were used since the amount of data lost is minimal and it was easier to stay on the safe side.

Additionally a minimum segment duration of 182 seconds was required (60 seconds of usable data + 60 seconds on each side for a power spectrum estimate + 1 second at

the beginning and end for cutting filtering transients). This cut is already included in the numbers of table 3.5.

Applied data quality flags			
Data quality flag	hours	%	Description
H1:ADC_OVERFLOW	0.46	0.09 %	ADC out of range
L1:ADC_OVERFLOW	1.31	0.27 %	
H1:CALIB_LINE_DROPOUT	0.20	0.04 %	Calibration line
H1:CALIB_LINE_V04_1_SEC	0.06	0.01 %	not present
H1:CALIB_LINE_V04_60_SEC	0.45	0.09 %	(different causes)
L1:CALIB_LINE_DROPOUT	0.24	0.05 %	
L1:CALIB_LINE_V04_1_SEC	0.14	0.03 %	
L1:CALIB_LINE_V04_60_SEC	0.99	0.20 %	
H1:INJECTION_BURST	1.64	0.34 %	Period of
H1:INJECTION_INSPIRAL	2.60	0.53 %	Hardware Injection,
H1:INJECTION_PULSTART	0.12	0.02 %	for Pulsar injection
H1:INJECTION_STOCHASTIC	9.62	1.97 %	only start and stop
L1:INJECTION_BURST	1.50	0.31 %	times are reported
L1:INJECTION_INSPIRAL	1.88	0.39 %	
L1:INJECTION_PULSTART	0.03	0.01 %	
L1:INJECTION_STOCHASTIC	9.96	2.04 %	
H1:OUTSIDE_S4	15.40	3.15 %	Data not available
L1:NO_DATA	5.03	1.03 %	
L1:NO_RDS	5.17	1.06 %	
L1:OUT_OF_LOCK	26.79	5.49 %	
L1:OUTSIDE_S4	15.40	3.15 %	
H1:PRELOCKLOSS_30	0.47	0.10 %	Excludes 30 sec
L1:PRELOCKLOSS_30	1.04	0.21 %	before lock-loss
Total time after cuts	435.25	89.14 %	
Total time before cuts	488.27	100.00 %	

Table 3.5: **Data quality flags** that were a priori excluded from science data. The individual flags do overlap partially, so the total amount of lost data is smaller than the sum of all individual flags.

One post-processing cut was required to deal with the detector non-stationarity. To avoid a bias in the cross-correlation statistics the 2 adjacent segments are used for the power spectral density (PSD) estimate [100]. Therefore the analysis becomes vulnerable to large, short transients that happen in one instrument in the middle segment - such transients cause a significant underestimate of the PSD and thus of the theoretical standard deviation for this segment. This leads to a contamination of

the final estimate.

To eliminate this problem the standard deviation σ is estimated for both the middle segment and the 2 adjacent segments. The two estimates are then required to agree within 20%

$$\left| \log \frac{\sigma_{\text{middle}}}{\sigma_{\text{adjacent}}} \right| < \log 1.2 \tag{3.52}$$

The analysis is fairly insensitive to the threshold - the only significant contamination comes from gigantic outliers that are cut by any reasonable threshold. The chosen threshold of 20% eliminates less than 6 % of the data.
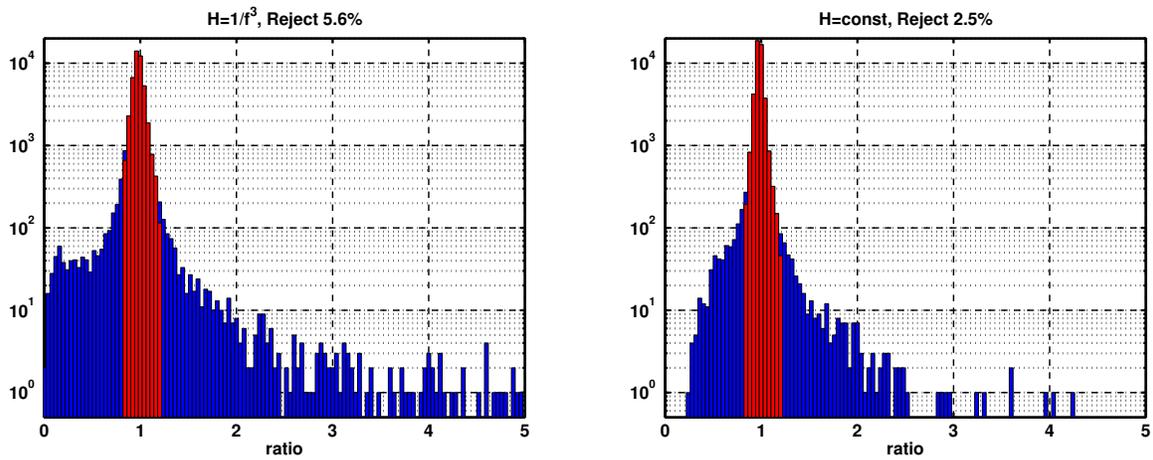
Figure 3-10: **Histogram of the ratio** $\sigma_{\text{middle}}/\sigma_{\text{adjacent}}$ for the final S4 analysis (see chapter 4). Left for $H(f) = \frac{1 \text{ Hz}^2}{f^3}$, right for $H(f) = 1 \text{ Hz}^{-1}$. Blue is before the cut, red after the cut (eq. 3.52).

Chapter 4

Results from S4

The LIGO S4 science run consisted of one month of coincidence data taking with all three LIGO interferometers (22 Feb 2005 noon to 23 Mar 2005 midnight CST). During that time all three interferometers where roughly a factor of 2 away from design sensitivity over almost the whole frequency band. Also, the Livingston interferometer was equipped with a Hydraulic External Pre-Isolation (HEPI) system, allowing it to stay locked during day time. This made S4 the first LIGO science run with all-day coverage at both sites.

Since the radiometer analysis requires two spatially separated sites I only used data from the two 4 km interferometers (H1 in Hanford and L1 in Livingston). For these two interferometers, about 20 days of coincident data was collected, corresponding to a duty cycle of 69%.

4.1 Broadband results

As mentioned at the beginning of chapter 3 the only real restriction of a stochastic search is a significant source duty cycle, with the caveat that the method is only optimal if the waveform is not known.

Consequently the main purpose of doing a directional stochastic search is to set a limit on possibly unknown sources. Nevertheless the shape of source power spectrum $H(f)$ has to be chosen a priori. Arguably the simplest possible assumption is to

choose some power law for $H(f)$. I chose two different power laws for $H(f)$:

- *Constant $\Omega_{\mathrm{gw}}(f)$:* $H(f) = \frac{1\ \mathrm{Hz}^2}{f^3}$ This emphasizes low frequencies and is useful when interpreting the result in a cosmological framework, since it corresponds to a scale-invariant primordial perturbation spectrum.

- *Constant strain power:* $H(f) = 1\ \mathrm{Hz}^{-1}$ This simply emphasizes the frequencies for which the interferometer strain sensitivity is highest.

The results are reported as point estimate Y and corresponding standard deviation σ for each pixel (see section 3.3.3). The point estimate Y has to be interpreted as best fit assuming a source spectral shape $H(f)$, i.e. the best estimate for the true source spectrum is $H_Y(f) = Y H(f)$.

4.1.1 Constant $\Omega_{\mathrm{gw}}(f)$
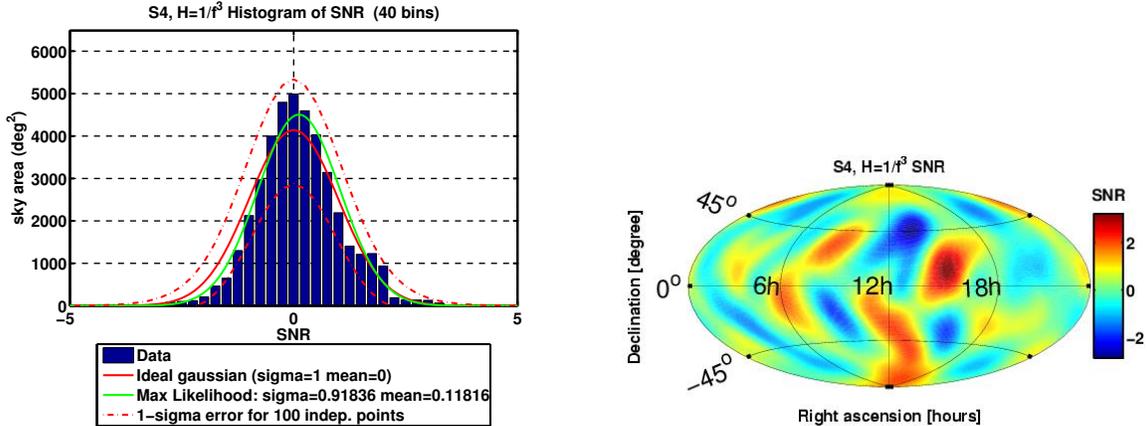
Figure 4-1: **S4 Result:** Histogram (left) and map (right) of the bias corrected signal-to-noise ratio (SNR) for $H(f) = \frac{1\ \mathrm{Hz}^2}{f^3}$. The green curve is a maximum likelihood Gaussian fit to the data. The red solid line is an ideal Gaussian, the two dash-dotted red lines are the 1-σ bands around the ideal Gaussian for $N_{\mathrm{eff}} = 100$.

Figure 4-1 shows a histogram and a map of the bias-corrected SNR $= \frac{Y}{\sigma}$. It was produced by weighting all data points on the map with the corresponding sky area in square degrees. But neighboring points are correlated, effectively reducing the number of independent points N_{eff}. That is why the histogram can look non-Gaussian

even though the data is still consistent with (correlated) Gaussian noise. Indeed the histogram in figure 4-1 features a slight bump around SNR=2, but is still consistent with $N_{\text{eff}} = 100$ - the red dash-dotted lines indicate the 1-σ bands around the red ideal Gaussian for $N_{\text{eff}} = 100$. The histogram is clearly consistent with them. Additionally the SNR distribution also passes a Kolmogorov-Smirnov test for $N_{\text{eff}} = 100$ ($\alpha = 0.1$).

So far though I do not know of any precise way to calculate N_{eff}. However I applied 2 heuristic methods that produced roughly the same answer:

- *Spherical harmonics decomposition* of the SNR map. The resulting power vs l graph shows structure up to roughly $l = 9$ and falls of steeply above that - the $l = 9$ point corresponds to one twentieth of the maximal power. The effective number of independent points then is $N_{\text{eff}} \approx (l + 1)^2 = 100$.

- *FWHM area* of a strong injected source, which is latitude dependent but of the order of 800 deg^2. To fill the sky we need about $N_{\text{eff}} \approx 50$ of those patches. This is probably even an overestimate because the correlation angle is bigger than the FWHM angle. Nevertheless, I used the higher $N_{\text{eff}} = 100$ for this discussion.

Figure 4-1 suggests that the data is consistent with no signal. Thus I calculated a Bayesian 90% upper limit for each sky direction. The prior was assumed to be flat between zero and infinity (even though a single interferometer power spectrum sets a tighter limit than any previous experiments). Additionally I marginalized over the calibration uncertainty of 8 % for H1 and 5% for L1 using a Gaussian probability distribution. The resulting upper limit map is shown in figure 4-2. The upper limits on the strain power spectrum $H(f)$ vary between roughly $1.2 \times 10^{-48} \text{Hz}^{-1} \left(\frac{100 \text{ Hz}}{f} \right)^3$ and $1.2 \times 10^{-47} \text{Hz}^{-1} \left(\frac{100 \text{ Hz}}{f} \right)^3$ depending on the exact position in the sky.

For completeness figure 4-3 also shows the point estimate and theoretical standard deviation maps.

S4, H=1/f³ 90% confidence upper limit
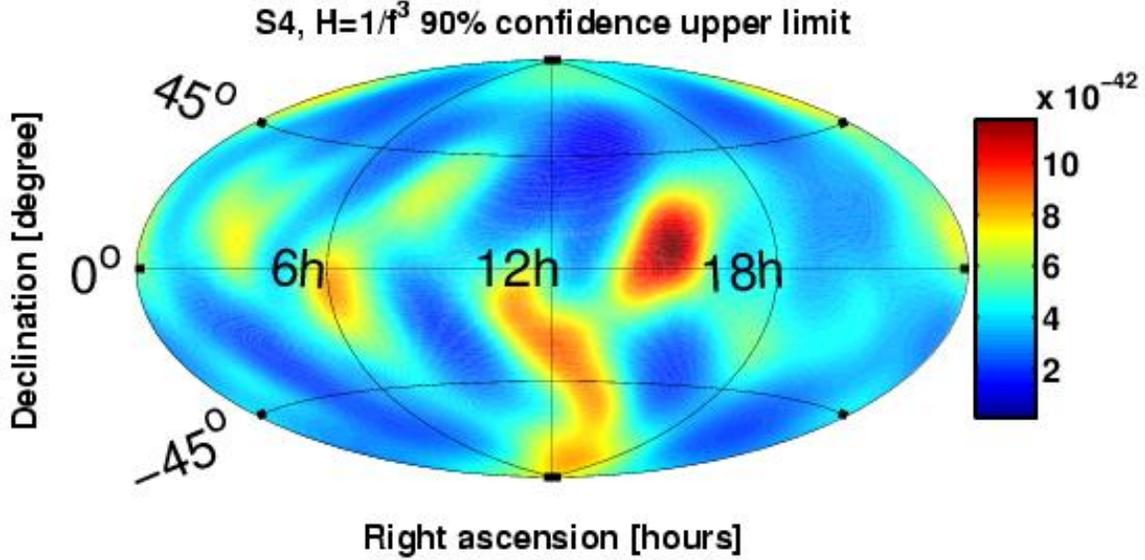
Figure 4-2: **S4 Final Result:** Map of the 90 % confidence level Bayesian upper limit for $H(f) = \frac{1\,\mathrm{Hz}^2}{f^3}$. The upper limit varies between roughly $1.2 \times 10^{-48}\mathrm{Hz}^{-1}\left(\frac{100\,\mathrm{Hz}}{f}\right)^3$ and $1.2 \times 10^{-47}\mathrm{Hz}^{-1}\left(\frac{100\,\mathrm{Hz}}{f}\right)^3$ depending on the exact position in the sky.

Figure 4-3: **S4 Result:** Map of the point estimate Y (left) and the theoretical standard deviation σ for $H(f) = \frac{1\,\mathrm{Hz}^2}{f^3}$.

4.1.2 Constant strain power

As before figure 4-4 shows a histogram and a map of the bias-corrected SNR $= \frac{Y}{\sigma}$. Structure in the spherical harmonics power spectrum goes up to $l = 19$, thus N_{eff} was estimated to be $N_{\mathrm{eff}} \approx (l+1)^2 = 400$. Alternatively the FWHM area of a strong injection covers about 100 deg² which also leads to $N_{\mathrm{eff}} \approx 400$. The dash-dotted red lines in the histogram (figure 4-4) correspond to the expected $1 - \sigma$ deviations from the ideal Gaussian for $N_{\mathrm{eff}} = 400$. The histogram is thus consistent with (correlated)

Gaussian noise, indicating that there is no signal present. The SNR distribution also passes a Kolmogorov-Smirnov test for $N_{\text{eff}} = 400$ ($\alpha = 0.1$).
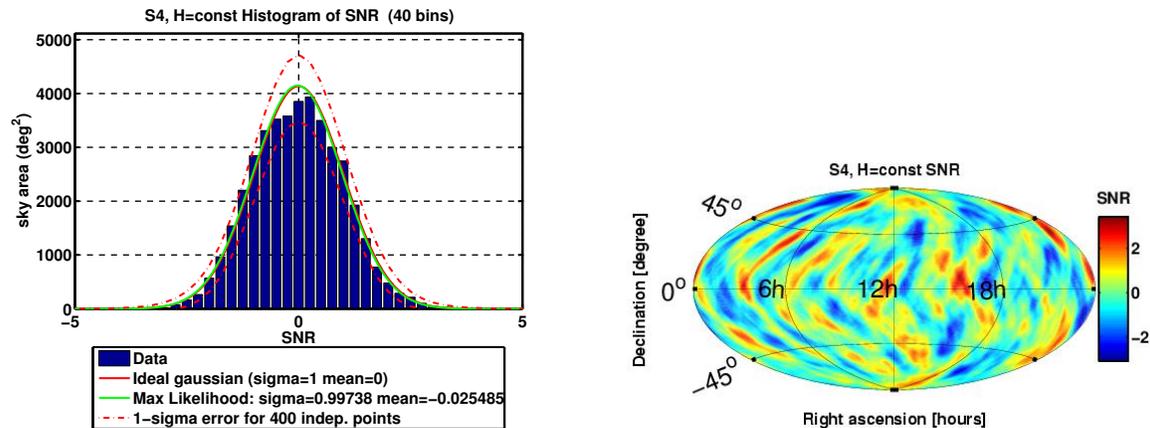
Figure 4-4: **S4 Result:** Histogram (left) and map (right) of the bias corrected signal-to-noise ratio (SNR) for $H(f) = 1 \text{ Hz}^{-1}$. The green curve is a maximum likelihood Gaussian fit to the data. The red solid line is an ideal Gaussian, the two dash-dotted red lines are the $1 - \sigma$ bands around the ideal Gaussian for $N_{\text{eff}} = 400$.

Again I calculated a Bayesian 90% upper limit for each sky direction, including the marginalization over the calibration uncertainty. The prior was assumed to be flat between 0 and ∞. The resulting upper limit map is shown in figure 4-5. The upper limits on the strain power spectrum $H(f)$ vary between roughly $8.5 \times 10^{-49} \text{Hz}^{-1}$ and $6.1 \times 10^{-48} \text{Hz}^{-1}$ depending on the exact position in the sky.

Finally figure 4-6 also shows the point estimate and theoretical standard deviation maps.

### 4.1.3   Interpretation

The maps presented in figures 4-2 and 4-5 show the first directional upper limits on a stochastic gravitational wave background ever obtained. They are consistent with no gravitational wave background being present. The most important aspect of this result is that it sets a limit on unexpected nearby sources, which means the interpretation ends with the limit on the strain power spectrum.

On the other hand one can interpret the result in terms of potential sources. As an example I look at the gravitational luminosity of all LMXBs within the Virgo galaxy
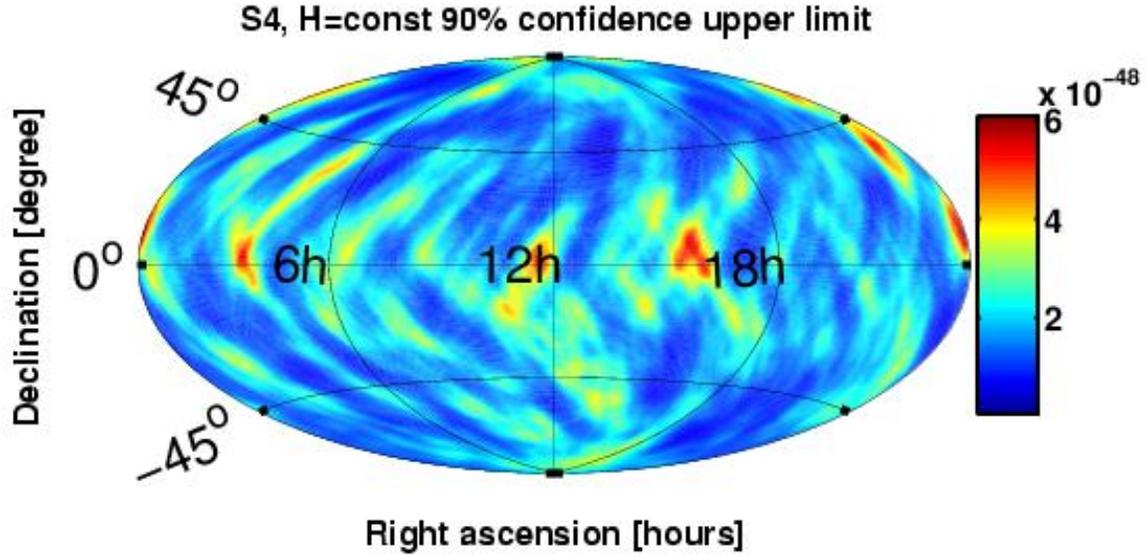
Figure 4-5:   **S4 Final Result:** Map of the 90 % confidence level Bayesian upper limit for $H(f) = 1$ Hz^{-1}.The upper limit varies between roughly 8.5×10^{-49}Hz^{-1} and 6.1×10^{-48}Hz^{-1} depending on the exact position in the sky.
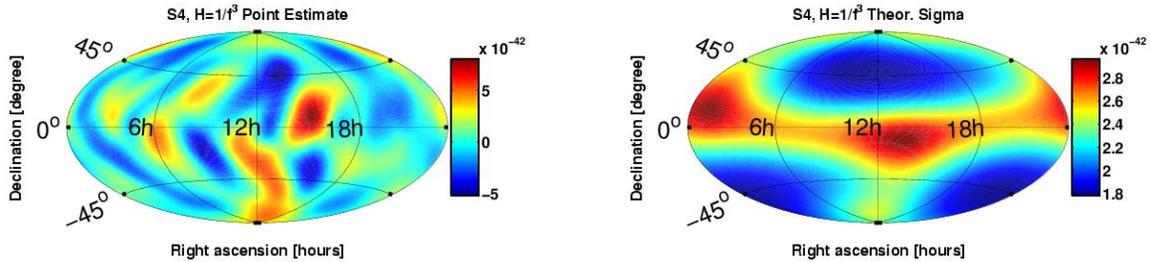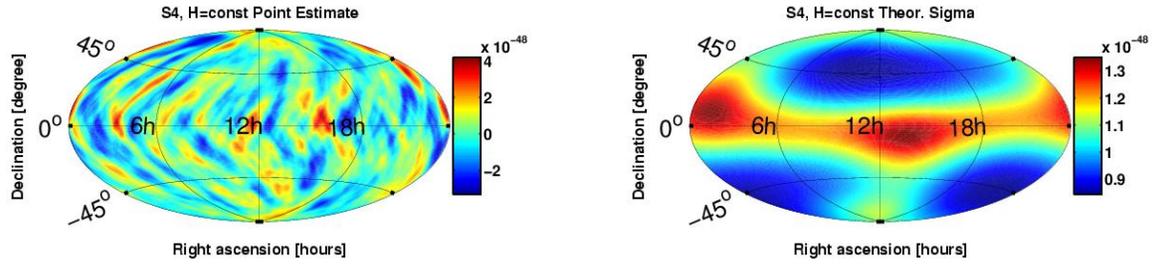

Figure 4-6:   **S4 Result:** Map of the point estimate Y (left) and the theoretical standard deviation σ for $H(f) = 1$ Hz^{-1}.

cluster. They have an integrated X-ray luminosity of about 1×10^{-9} erg/sec/cm^2 (see equation 3.19). For simplicity I assume that they produce a flat strain power spectrum $H(f)$ over a bandwidth Δf. Then the strength of this strain power spectrum is about

$$H(f) = \frac{2G}{\pi c^3} \frac{1}{f_{\text{Kepler}} f \Delta f} F_X \approx 10^{-55} \text{ Hz}^{-1} \left(\frac{100 \text{ Hz}}{f} \right) \left(\frac{100 \text{ Hz}}{\Delta f} \right) \tag{4.1}$$

which is clearly out of reach.

4.2 Limits on isotropic background

Using formula 3.38 it is possible to recover the point estimate and standard deviation for the isotropic case (see also appendix C.4). From that the 90% Bayesian upper limit can be calculated. I additionally marginalize over the DC calibration uncertainty. Setting the Hubble constant to $72\frac{\text{km}}{\text{sec Mpc}}$, the 90% upper limit I can set on $\Omega_{\text{gw}}(f)$ is 1.20×10^{-4}. Alternatively, assuming a flat strain power spectrum, the limit is $5.13 \times 10^{-5} \left(\frac{f}{100\text{Hz}}\right)^3$. Table 4.1 summarizes that result.

S4 isotropic upper limit		
Quantity	$\Omega_{\text{gw}}(f) = const$	$S_{\text{gw}}(f) = const$
point estimate Y	$1.02 \times 10^{-47}\text{Hz}^{-1} \left(\frac{f}{100\text{Hz}}\right)^{-3}$	$-7.12 \times 10^{-48}\text{Hz}^{-1}$
standard deviation σ	$6.97 \times 10^{-48}\text{Hz}^{-1} \left(\frac{f}{100\text{Hz}}\right)^{-3}$	$7.22 \times 10^{-48}\text{Hz}^{-1}$
DC calibration uncertainty H1	$\pm 8\%$	
DC calibration uncertainty L1	$\pm 5\%$	
90% Bayesian UL on $S_{\text{gw}}(f)$	$1.99 \times 10^{-47}\text{Hz}^{-1} \left(\frac{f}{100\text{Hz}}\right)^{-3}$	$8.49 \times 10^{-48}\text{Hz}^{-1}$
90% Bayesian UL on $h^2\Omega_{\text{gw}}(f)$	6.25×10^{-5}	$2.66 \times 10^{-5} \left(\frac{f}{100\text{Hz}}\right)^3$

Table 4.1: **S4 final isotropic result** for the $\Omega_{\text{gw}}(f) = const$ and the $S_{\text{gw}}(f) = const$ case. The first two lines show point estimate and standard deviation that are used to calculate the 90% Bayesian upper limits. Those upper limits are also marginalized over the calibration uncertainty.

4.2.1 Interpretation

The limit on an isotropic stochastic background of gravitational waves that can be set with the S4 data is roughly one order of magnitude lower than the published LIGO S3 limit [91], which already was by far the best experimental limit in the terrestrial accessible frequency band (see section 3.1.1). In fact LIGO has the prospect of improving on the Nucleosynthesis bound of $\Omega_{\text{gw}} \lesssim 1.2 \times 10^{-5}$ in the current and future science runs.

4.3 Narrow-band results targeted on Sco-X1

The gravitational wave flux from all LMXB is expected to be dominated by the closest one, Sco-X1 (see section 3.2.1). Unfortunately its spin frequency is not really known. I thus want to set an upper limit for each frequency bin on the RMS strain coming from the direction of Sco-X1 (see table 3.2). The bin width I chose was $df = 0.25$ Hz, which is the same bin width that was used for the broadband analysis. To choose a narrower band, corrections for the orbital phase of the companion star would have to be made (see equation 3.22).

To avoid contamination from the injected pulsars, the 2 frequency bins next to a pulsar frequency were excluded. Multiples of 60 Hz were also excluded. The lowest frequency was 50 Hz, the highest was 1799.75 Hz. The left side of figure 4-7 shows a histogram of the remaining 6965 0.25 Hz wide frequency bins. It is consistent with a Gaussian distribution (Kolmogorov-Smirnov test with $N = 6965$ and $\alpha = 0.1$).
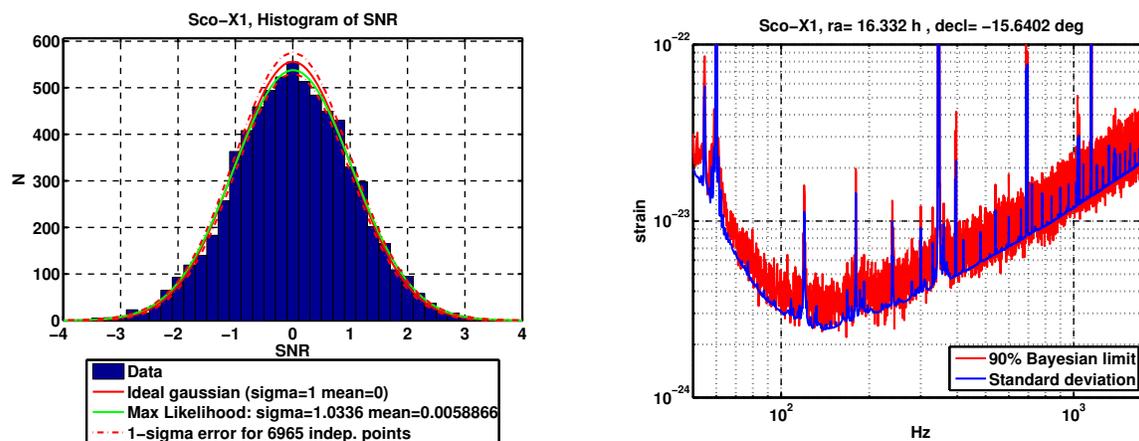
Figure 4-7: **S4 Result for Sco-X1:** For each 0.25 Hz wide frequency bin a pint estimate and standard deviation is calculated. The resulting SNR is histogrammed on the left side. There are no outliers. The resulting 90% confidence Bayesian upper limit as a function of frequency - marginalized over the calibration uncertainty, is plotted on the right (red). Also shown is the standard deviation (blue).

A 90% Bayesian upper limit for each frequency bin was calculated based on the point estimate and standard deviation, including a marginalization over the calibration uncertainty (H1: 8%; L1: 5%). The right side of figure 4-7 is a plot of this 90% limit (red trace). Above about 200 Hz (shot noise regime above cavity pole) the

typical upper limit rises linearly with frequency and is given by

$$h_{\mathrm{RMS}}^{(90\%)} \approx 8.4 \times 10^{-24} \left(\frac{f}{500 \text{ Hz}} \right) \quad f \gtrsim 200 \text{ Hz} \tag{4.2}$$

The standard deviation is also shown in blue.

4.3.1   Interpretation

The radiometer analysis is clearly not the optimal way to go after a presumably periodic source like Sco-X1. Nevertheless it can set an upper limit with a minimal set of assumptions on the source. The frequency resolution of 0.25 Hz presented here is close to the minimal bandwidth that is required if one does not correct for orbital parameters of the source.

The upper limit (eq. 4.2) can directly be compared to the expected strain based on the X-ray luminosity (eq. 3.21):

$$\frac{h_{\mathrm{RMS}}^{(90\%)}}{h_{\mathrm{RMS}}^{L_X}} \approx 440 \left(\frac{f}{500 \text{ Hz}} \right)^{\frac{3}{2}} \tag{4.3}$$

Here f is the gravitational wave frequency, i.e. twice the (unknown) spin frequency of Sco-X1. So we really don't expect to see anything yet. Furthermore the upper limit for the strain scales as $\left(\frac{df}{T} \right)^{1/4}$, with df the bin width and T the total run duration. So even if one integrates for a year, corrects for all orbital frequency shifts and reduces df to the intrinsic limit of 8×10^{-5} Hz (eq. 3.23) the upper limit on the strain improves only by a factor of 16. Clearly the way to go is to further improve the interferometer sensitivity - since S4 the strain sensitivity has already been increased by 2 to 3, depending on the frequency.

Conclusion

At the time of writing all three LIGO interferometers have reached or surpassed their design sensitivity and are now acquiring science data. To reach this goal, it was critical to increase the power in the interferometer to more than 200 Watts incident on the beam splitter. This required the commissioning of both a thermal compensation system (TCS) and shot noise limited sensing electronics capable of detecting all the light. Additionally, a series of unexpected noise sources had to be mitigated. All of these steps are discussed in chapter 2. While reaching the design sensitivity is a key milestone for the LIGO project, the current interferometers still have the potential for at least a factor of 2 of improvement in strain sensitivity [50].

In a second part I introduce a radiometer analysis that uses the cross-correlation of the data streams from two spatially separated gravitational wave interferometers to spatially resolve anisotropies in a stochastic gravitational wave background. The analysis is optimized for identifying point sources of stochastic gravitational radiation.

Data from the fourth LIGO science run (S4) was analyzed and no stochastic gravitational wave background was seen. The limit on a broadband and flat strain power spectrum coming from a point source varies between $8.5 \times 10^{-49} \mathrm{Hz}^{-1}$ and $6.1 \times 10^{-48} \mathrm{Hz}^{-1}$ depending on the source position. Also a limit on gravitational radiation coming from Sco-X1, a Low-Mass X-ray binary and the brightest X-ray source in the sky, is set for each frequency bin (see figure 4-7).

Additionally a bound of $h^2 \Omega_{\mathrm{gw}}(f) < 6.25 \times 10^{-5}$ was set on an isotropic gravitational wave energy density. The ongoing extended science run also holds the promise of improving on the Nucleosynthesis bound of $\Omega_{\mathrm{gw}} \lesssim 1.2 \times 10^{-5}$.

Appendix A

Tables of Parameters

Physical Constants			
Parameter	Symbol	Value	Units
Speed of Light	c	299792458	m/s
Planck's Constant	h	6.6261×10^{-34}	J s
Boltzmann's Constant	k_B	1.380×10^{-23}	J/K
Electron Charge	e_c	1.602×10^{-19}	C
Gravitational Constant	G	6.674×10^{-11}	$\text{m}^3/\text{kg}/\text{s}^2$
Fine Structure Constant	α	$1/137.036$	-
Stefan-Boltzmann Constant	σ_B	5.67×10^{-8}	$\text{W}/\text{m}^2/\text{K}^4$
Avogadro Constant	N_A	6.022×10^{23}	mol^{-1}
Solar mass	$M_\odot$	1.9889×10^{30}	kg

Table A.1: Values of constants from the NIST CODATA web page [78]

Large Optic Parameters; Substrate: Fused Silica (Amorphous SiO_2)			
Parameter	Symbol	Value	Units
Specific Heat	C	740	J/kg/K
Refractive Index (@ 1064 nm)	n	1.45	-
Thermal Conductivity	κ	1.38	W m^{-1} K^{-1}
Young's Modulus (substrate)	E_S	72.80	GPa
Young's Modulus (coating)	E_C	100	GPa
Poisson Ratio	η	0.170	-
Thermal expansion coef.	α	0.55	ppm/K
Thermo-Optic coef. (1μm)	$\beta = \frac{dn}{dT}$	11.9	ppm/K
Emissivity (10.6μm)	ϵ	0.9	-
Thickness (coating)	d_C	8×10^{-6}	m
Loss Angle (substrate)	ϕ_S	1×10^{-7}	-
Loss Angle (coating)	ϕ_C	2×10^{-4}	-
Density	ρ	2196	kg/m^3
Optic Radius	R_{LOS}	0.125	m
Optic Diameter	$\varnothing$	0.250	m
Optic Thickness	h_{LOS}	0.100	m
Optic Thickness (BS)	h_{BS}	0.040	m
Optic Mass	m_{LOS}	10.5	kg
Optic Mass (BS)	m_{BS}	4.2	kg

Table A.2: Parameters for the optics are only approximate. There is an optic to optic variation in dimensions due to the varying wedge angles. Thickness is measured at the *thickest* point for all optics except the BS where it is measured at the *thinnest* point. Values are taken from [51], [67] and [77].

Description of Variables		
Variable Symbol	Description	Value (for H1)
P	Power into the interferometer	$\approx$ 4 Watt
g_{cr}	Carrier amplitude recycling gain	*7.1*
$G_{cr} = g_{cr}^2$	Carrier recycling gain	*50**
g_{sb}	Sideband amplitude recycling gain	*5.5*
$G_{sb} = g_{sb}^2$	Sideband recycling gain	*30*
t_{sb}	Sideband transmission to the AS port from the IFO input	*0.995*** ≈ 0.77
r_{cr}	Interferometer carrier reflectivity	*0.163***
r_c	Arm cavity carrier reflectivity	*0.990*
r_c'	Derivative of r_c w.r.t. cavity round trip phase	*139*
$\mathcal{F}$	Arm cavity finesse	*219*
FSR	Arm cavity Free Spectral Range	37.520 kHz
f_{TM}	Arm cavity transverse mode spacing	11.5 kHz
L_x	Length of the X-arm cavity	3995.0562 m
L_y	Length of the Y-arm cavity	3995.0724 m
f_c	Arm cavity pole frequency	85 Hz
t_M	Michelson transmission for the sidebands	*0.18*
l_D	Schnupp asymmetry $(l_x - l_y)$	0.356 m
T_{RM}	RM power transmission	0.027
T_{ITM}	ITM power transmission	0.028
Γ	Modulation depth in radians	0.4
$\aleph$	Optical gain pre-factor	-
$\omega_m/(2\pi)$	Resonant sideband frequency	24.480954 MHz
$\omega_{nr}/(2\pi)$	Non-resonant sideband frequency	61.202385 MHz
FSR_{MC}	Free Spectral Range of the MC	12.240477 MHz
f_{MC}	MC pole frequency	4.59 kHz
RoC_{ETMX}	ETMX radius of curvature on HR side	7.26 km
RoC_{ETMY}	ETMY radius of curvature on HR side	7.32 km
RoC_{ITMX}	ITMX radius of curvature on HR side	13.91 km
RoC_{ITMY}	ITMY radius of curvature on HR side	13.6 km
RoC_{RM}	RM radius of curvature on HR side	14.4 km
RoC_{BS}	BS radius of curvature on HR side	-336 km

Table A.3: Definition of variables and their value for H1. *Italic* values are calculated using the known mirror transmissions and interferometer geometry following [47]. (*) An arm round trip loss of 140*ppm* was assumed to fit G_{cr} to the experimentally observed value. (**) In reality the sideband transmission to the AS port is significantly worse than in the model. The uncertainties of all measured values are in the last digit. The optics parameters were taken from [75]. Other references: [65, 66]

DEFINITIONS of ACRONYMS	
ACRONYM	DEFINITION
IFO	Interferometer
RM	Recycling Mirror
BS	Beam Splitter
ITMX	Input Test Mass, X-Arm
ITMY	Input Test Mass, Y-Arm
ETMX	End Test Mass, X-Arm
ETMY	End Test Mass, Y-Arm
LSC	Length Sensing & Control
ISC	Interferometer Sensing & Control
OSEM	Optical Sensor and Electro-Magnetic actuator
PD	Photo-Detector
RFPD	Radio Frequency Photo-Detector
ASC	Alignment Sensing & Control
WFS	Wavefront Sensor
QPD	Quadrant Photo-Detector
SEI	Seismic Isolation
TCS	Thermal Compensation System
IOO	Input Output Optics
PSL	Pre-Stabilized Laser
FSS	Frequency Stabilization Servo
PMC	Pre-Mode Cleaner
ISS	Intensity Stabilization Servo
PC	Pockels Cell
MC	Mode Cleaner
OMC	Output Mode Cleaner
BSC	Barbecue Sauce Container
HAM	Horizontal Access Module
RGA	Residual Gas Analyzer
PZT	Lead Zirconate Tantanate
FAS	Fine Actuation System
PEPI	Piezo-Electric Pre-Isolator
HEPI	Hydraulic External Pre-Isolator
COC	Core Optics Components
MMT	Mode Matching Telescope
LVEA	Large Vacuum Equipment Area
SUS	Suspension
LOS	Large Optic Suspension
SOS	Small Optic Suspension
IIR	Infinite Impulse Response
FIR	Finite Impulse Response

Table A.4:

Appendix B

Useful formulas and definitions

B.1 Fabry-Perot Cavity

B.1.1 Reflection, transmission and buildup

For a cavity consisting of input mirror M1 (power reflectivity R_1 and power transmission T_1) and end mirror (power reflectivity R_2 and power transmission T_2) the reflected field E_R, the transmitted field E_T and the intra-cavity field E_c are

$$
\begin{aligned}
E_R &= E_{in} \left(\frac{T_1 \sqrt{R_2} e^{i\phi}}{1 - \sqrt{R_1 R_2} e^{i\phi}} - \sqrt{R_1} \right) \\
E_T &= E_{in} \left(\frac{\sqrt{T_1 T_2} e^{i\phi/2}}{1 - \sqrt{R_1 R_2} e^{i\phi}} \right) \\
E_C &= E_{in} \left(\frac{\sqrt{T_1}}{1 - \sqrt{R_1 R_2} e^{i\phi}} \right)
\end{aligned}
\tag{B.1}
$$

where $\phi = 2kL = 2\pi \frac{f}{\text{FSR}}$ is the round trip phase, k the wave vector, L the cavity length, f the laser frequency and FSR $= \frac{c}{2L}$ the free spectral range.

B.1.2 Transfer functions for modulations

Near resonances the line forms are Lorentzian, i.e.

$$
E_{T,C} \propto \frac{1}{1 + i\frac{f}{f_0}}, \quad f_0 = \frac{(1 - \sqrt{R_1 R_2})\text{FSR}}{2\pi \sqrt{R_1 R_2}}
\tag{B.2}
$$

f_0 is the half-max-half-width (in terms of power) of the Lorentzian line and is also called cavity pole because both frequency and amplitude modulations on the input laser light are filtered with one real pole at f_0, i.e the transfer function is $1/(1+if/f_0)$. Strictly speaking this is only true as long as the modulation frequency is not much bigger than the pole frequency. It obviously completely fails at multiples of the FSR. For example at the first FSR the transfer function can be approximated by

$$\frac{2\left(1+i\frac{f}{f_0}\right)}{\left(1+\frac{\text{FSR}^2}{f_0^2}\right)\left(1+i\frac{f}{f_0+i\text{FSR}}\right)\left(1+i\frac{f}{f_0-i\text{FSR}}\right)} \tag{B.3}$$

Appendix C

Formulae for radiometer and isotropic search

C.1 Definition of basic quantities

For a stochastic, stationary background of gravitational waves the expectation value of the fields is:

$$\langle h_A^*(f, \Omega), h_{A'}(f', \Omega') \rangle = H_A^{2-\text{sided}}(f) P(\Omega) \delta^2(\Omega, \Omega') \delta_{A,A'} \delta(f - f') \qquad \text{(C.1)}$$

where $P(\Omega)$ is the power distribution across the sky and $H_A^{2-\text{sided}}(f)$ is the 2-sided strain power spectral in polarization A. The goal of the radiometer is to estimate the signal strength from one direction Ω, *assuming* an unpolarized source, i.e.

$$H^{1-\text{sided}}(f) = 4H_+^{2-\text{sided}}(f) = 4H_\times^{2-\text{sided}}(f) \qquad \text{(C.2)}$$

One factor of 2 comes from going from 2-sided to 1-sided, the other is due to the interpretation of $H(f)$ as total power in both polarizations. The superscript "$1 - \text{sided}$" is dropped from here on. (This is a different definition than what Allen and Romano [98] used - their H(f) is 2-sided and per polarization.) The strain power spectral

density $H(f)$ is related to the the energy flux by

$$F_{\text{gw,f}}(\Omega)df = \frac{c^3 \pi f^2}{4G} H(f) P(\Omega) df \tag{C.3}$$

and to the energy density in gravitational waves, ρ_{gw}, by

$$\rho_{gw} = \int_{S^2} d\Omega \int_0^\infty df \frac{c^2 \pi f^2}{4G} H(f) P(\Omega) df. \tag{C.4}$$

Using additionally the critical density from the Friedman equation

$$\rho_c = \frac{3c^2 H_0^2}{8\pi G} \tag{C.5}$$

and assuming an isotropic background, $P(\Omega) = 1$, we find for $\Omega_{gw}(f)$ - the energy density ρ_{gw} per logarithmic frequency f, normalized by the energy density required to close the universe, ρ_c:

$$\Omega_{\text{gw}}(f) = \frac{1}{\rho_c} \frac{d\rho_{\text{gw}}}{d\ln f} = \frac{8\pi^3}{3H_0^2} f^3 H(f) \tag{C.6}$$

In the case of an isotropic background, $P(\Omega) = 1$, the quantity $S_{\text{gw}}(f)$ is defined as the (1-sided) strain power spectrum that 2 co-located and aligned detectors would see. It is connected to $H(f)$ through

$$\gamma_{\text{iso}} S_{\text{gw}} = \int d\Omega \gamma_\Omega H \tag{C.7}$$

Due to the definition of γ_{iso} and γ_Ω (eq. 3.26,3.31) we have $S_{\text{gw}} = \frac{4\pi}{5} H$. S_{gw} plays the same technical role in an isotropic search as H does in the directed search, i.e. the same variable is used in the MATLAB code. S_{gw} is related to $\Omega_{\text{gw}}(f)$ by

$$\Omega_{\text{gw}}(f) = \frac{8\pi^3}{3H_0^2} f^3 H(f) = \frac{10\pi^2}{3H_0^2} f^3 S_{\text{gw}}(f) \tag{C.8}$$

C.2 Basic formulae for the isotropic search

Optimal filter Q (i is the segment index):

$$Q_i = \lambda_i \frac{\gamma_{\mathrm{iso}} S_{\mathrm{gw}}}{P_1 P_2} \tag{C.9}$$

Normalization integral:

$$I_{\mathrm{iso}i} = \lambda_i^{-1} = \int df \frac{|\gamma_{\mathrm{iso}}|^2 S_{\mathrm{gw}}^2}{P_1 P_2} \tag{C.10}$$

Cross-correlation integral:

$$Y_{\mathrm{iso}i} = T(Q_i, \frac{S_1^* S_2}{P_1 P_2}) = T\lambda_i \int df \frac{\gamma_{\mathrm{iso}}^* S_{\mathrm{gw}}}{P_1 P_2} S_1^* S_2 \tag{C.11}$$

Theoretical standard deviation for segment i:

$$\sigma_{\mathrm{iso}i}{}^2 = \frac{T}{4}(Q_i, Q_i) = \frac{T}{4}\lambda_i^2 \int df \frac{|\gamma_{\mathrm{iso}}|^2 S_{\mathrm{gw}}^2}{P_1 P_2} = \frac{T}{4} I_{\mathrm{iso}}{}^{-1} \tag{C.12}$$

Whole run standard deviation and Y_{iso}/T:

$$\sigma_{\mathrm{iso}}{}^{-2} = \sum_i \sigma_{\mathrm{iso}i}{}^{-2}$$
$$Y_{\mathrm{iso}} = \frac{\sum_i Y_{\mathrm{iso}i} \sigma_{\mathrm{iso}i}{}^{-2}}{\sum_i \sigma_{\mathrm{iso}i}{}^{-2}} \tag{C.13}$$

C.3 Basic formulae for the radiometer search

There is a different overlap reduction function $\gamma_{\Omega i}$ for each point Ω in the sky and each segment i. The relation to the isotropic γ_{iso} is (note that γ_{iso} is independent of i and that the additional factor of 2 is introduced such that the radiometer result is normalized to total power in both polarizations of an unpolarized source.)

$$\gamma_{\mathrm{iso}} = 2\frac{5}{8\pi} \int d\Omega \gamma_{\Omega i} \tag{C.14}$$

Optimal filter $Q_{\Omega i}$ (i is the segment index):

$$Q_{\Omega i} = \lambda_{\Omega i} \frac{\gamma_{\Omega i} H}{P_1 P_2} \tag{C.15}$$

Normalization integral:

$$I_{\Omega i} = \lambda_{\Omega i}^{-1} = \int df \frac{|\gamma_{\Omega i}|^2 H^2}{P_1 P_2} \tag{C.16}$$

Cross-correlation integral:

$$Y_{\Omega i} = T(Q_{\Omega i}, \frac{S_1^* S_2}{P_1 P_2}) = T\lambda_{\Omega i} \int df \frac{\gamma_{\Omega i}^* H}{P_1 P_2} S_1^* S_2 \tag{C.17}$$

Theoretical standard deviation for segment i:

$$\sigma_{\Omega i}^2 = \frac{T}{4}(Q_{\Omega i}, Q_{\Omega i}) = \frac{T}{4} \lambda_{\Omega i}^2 \int df \frac{|\gamma_{\Omega i}|^2 H^2}{P_1 P_2} = \frac{T}{4} I_{\Omega i}^{-1} \tag{C.18}$$

Whole run standard deviation and point estimate Y_Ω/T:

$$\sigma_\Omega^{-2} = \sum_i \sigma_{\Omega i}^{-2}$$
$$Y_\Omega = \frac{\sum_i Y_{\Omega i} \sigma_{\Omega i}^{-2}}{\sum_i \sigma_{\Omega i}^{-2}} \tag{C.19}$$

C.4   Relation between radiometer and isotropic search

The relations derived in this section can be used to compare results from the radiometer search to the isotropic search. As mentioned above the quantities S_{gw} and H are represented by the same variable in the MATLAB code, so for the purpose of this paragraph I will set them to be equal. As a result factors of $\frac{5}{4\pi}$ will show up in the final relations.

By inspection of equations C.11, C.17 and C.14 we find the relation

$$Y_{\text{iso}i} \; I_{\text{iso}i} = \frac{5}{4\pi} \int d\Omega Y_{\Omega i} I_{\Omega i} \tag{C.20}$$

Since $\sigma_i^{-2} \propto I_i$ for both the radiometer and the isotropic search this implies

$$Y_{\mathrm{iso}i}\sigma_{\mathrm{iso}i}^{-2} = \frac{5}{4\pi}\int d\Omega Y_{\Omega i}\sigma_{\Omega i}^{-2} \tag{C.21}$$

But these are exactly the quantities that get added up in the optimal combination of individual segments (eq. C.13 and C.19). Therefore the following relation holds for the end result:

$$Y_{\mathrm{iso}}\ \sigma_{\mathrm{iso}}^{-2} = \frac{5}{4\pi}\int d\Omega\ Y_{\Omega}\ \sigma_{\Omega}^{-2} \tag{C.22}$$

The relation between the theoretical sigmas is not quite as straight forward. First we define the 2-point correlation integral $I_{\Omega,\Omega' i}$

$$I_{\Omega,\Omega' i} = \int df \frac{\gamma_{\Omega i}^* \gamma_{\Omega' i} H^2}{P_1 P_2} \tag{C.23}$$

and in analogy to eq. C.18

$$\hat{\sigma}_{\Omega,\Omega' i}^{-2} = \frac{4}{T}I_{\Omega,\Omega' i} \tag{C.24}$$

It has the property $\hat{\sigma}_{\Omega,\Omega i} = \sigma_{\Omega i}$. Note though that $\hat{\sigma}_{\Omega,\Omega' i}$ is not the same as $\sigma_{\Omega,\Omega' i}$, defined by

$$\sigma_{\Omega,\Omega' i}^2 = \langle Y_{\Omega i}Y_{\Omega' i}\rangle = \frac{T}{4}\left(Q_{\Omega i}, Q_{\Omega' i}\right) = \frac{T}{4}\frac{I_{\Omega,\Omega' i}}{I_{\Omega i}I_{\Omega' i}} = \frac{\sigma_{\Omega i}^2 \sigma_{\Omega' i}^2}{\hat{\sigma}_{\Omega,\Omega' i}^2} \tag{C.25}$$

Definition C.24, together with eq. C.12 and C.14, imply

$$\sigma_{\mathrm{iso}i}^{-2} = \left(\frac{5}{4\pi}\right)^2 \int d\Omega \int d\Omega' \hat{\sigma}_{\Omega,\Omega' i}^{-2} \tag{C.26}$$

and, after summing over all i

$$\sigma_{\mathrm{iso}}^{-2} = \left(\frac{5}{4\pi}\right)^2 \int d\Omega \int d\Omega' \hat{\sigma}_{\Omega,\Omega'}^{-2} \tag{C.27}$$

where $\hat{\sigma}_{\Omega,\Omega'}^{-2} = \sum_i \hat{\sigma}_{\Omega,\Omega' i}^{-2}$. The quantities $\hat{\sigma}_{\Omega,\Omega' i}$ are not calculated in the radiometer code since they are not required for the radiometer end result. In order to still be able to use relation C.22 the radiometer code instead also directly calculates the isotropic

σ_{iso}. This provides a powerful sanity check.

C.5 Remarks on deconvolving the radiometer

C.5.1 Inverse of 2-point correlation integral

The key for the deconvolution problem is knowledge of the inverse $F_{\tilde{\Omega},\Omega}$ of $I_{\Omega,\Omega'} = \sum_i I_{\Omega,\Omega'i}$, defined by

$$\int d\Omega F_{\tilde{\Omega},\Omega} \int d\Omega' I_{\Omega,\Omega'} P_{\Omega'} = P_{\tilde{\Omega}} \quad \forall\ P_{\Omega'} \tag{C.28}$$

or

$$\int d\Omega F_{\tilde{\Omega},\Omega} I_{\Omega,\Omega'} = \delta^2\left(\tilde{\Omega}, \Omega'\right) \tag{C.29}$$

Discretizing the integral $\int d\Omega = \sum_n w_n$, with w_n the area corresponding to the nth pixel, results in

$$\sum_n F_{kn} w_n \sum_m I_{nm} w_m P_m = P_k \tag{C.30}$$

or

$$\sum_n F_{kn} w_n I_{nm} w_m = \delta_{k,m} \tag{C.31}$$

in other words F_{kn} is given by the matrix inversion

$$F_{kn} = \left[[w_n I_{nm} w_m]^{-1}\right]_{kn} \tag{C.32}$$

This looks easy, but the real problem arises because the matrix $w_n I_{nm} w_m$ will be badly conditioned as soon as the pixel resolution exceeds the intrinsic antenna resolution given by $I_{\Omega,\Omega'}$. Also the dimension of this matrix is N^2 with N the number of pixels per map, i.e. this can be a numerical challenge.

C.5.2   Deconvolved radiometer problem statement

In order to get a map that is not convolved with the antenna pattern we have to redefine what we mean by an optimal filter. To simplify the notation I define an additional scalar product that includes the integration over time (summation over segments i):

$$[A_i(f), B_i(f)] = \sum_i (A_i(f), B_i(f)) = \sum_i \int df\, A_i(f)^* B_i(f) P_1(f) P_2(f) \qquad \text{(C.33)}$$

This allows to state the problem:

The expectation value of the cross-correlation $\langle Y_\Omega \rangle$ has to be equal to the gravitational wave flux $P(\Omega)$ at Ω, for all Ω

$$\langle Y_\Omega \rangle = T[Q_{\Omega i}, \int d\bar{\Omega} \frac{\gamma_{\Omega i} H}{P_1 P_2} P(\bar{\Omega})] \equiv T P(\Omega) \qquad \text{(C.34)}$$

and the variances

$$\sigma^2_{\Omega,\Omega} = \frac{T}{4}[Q_{\Omega i}, Q_{\Omega i}] \qquad \text{(C.35)}$$

have to be minimized. Weighting all sky directions equally suggests minimizing

$$\int d\Omega \sigma^2_{\Omega,\Omega} = min \qquad \text{(C.36)}$$

To make the notation more transparent it is worth translating the problem to matrix notation.
$Q = Q_{\Omega, i}(f)$, $M = M_{\Omega, i}(f) = \frac{\gamma_{\bar{\Omega}, i}}{P_1 P_2}$, I: identity matrix
The 1st index of Q and M is the combined time-frequency summation, the 2nd index is the sky position. With that the problem statement (eq. C.34 to C.36) becomes

$$Q^\dagger M = I$$
$$\qquad \text{(C.37)}$$
$$tr Q^\dagger Q = min$$

C.5.3 Deconvolved radiometer formal solution

Eq. C.37 is a classical under-constrained least-square problem. The formal solution goes as follows: Define $L = (M^\dagger M)^{-1}$. Then any Q of the form $Q = ML^\dagger + K$ with $K^\dagger M = 0$ fulfills equation C.37a, and equation C.37b yields $K = 0$. Thus $Q = ML^\dagger$.

Translating back to the usual notation we find that L is nothing but $F_{\tilde{\Omega},\Omega}$. Thus we find a new optimal filter

$$\tilde{Q}_{\tilde{\Omega}\,i} = \int d\Omega F^*_{\tilde{\Omega},\Omega} \frac{\gamma_{\Omega i} H}{P_1 P_2} \tag{C.38}$$

a new cross-correlation integral

$$\left\langle \tilde{Y}_{\tilde{\Omega}\,i} \right\rangle = T(\tilde{Q}_{\Omega i}, \frac{S_1^* S_2}{P_1 P_2}) = T \int d\Omega F_{\tilde{\Omega},\Omega} \int df \frac{\gamma_{\Omega i}^* H}{P_1 P_2} S_1^* S_2 \tag{C.39}$$

and a new theoretical standard deviation

$$
\begin{aligned}
\tilde{\sigma}_{\tilde{\Omega}}^2 &= \frac{T}{4} \sum_i (\tilde{Q}_{\tilde{\Omega}\,i}, \tilde{Q}_{\tilde{\Omega}\,i}) \\
&= \frac{T}{4} \sum_i \int d\Omega' F^*_{\tilde{\Omega},\Omega'} \int d\Omega F_{\tilde{\Omega},\Omega} \int df \frac{\gamma_{\Omega i}^* \gamma_{\Omega' i} H^2}{P_1 P_2} \\
&= \frac{T}{4} \int d\Omega' F^*_{\tilde{\Omega},\Omega'\,i} \int d\Omega F_{\tilde{\Omega},\Omega\,i} \sum_i I_{\Omega,\Omega'\,i} \\
&= \frac{T}{4} F^*_{\tilde{\Omega},\tilde{\Omega}}
\end{aligned}
\tag{C.40}
$$

C.5.4 Generic problem of the deconvolved radiometer

Obviously the key problem is calculating the inverse $F_{\tilde{\Omega},\Omega}$ of the 2-point correlation integral $I_{\tilde{\Omega},\Omega}$ which describes the antenna lobe of the synthetic aperture. Since $I_{\tilde{\Omega},\Omega}$ smears the signal out on the typical angular scale $\alpha = \frac{c}{fd}$ (d: site separation, f: typical signal frequency, c: light speed) any attempt to achieve a significantly higher resolution than α is necessarily going to run into numerical trouble.

But there is also a more fundamental reason why this deconvolution is not too meaningful. The described deconvolved radiometer search aims at finding the distribution $P(\Omega)$ assuming the signal spectrum H is the same for the whole sky, an

assumption that most likely is wrong. The actual shape of the synthetic aperture antenna lobe, and therefore the deconvolved map, however depends on the signal spectrum H which has to be put in a priori. Thus, even if there were a signal, the resulting sky map would most likely not be accurate. For that reason the deconvolution problem was not pursued in this thesis.

Appendix D

Correction to the TCS noise coupling

D.1   Estimate of bending correction

In section 2.8.5 I used the formula for a bimetallic strip 2.40 to estimate the locally induced curvature of the optic. Here I estimate the effect of the geometric constraint of a large optic if the optic is only heated at the center.

I do this by dividing the optic into a near zone $r < r_1$ and a far zone $r_1 < r < r_2 = R_{\text{optic}}$ and estimate the energy required to bend the optic.
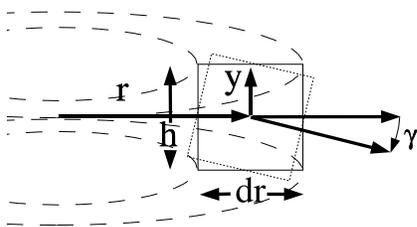

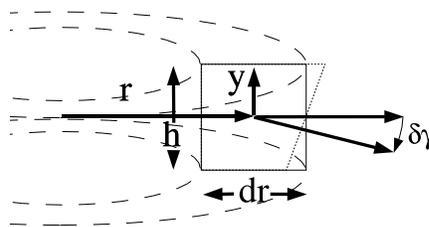Figure D-1:   **Schematic of ring element in far zone**

Figure D-2:   **Schematic of ring element in near zone**

D.1.1 Far zone

I focus on a ring element at radius r with radial size dr and thickness h. When the near zone is bent by an angle $\gamma = \int_0^{r_1} dr \, 1/R(r)$ this ring element gets both translated along the optical axis and rotated by the angle γ. No energy is required for the translation. But a rotation stretches the circumference by $\Delta l/l = y \, \gamma/r$. Thus the energy required to do this is

$$
\begin{aligned}
\text{Energy} &= \int_{r_1}^{r_2} \int_{-h/2}^{h/2} \frac{1}{2} E_S \left(\frac{y\gamma}{r}\right)^2 dy \ 2\pi r dr \\
&= \frac{\pi E_S h^3}{12} \gamma^2 \ln \frac{r_2}{r_1}
\end{aligned}
\tag{D.1}
$$

where E_S is the Young's Modulus.

D.1.2 Near zone

Here the bending angle changes as $\delta\gamma = dr/R(r)$. Again I focus on a ring element at radius r with radial size dr and thickness h, but now the dominant term comes from bending the element like a rod, i.e. $\Delta l/l = y \, d\gamma/dr$. Thus the energy required to do this is

$$
\begin{aligned}
\text{Energy} &= \int_0^{r_1} \int_{-h/2}^{h/2} \frac{1}{2} E_S \left(\frac{y d\gamma}{dr}\right)^2 dy \ 2\pi r dr \\
&= \frac{\pi E_S h^3}{12} \gamma^2 \left(\frac{1}{\gamma^2(r_1)} \int_0^{r_1} dr \ r \left(\frac{d\gamma(r)}{dr}\right)^2\right) \\
&= \frac{\pi E_S h^3}{12} \gamma^2 K(\text{shape})
\end{aligned}
\tag{D.2}
$$

K is a numerical constant that only depends on the shape of $d\gamma(r)/dr$. For a Gaussian profile with radius $w \ll r_1$ we have $K = 1/\pi$.

D.1.3 Energy balance

Based on the bimetallic strip formula 2.40 we estimate a total bending angle $\gamma_0 = \frac{6\alpha}{h^2} \int_0^{r_1} dr \int dz T(z, r)$. But this does not include the energy required to bend the

optic in the far zone. The actual total bending angle γ can thus be estimated by minimizing

$$\text{Energy} = \frac{\pi E_S h^3}{12} \left(K(\gamma - \gamma_0)^2 + \gamma^2 \ln \frac{r_2}{r_1} \right) \tag{D.3}$$

which gives

$$\frac{\gamma}{\gamma_0} = \frac{1}{1 + K^{-1} \ln \frac{r_2}{r_1}} \tag{D.4}$$

Since the induced displacement $\langle \triangle z_3 \rangle$ is linear in γ the same correction factor applies to it.

D.2   Next order correction to the local coupling

Here I show that for an infinitely large optic with a *not* infinitesimally thin heated surface layer the next order correction for the TCS transfer function (Equation 2.38, derived in section 2.8.5) is

$$\begin{aligned}
\triangle z(x, y) = & \left[(1 + \eta)\alpha \left(1 - \frac{\pi}{2\mathcal{F}}(n - 1) \right) - \frac{\pi}{2\mathcal{F}} \frac{dn}{dT} \right] \frac{d^2}{i\kappa} p(x, y) \\
& - \frac{\pi}{2\mathcal{F}} \frac{dn}{dT} \frac{d^2}{i\kappa} \left(-id^2 \triangle_2 \right) p(x, y) \\
& + \text{Terms of order} \left(d^4 \triangle_2^2 \right) p(x, y)
\end{aligned} \tag{D.5}$$

where the surface layer thickness parameter is $d = \sqrt{\kappa/(2\pi f C \rho)}$ (Equation 2.34). The small parameter used for the expansion is $d^2 \triangle_2$ ($\triangle_2$ is the 2-dim Laplace operator on the surface $z = 0$.)

Derivation: Heat diffusion: First we need to solve $C\rho\partial_t T = \kappa \triangle T + 2p(x, y)\delta(z)$ (the heat diffusion equation) up to first order in $d^2 \triangle_2$. Note that there is an additional factor of 2 in the source term because the heat is only conducted away on one side. In Fourier space this equation is

$$\left(k_z^2 + id^{-2} \right) \tilde{T} = -k_T^2 \tilde{T} + \frac{2\tilde{p}}{\kappa} \tag{D.6}$$

Which can iteratively be solved up to first order:

$$\tilde{T}^{(0+1)} = \frac{2\tilde{p}/\kappa}{k_z^2 + id^{-2}} - \frac{k_T^2 2\tilde{p}/\kappa}{\left(k_z^2 + id^{-2}\right)^2} \tag{D.7}$$

The integral $\int_0^\infty dz T^{0+1}(z)$ is then equal to $\tilde{T}^{(0+1)}(k_z = 0)/2$, i.e.

$$\int_0^\infty dz T^{(0+1)} = \frac{-id^2}{\kappa} \left[1 - id^2 \triangle_2\right] p(x,y) \tag{D.8}$$

We will need the Fourier transform "$k_z \to z$" only for the 0th order, which can be calculated using the Cauchy Integral Theorem ($z > 0$):

$$T^{(0)} = \frac{2p}{\kappa} \frac{1}{2\pi} \int_{-\infty}^\infty dk_z \frac{e^{-ik_z z}}{k_z^2 + id^{-2}} = \frac{p}{\kappa} d \frac{(1-i)}{\sqrt{2}} \exp\left(-\frac{(1+i)}{\sqrt{2}} \frac{z}{d}\right) \tag{D.9}$$

Elastic problem: We now need to solve the elastic equilibrium equation with boundary condition on $z = 0$ in the half plane $z > 0$:

$$\frac{1-\eta}{1+\eta} \nabla \left(\nabla \cdot \vec{v}\right) - \frac{1-2\eta}{2(1+\eta)} \nabla \wedge \nabla \wedge \vec{v} = \alpha \nabla T \tag{D.10}$$

$$\begin{aligned}
\sigma_{zz} &= \frac{E}{1-2\eta} \left[\frac{\eta}{1+\eta}\left(\nabla \cdot \vec{v}\right) - \alpha T + \frac{1-2\eta}{1+\eta} \frac{\partial v_z}{\partial z}\right]\Big|_{z=0} = 0 \\
\sigma_{xz} &= \frac{E}{2(1+\eta)} \left[\frac{\partial v_z}{\partial x} + \frac{\partial v_x}{\partial z}\right]\Big|_{z=0} = 0 \\
\sigma_{yz} &= \frac{E}{2(1+\eta)} \left[\frac{\partial v_z}{\partial y} + \frac{\partial v_y}{\partial z}\right]\Big|_{z=0} = 0
\end{aligned} \tag{D.11}$$

$\vec{v}$ is the displacement field, E is the Young's modulus and η is the Poisson ratio. Here I am following more or less [72] and [73], section 8. This problem can be reduced with the Ansatz $\vec{v} = \vec{v}_0 + \nabla\phi$, where ϕ fulfills the Poisson equation

$$\triangle\phi = \frac{1+\eta}{1-\eta} \alpha T \tag{D.12}$$

without boundary condition and $\vec{v}_0$ fulfills equation D.10 with zero source term and

new boundary conditions

$$\sigma_{zz} = \frac{E}{1+\eta} [\triangle_2 \phi] \Big|_{z=0}$$

$$\sigma_{xz} = -\frac{E}{(1+\eta)} \left[\frac{\partial^2 \phi}{\partial x \partial z} \right] \Big|_{z=0} = 0 \qquad \text{(D.13)}$$

$$\sigma_{yz} = -\frac{E}{(1+\eta)} \left[\frac{\partial^2 \phi}{\partial y \partial z} \right] \Big|_{z=0} = 0$$

Here $\triangle_2 = \partial_x^2 + \partial_y^2$. This second step ("$\phi \to \vec{v}$") is solved in [73], section 8. Equation D.12 can be integrated:

$$\phi(x, y, z = 0) = -\frac{1+\eta}{1-\eta} \frac{\alpha}{4\pi} \int dx' dy' \int dz' \frac{T(x', y', z')}{\sqrt{(x-x')^2 + (y-y')^2 + (z')^2}} \qquad \text{(D.14)}$$

We can now use equation D.9 and the abbreviation $a := \sqrt{(x-x')^2 + (y-y')^2}$ to evaluate the integration over z'.

$$\begin{aligned}
\int_0^\infty dz' \frac{T^{(0)}}{\sqrt{a^2 + (z')^2}} &= \frac{-id^2}{a} \frac{p}{\kappa} \int_0^\infty dX \frac{e^{-X}}{\sqrt{1 - id^2 a^{-2} X^2}} \\
&= \frac{-id^2}{a} \frac{p}{\kappa} \int_0^\infty dX e^{-X} \left[1 + id^2 a^{-2} \frac{X^2}{2} + O\left(d^4 a^{-4} X^4\right) \right] \\
&= \frac{-id^2}{a} \frac{p}{\kappa} \left[1 + id^2 a^{-2} + O\left(d^4 a^{-4}\right) \right] \\
&= -id^2 \frac{p}{\kappa} \left[1 + id^2 \triangle_2' + O\left(d^4 \triangle_2'^2\right) \right] \frac{1}{a}
\end{aligned} \qquad \text{(D.15)}$$

The last step is true because $\triangle_2' a^{-1} = a^{-3}$. Inserting this result into equation D.14 and using integration by parts twice to move the Laplace operator over to $p(x', y')$ gives

$$\phi^{(0)}(x, y) = -\frac{1+\eta}{1-\eta} \frac{\alpha}{4\pi} \int dx' dy' \frac{1}{a} \frac{-id^2}{\kappa} \left[1 + id^2 \triangle_2' + O\left(d^4 \triangle_2'^2\right) \right] p(x', y'). \qquad \text{(D.16)}$$

At the same time we also have a contribution of $T^{(1)}$.

$$\phi^{(1)}(x, y) = -\frac{1+\eta}{1-\eta} \frac{\alpha}{4\pi} \int dx' dy' \frac{1}{a} \frac{-id^2}{\kappa} \left[-id^2 \triangle_2' + O\left(d^4 \triangle_2'^2\right) \right] p(x', y'). \qquad \text{(D.17)}$$

The 2 terms of order $d^2 \triangle_2'$ cancel each other exactly.

Now we can solve for v_z. According to [73], section 8 v_z is given by

$$v_z = \frac{1-\eta^2}{\pi E} \int dx' dy' \frac{\sigma_{zz}^{z'=0}}{\sqrt{(x-x')^2 + (y-y')^2}} \tag{D.18}$$

and $\sigma_{zz}^{z'=0}$ is given by equation D.13. Putting everything together and neglecting terms of order $(d^4 \triangle_2''^2)$ we get

$$\begin{aligned} v_z(x,y) &= -\frac{(1+\eta)\alpha}{4\pi^2} \frac{d^2}{i\kappa} \int d^2 x' \frac{1}{|\vec{x} - \vec{x}'|} \triangle_2' \int d^2 x'' \frac{1}{|\vec{x'} - \vec{x''}|} p(x'', y'') \\ &= (1+\eta)\alpha \frac{d^2}{i\kappa} p(x,y) \end{aligned} \tag{D.19}$$

Conversion to displacement noise: So after all that work the surface displacement $\triangle z_1 = v_z$ remains unchanged up to order $(d^4 \triangle_2^2)$! The term proportional to $\frac{dn}{dT}$ however is scaled by $[1 - id^2 \triangle_2]$, resulting in equation D.5. This correction is only in phase though - the *magnitude* of the transfer function remains totally unchanged up to order $(d^4 \triangle_2^2)$ terms.

Bibliography

[1] Albert Einstein Über Gravitationswellen. *Sitzungsberichte der Königlich Preussischen Akademie der Wissenschaften Berlin* (1918), 154-167

[2] R. A. Hulse and J. H. Taylor. Discovery of a pulsar in a binary system. *Astrophys. Journ.*, 195:L51–L53, 1975.

[3] J. M. Weisberg and J. H. Taylor. General relativistic geodetic spin precession in binary pulsar B1913+16: mapping the emission beam in two dimensions. *Astrophys. Journ.*, 576(2):942–949, 2002.

[4] D. J. Champion, D. R. Lorimer, M. A. McLaughlin, J. M. Cordes, Z. Arzoumanian, J. M. Weisberg, and J. H. Taylor. PSR J1829+2456: a relativistic binary pulsar. *Mon. Not. R. Astron. Soc.*, 000:1–5, March 2004.

[5] G. F. Smoot *et al.*, "Structure in the COBE DMR first year maps," Astrophys. J. **396**, L1 (1992).

[6] C.L. Bennett *et al.*, "First Year Wilkinson Microwave Anisotropy Probe (WMAP) Observations: Preliminary Maps and Basic Results", Astrophys. J. S. **148**, 1 (2003).

[7] C. W. Misner, K. S. Thorne, and J. A. Wheeler. *Gravitation*. W. H. Freeman and Co., 1970.

[8] Peter R. Saulson. *Fundamentals of Interferometric Gravitational Wave Detectors*. World Scientific, 1994.

[9] L. Bildsten. Gravitational radiation and rotation of accreting neutron stars. *Astro. Journal*, 501:L89–L93, 1998.

[10] D. Chakrabarty, E. H. Morgan, M. P. Muno, D. K. Galloway, R. Wijnands, M. van der Klis, and C. B. Markward. Nuclear-powered millisecond pulsars and the maximum spin frequency of neutron stars. *Nature*, 424:42–44, July 2003.

[11] D. Chakrabarty. Millisecond Pulsars in X-Ray binaries. *astro-ph*/0408004 July 2004.

[12] Yu. N. Gnedin; N. A. Silant'ev; L. G. Titarchuk. Sco X-1 and Cyg X-1: Determination of Strength and Structure of Magnetic Field in the Nearest Environment of Accreting Compact Stars. *astro-ph*/0207640, 2002.

[13] C. F. Bradshaw, E. B. Fomalont, B. J. Geldzahler. High-Resolution Parallax Measurements of Scorpius X-1. *ApJ*, 512L121 (1999).

[14] E. W. Gottlieb,E. L. Wright, W. Liller. Optical studies of UHURU sources. XI. A probable period for Scorpius X-1 = V818 Sco. *ApJ*, 195L33 (1975).

[15] van der Klis et al., Discovery of Submillisecond Quasi-periodic Oscillations in the X-Ray Flux of Scorpius X-1. *ApJL*, 496, L1 (1996).

[16] C. M. Zhang, H. X. Yin, Y. H. Zhao, F. Zhang, L. M. Song, The correlations between the twin kHz QPO frequencies of LMXBs. gr-qc/0601318.

[17] L. Bildsten, V. Mandic. Personal communication 2005.

[18] E. E. Flanagan and S. A. Hughes. Measuring gravitational waves from binary black hole coalescences. i. signal to noise for inspiral, merger, and ringdown. *Phys. Rev. D*, 57(8):4535–4565, 1998.

[19] C. W. Misner, R. A. Breuer, D. R. Brill, P. L. Chrzanowski, H. G. Hughes, and C. M. Pereira. Gravitational synchrotron radiation in the Schwarzschild geometry. *Phys. Rev. Lett.*, 28:998–1001, 1972.

[20] S.W. Hawking. Theory of the detection of short bursts of gravitational radiation. *Phys. Rev. D*, 4:2191–2197, 1971.

[21] B. Allen. A χ^2 time-frequency discriminator for gravitational wave detection. *arXiv*, pages gr–qc/0405045, 2004. http://xxx.lanl.gov/abs/gr-qc/0405045.

[22] A. Buonanno, Y. Chen, and M. Vallisneri. Detection template families for gravitational waves from the final stages of binary black-hole inspirals: Nonspinning case. *Phys. Rev. D*, 67:024016, 2003.

[23] C. Kim, V. Kalogera, D. R. Lorimer, M. Ihm, and K. Belczynski. The galactic double-neutron-star merger rate: Most current estimates. In F. Rasio, editor, *Binary Radio Pulsars*, 2004. http://xxx.lanl.gov/abs/astro-ph/0405564.

[24] C. Kim, V. Kalogera, D. R. Lorimer, M. Ihm, and K. Belczynski. The double-neutron star inspiral rate snd expectations for gravitational-wave detection. http://www.astro.northwestern.edu/Vicky/Papers/69.pdf.

[25] J. Weber. Detection and generation of gravitational waves. *Phys. Rev.*, 117:306–313, 1960.

[26] J. L. Levine and R. L. Garwin. New negative result for gravitational wave detection and comparison with reported detection. *Phys. Rev. Lett.*, 33(13):794–797, September 1974.

[27] J. A. Tyson. Null search for bursts of gravitational radiation. *Phys. Rev. Lett.*, 31(5):326–329, July 1973.

[28] J. Weber. Evidence for discovery of gravitational radiation. *Phys. Rev. Lett.*, 22:1320–1324, 1969.

[29] A. Morse, W. O. Hamilton, W. W. Johnson, E. Mauceli, and M. P. McHugh. Calibration and sensitivity of resonant-mass gravitational wave detectors. *Phys. Rev. D*, 59, 1999.

[30] M. Cerdonio, L. Conti, J. A. Lobo, A. Ortolan, L. Taffarello, and J. P. Zendri. Wideband dual sphere detector of gravitational waves. *Phys. Rev. Lett.*, 87, 2001.

[31] Viviana Fafone. Resonant-mass detectors: status and perspectives. *Class. Quantum Grav.*, 21:S377–S383, 2004.

[32] Ch. Fabry and A. Perot. On a new form of interferometer. *Astrophys. J.*, 13:265–272, 1901.

[33] F. A. E. Pirani. *Acta. Phys. Polon.*, 15:389, 1956.

[34] G.F. Moss, L.R. Miller, and R.L. Forward. Photon-noise-limited laser transducer for gravitational antenna. *Applied Optics*, 10:2495–2498, 1971.

[35] R. W. P. Drever, J. L. Hall, F. V. Kowalski, J. Hough, G. M. Ford, A. J. Munley, and H. Ward. Laser phase and frequency stabilization using an optical resonator. *Appl. Phys. B*, 31:97–105, June 1983.

[36] D. Schnier, J. Mizuno, G. Heinzel, H. Lück, A. Rüdiger, R. Schilling, M. Schrempel, W. Winkler, and K. Danzmann. Power recyling in the garching 30 m prototype interferometer for gravitational-wave detection. *Phys. Lett. A*, 225:210–216, 1997.

[37] Rainer Weiss. Electromagnetically coupled broadband gravitational antenna. Quarterly Progress Report 105, Research Laboratory of Electronics, MIT, April 1972.

[38] Rai Weiss. Caltech/MIT project for a laser interferometer gravitational wave observatory. Proposal to the National Science Foundation, 1987.

[39] A. Lazzarini, R. Weiss, LIGO Science Requirement Document. LIGO-E950018-02 (1995).

[40] B. Willke and the GEO 600 Collaboration. Status of GEO 600. *Class. Quant. Grav.*, 21:S417–S423, 2004.

[41] R. Takahashi and the TAMA Collaboration. Status of TAMA 300. *Class. Quant. Grav.*, 21:S403–S408, 2004.

[42] Daniel Sigg. Commissioning of LIGO detectors. *Class. Quant. Grav.*, 21:S409–S415, 2004.

[43] A. Abramovici *et al.*, "LIGO: The Laser interferometer gravitational wave observatory," Science **256**, 325 (1992).

[44] B. Barish and R. Weiss, Phys. Today **52**, 44 (1999).

[45] R. Weiss and B. Barish. LIGO and the detection of gravitational waves. *Physics Today*, 52:44–50, 1999. LIGO-P990039-00-R.

[46] F. Frasconi for the VIRGO Collaboration. Status of VIRGO. *Class. Quant. Grav.*, 21:S385–S394, 2004.

[47] Daniel Sigg. Frequency response of the LIGO interferometer. Technical report, MIT, 1997. LIGO-T970084-00-D.

[48] P. Fritschel, R. Bork, G. González, N. Mavalvala, D. Ouimette, H. Rong, D. Sigg, and M. Zucker. Readout and control of a power-recycled interferometric gravitational-wave antenna. *Applied Optics*, 40(28):4988–4998, October 2001.

[49] The LIGO Scientific Collaboration. Detector description and performance for the first coincidence observations between LIGO and GEO. *Nucl.Instrum.Meth.*, 517:154–179, 2004.

[50] P. Fritschel, R. Adhikari, R. Weiss. Enhancements to the LIGO S5 Detectors. Technical report, 2005. LIGO-T050252-00-I.

[51] Rana Adhikari. *Sensitivity and Noise Analysis of 4 km Laser Interferometric Gravitational Wave Antennae*. PhD thesis, Massachusetts Institute of Technology, 2004. July.

[52] Peter K. Fritschel. *Techniques for Laser Interferometer Gravitational Wave Detectors*. PhD thesis, Massachusetts Institute of Technology, February 1992.

[53] Matt Evans. *Lock Acquisition in Resonant Optical Interferometers*. PhD thesis, Caltech, 2002.

[54] M. Evans, N. Mavalvala, P. Fritschel, R. Bork, B. Bhawal, H. Yamamoto, and S. Whitcomb. Lock acquisition of a gravitational wave interferometer. *Optics Lett.*, 27(8):598–600, 2002. LIGO-P010015-A-D.

[55] Jun Mizuno. *Comparison of optical configurations for laser-interferometric gravitational-wave detectors*. PhD thesis, Max-Planck-Institut Fur Quantenoptik, July 1995.

[56] Rana Adhikari, Peter Fritschel. LOS Output Electronics Modifications. Technical report, 2004. LIGO-T040172-00-D.

[57] Phil Willems. Comments on TCS Injected Noise. Personal communication (2006).

[58] J. Giaime, P. Saha, D. Shoemaker, and L. Sievers. A passive vibration isolation stack for LIGO: Design, modeling, and testing. *Rev. Sci. Inst.*, 67:208–214, 1996.

[59] A. Gillespie and F. Raab. Thermally excited vibrations of the mirrors of laser interferometer gravitational-wave detectors. *Phys. Rev. D*, 52:577–585, 1995.

[60] G. I. González and P. R. Saulson. Brownian motion of a mass suspended by an anelastic wire. *Journal of the Acoustical Society of America*, 96:207–212, 1994.

[61] Yu. Levin. Internal thermal noise in the LIGO test masses: a direct approach. *Physical Review D*, 57:659–663, 1998.

[62] G. M. Harry, A. M. Gretarsson, P.R. Saulson, S. E. Kittelberger, S.D. Penn, W.J.Startin, S. Rowan, M.M. Fejer, D.R.M. Crooks, G. Cagnoli, J. Hough, and

N. Nakagawa. Thermal noise in interferometric gravitational wave detectors due to dielectric optical coatings. *Class. Quantum Grav.*, 19:897–917, 2002.

[63] Gabriela González. Suspension thermal noise in the LIGO gravitational wave detector. *Class. Quantum Grav.*, 17:4409–4435, 2000. http://arxiv.org/abs/gr-qc/0006053.

[64] T. M. Niebauer, R. Schilling, K. Danzmann, A. Rüdiger, and W. Winkler. Nonstationary shot noise and its effect on the sensitivity of interferometers. *Phys. Rev. A*, 43(9):5022–5029, 1991.

[65] M. Rakhmanov, F. Bondu, O. Debieu, and R. L. Savage Jr. Characterization of the LIGO 4 km fabry-perot cavities via their high-frequency dynamic responses to length and laser frequency variations. *Class. Quantum Grav.*, 21:S487–S492, 2004.

[66] Rai Weiss. Compilation of metrology data for the LIGO large optics. Technical report, MIT, 1998. http://www.ligo.caltech.edu/docs/T/T980065-00.pdf.

[67] Ryan Lawrence. *Active wavefront Correction in Laser Interferometric Gravitational Wave Detectors.* PhD thesis, Massachusetts Institute of Technology, February 2003.

[68] M. Smith, D. Ottaway, P. Willems, C. Vorvick, G. Moreno. Heating Beam Pattern Optical Design. CO2 Laser Thermal Compensation Bench LIGO-T040057-01-D.

[69] S. Ballmer, V. Frolov, R. Lawrence, W. Kells, G. Moreno, K. Mason, D. Ottaway, M. Smith, C. Vorvick, P. Willems, M. Zucker. Thermal Compensation System Description. LIGO-T050064-00-R.

[70] D. Ottaway, J. Betzwieser, S. Ballmer, S. Waldman, W. Kells. In-situ measurement of absorption in high power interferometers using beam diameter measurements *Optics Lett.*, Vol 31(4) 2006.

[71] H. Armandula. Component specification, Input Test Mass, 4k, substrate, coated. *LIGO internal document*, E980067-00-D, 1998.

[72] V.B. Braginsky, S.P. Vyatchanin. Thermodynamical fluctuations in optical mirror coatings. *Phys. Lett. A*, 312:244-255, 2003.

[73] L.D. Landau, E.M. Lifshitz. Theory of Elasticity. *Nauka Moscow*, 1980 translation Pergamon Oxford, 1986.

[74] G. Mueller and Q. Shu, R. Adhikari, D. B. Tanner, D. Reitze, D. Sigg, N. Mavalvala, J. Camp. Determination and optimization of mode matching into optical cavities by heterodyne detection. *Optics Lett.*, 25(4):266–268, 2000. *LIGO* , P000001-00-R.

[75] GariLynn Billingsley. LIGO core optics components website. http://www.ligo.caltech.edu/∼gari/index.htm, 2002. A compilation of specifications and metrology data for the LIGO core optics.

[76] T. W. Clyne. Key Engineering Materials 116-117 (1996), p. 307.

[77] David R. Lide, editor. *CRC Handbook of Chemistry and Physics*. CRC Press, Boca Raton, FL, 3rd electronic edition, 2000. Available online at http://www.knovel.com

[78] NIST. 2002 codata values. http://physics.nist.gov/constants/, 2003. Latest constants as of December 2002.

[79] J. Hough, J. R. Pugh, R. Bland, R. W. Drever, "Search for continuous gravitational radiation" Nature **254**, 498 (1975)

[80] P. Astone et al., "Upper limit for a gravitational-wave stochastic background with the Explorer and Nautilus resonant detectors" Phys. Lett. B **385**, 421 (1996)

[81] P. Astone et al., "Upper limit at 1.8 kHz for a gravitational-wave stochastic background with the ALTAIR resonant-mass detector" Astronomy and Astrophysics **343**, 19 (1999)

[82] P. Astone et al., "Cross-correlation measurement of stochastic gravitational waves with two resonant gravitational wave detectors" Astronomy and Astrophysics **351**, 811 (1999)

[83] P. Astone, V. Ferrari, M. Maggiore, J. D. Romano, "Stochastic background of gravitational waves" Int. J. Mod. Phys. D **9**, 361 (2000)

[84] K. Compton, D. Nicholson, B. F. Schutz, *Proceedings of the Seventh Marcel Grossman Meeting on General Relativity* World Scientific, p. 1078 (1994)

[85] J.W. Armstrong, "Stochastic Gravitational Wave Background: Upper Limits in the 10^{-6} to 10^{-3} Hz Band" *et al.*, Astrophys. J. **599**, 806 (2003).

[86] M.P. McHugh *et al.*, "Pulsar timing and the upper limits on a gravitational wave background: A Bayesian approach" Phys. Rev. D **54**, 5993 (1996).

[87] LIGO Scientific Collaboration. Setting upper limits on the strength of periodic gravitational waves from PSR j1939 + 2134 using the first science data from the GEO600 and LIGO detectors. *Phys. Rev. D* **69**, 082004 (2004).

[88] LIGO Scientific Collaboration. Limits on Gravitational-Wave Emission from Selected Pulsars Using LIGO Data. *Phys. Rev. Lett.* **94**, 181103 (2005).

[89] LIGO Scientific Collaboration. Analysis of LIGO data for gravitational waves from binary neutron stars. *Phys. Rev. D*, 69:122001, 2004.

[90] B. Abbott *et al.*, "Analysis of first LIGO science data for stochastic gravitational waves" Phys. Rev. D **69**, 122004 (2004).

[91] B. Abbott *et al.*, "Upper Limits on a Stochastic Background of Gravitational Waves," Phys. Rev. Lett. **95**, 221101 (2005).

[92] Stochastic Analysis Group, LIGO Report, "Companion Technical Note to the S3 Stochastic IFO-IFO Analysis Paper" LIGO Report, LIGO-T050012-01-Z

[93] S. Ballmer, "A radiometer for stochastic gravitational waves," *Classical and Quantum Gravity* accepted for publication (gr-qc/0510096)

[94] M. Maggiore, "Gravitational Wave Experimants and Early Universe Cosmology" Phys. Rep. **331**, 283 (2000) (gr-qc/9909001).

[95] T. Regimbau, J. A. de Freitas Pacheco "Cosmic background of gravitational waves from rotating neutron stars," Astron. Astrophys. **376**, 381 (2001)

[96] B. Allen and A.C. Ottewill, "Detection of Anisotropies in the Gravitational-Wave Stochastic Background," Phys. Rev. D **56**, 545 (1997)

[97] N. J. Cornish, "Mapping the gravitational-wave background," Class. Quantum Grav. **18**, 4277 (2001)

[98] B. Allen and J.D. Romano, "Detecting a stochastic background of gravitational radiation: Signal processing strategies and sensitivities," Phys. Rev. D **59**, 102001 (1999).

[99] N. Christensen, Phys. Rev. D **46**, 5250 (1992); É.É. Flanagan, Phys. Rev. D **48**, 389 (1993).

[100] LIGO Data and Computing Group. Bias from power spectrum measurement in parameter estimation for the stochastic gravitational wave background. Technical report, MIT, 2004. LIGO-T040128-00-E.

[101] A. Lazzarini and J. Romano (2004), "Use of overlapping windows in the stochastic background search" LIGO Report, http://www.ligo.caltech.edu/docs/T/T040089-00.pdf

[102] John Zweizig S4 Data Quality. Technical report, MIT, 2005. LIGO-G050197-00-E.